Cirrus in the Tropical Tropopause Transition Layer: Formation Mechanisms and Influence of the Local and Planetary-Scale Environment

Katrina S. Virts

A thesis submitted in partial fulfillment of the
requirements for the degree of

Master of Science

University of Washington

2009

Program Authorized to Offer Degree: Atmospheric Sciences

University of Washington
Graduate School

This is to certify that I have examined this copy of a master's thesis by

Katrina S. Virts

and have found that it is complete and satisfactory in all respects,
and that any and all revisions required by the final
examining committee have been made.

Committee Members:

_____
John M. Wallace

_____
Qiang Fu

_____
Thomas P. Ackerman

Date: _____

Signature _____

Date _____

University of Washington

Abstract

Cirrus in the Tropical Tropopause Transition Layer:
Formation Mechanisms and Influence of the
Local and Planetary-Scale Environment

Katrina S. Virts

Chair of the Supervisory Committee:
Professor John M. Wallace
Atmospheric Sciences

Cloud boundaries identified during the first two years of data from the CALIPSO satellite-based lidar are used to investigate the formation mechanisms and characteristic environments of cirrus within the tropical tropopause transition layer (TTL). The two primary formation mechanisms for TTL cirrus, as presented in Jensen et al. (1996), are investigated, and TTL cirrus clouds are found to be strongly modulated by large-scale ascent associated with planetary wave activity within the TTL but by nearby convective activity.

CALIPSO data are analyzed in conjunction with temperature profiles from two radiosonde observation sites in the tropical western Pacific as well as Global Forecast System (GFS) 100 hPa temperatures in order to determine the temperature anomalies associated with TTL cirrus. Negative anomalies in the range of 4–6 K are observed within the TTL over the tropical western Pacific when clouds are present.

TTL cirrus clouds are associated with temperature, geopotential height, and wind perturbations within the TTL that resemble the convectively-induced, mixed Kelvin-Rossby wave solutions modeled in Gill (1980). The TTL cirrus signature is centered approximately

30° of longitude to the east of the associated convection center and takes on a shape similar to that of the temperature perturbations. A similar planetary wave signature appears in the TTL cirrus field above the Pacific warm pool region during the evolution of the Madden-Julian Oscillation (MJO). A cirrus maximum is also observed over equatorial Africa and South America during the latter stages of a normal MJO cycle.

Tropical mean TTL cirrus fraction is modulated by the MJO, with ~92% more TTL cirrus equatorward of 10° latitude when the convective maximum enters the Pacific than when the MJO is in its beginning stages. TTL cirrus also varies on annual and, to a lesser degree, interannual time scales, with the boreal winter months and La Niña periods experiencing greater cloudiness.

TABLE OF CONTENTS

LIST OF FIGURES

SECTION 1: INTRODUCTION

Optically thin, often subvisible cirrus clouds are frequently observed in the tropical upper troposphere, most commonly above the western Pacific warm pool. Fractional cloud occurrence decreases rapidly above the 15–16 km level, though some clouds have been observed above 18 km (Fu et al. 2007). Optically thin cirrus are known to impact tropical (and global) climate by virtue of their role in, among other things, the absorption and emission of radiation and troposphere-stratosphere exchange. Two primary formation mechanisms for these clouds, sheared cumulonimbus anvils and in situ formation, have been documented (Jensen et al. 1996).

In the extratropics, there is a sharp boundary between the generally conditionally unstable troposphere and the stable stratosphere (Birner 2006); this boundary is referred to as the tropopause. In the tropics, however, identifying a single level that represents the "top" of the troposphere in a meteorologically or climatologically meaningful way has proved problematic (Highwood and Hoskins 1998, and references therein). Instead, there is what has come to be recognized as a transition region between the troposphere and stratosphere. This transition region is commonly referred to as the tropical tropopause transition layer (TTL). The TTL has been identified in the literature as the region between the altitude of zero net radiative heating near 14–15 km (Alcala and Dessler 2002) and either the cold point tropopause (near 17 km for the tropics as a whole), the level at which the upward mass flux matches that in the lower stratospheric Brewer-Dobson circulation (~18.7 km according to Fu et al. 2007), or the level of the overshooting tops of convective clouds (near 18 km, Alcala and Dessler 2002).

The notion that extensive cirrus layers should exist within the TTL in regions of large-scale ascent (or that, conversely, the absence of such layers indicated that deep convection must supply air directly to the tropical lower stratosphere) was put forth before the necessary

instrumentation to detect widespread optically thin cirrus was in place (Robinson 1980; Holton et al. 1995). Detection of optically thin cirrus cloud decks began in earnest in the 1990s, as ground-based lidars (Mather et al. 1998), lidars aboard experimental aircraft (McFarquhar et al. 2000) and space shuttles (Winker and Trepte 1998), and satellite radiometers (Wang et al. 1996) were used to detect optically thin cirrus and cloud occurrence within the TTL.

In 2006, the CALIPSO satellite (see Section 2), which carries a two-wavelength polarization lidar, was launched and joined NASA's so-called "A-Train" of atmospheric observation satellites. CALIPSO is the first space-based lidar optimized for cloud and aerosol layer detection and is capable of detecting subvisible cirrus layers with optical depths of 0.01 or less (Winker et al. 2007). Figure 1.1 maps the percentage of the cloud profiles acquired by CALIPSO during the period June 2006–June 2008 in which a cloud with base above 15 km can be identified. The top panel includes all the cloud profiles gathered; the other panels show cloud fraction during the four seasons (months included are indicated in the upper left corner). The maximum cloud fraction in each panel is indicated in the lower right corner. In the annual mean, TTL cirrus are identified most frequently — over 20% of the time — above a large region stretching from Southeast Asia southeastward through the Maritime Continent and into the western Pacific. Secondary maxima are found over equatorial Africa and South America. The Central Equatorial Pacific Experiment (CEPEX), conducted during March 1993, identified cirrus cloud decks with bases above 15 km in 29% of lidar return signals obtained during airborne investigations near the date line (McFarquhar et al. 2000). Other studies of subvisible cirrus, such as Wang et al. (1996), have reported cloud frequencies as high as 70% over the western Pacific. Repeating the analysis of Figure 1.1 with higher horizontal resolution and including some tropical cirrus with lower cloud base yields local values similar to those reported by Wang et al. (not shown).

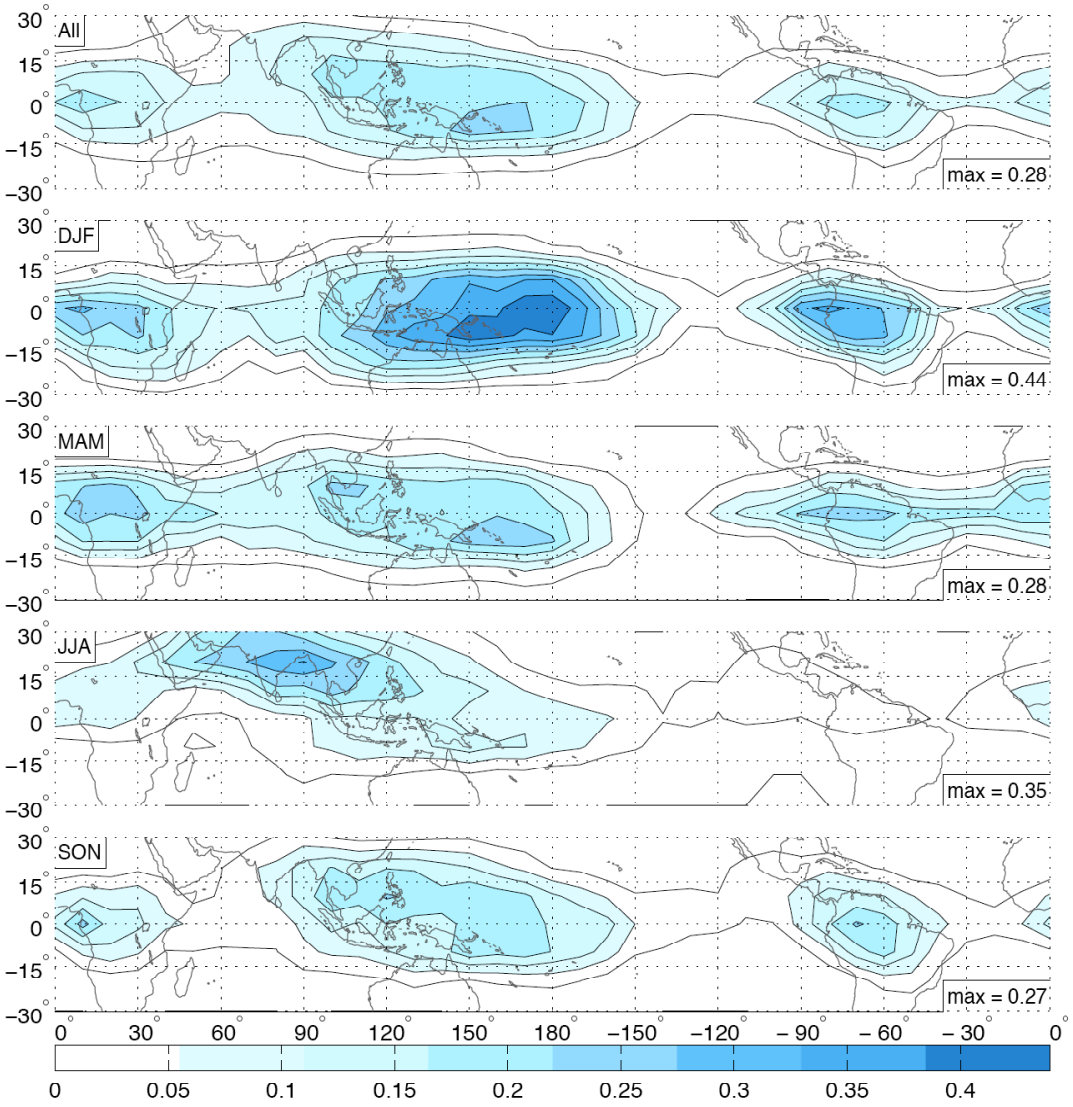

Figure 1.1 Cloud fraction with base above 15 km, calculated from CALIPSO satellite-based lidar profiles. Data are plotted on a 10° latitude × 10° longitude grid for all months ("All"), December–February ("DJF"), March–May ("MAM"), June–August ("JJA"), and September–November ("SON"). Maximum cloud fraction indicated in lower right corner.

Considering the seasonal panels, the highest cloud fractions during the year are observed during the months December–February over the western equatorial Pacific, where an extensive region centered just to the south of the equator has cloud fractions exceeding 0.4. Maximum TTL cloudiness over South America also occurs during the boreal winter months, while equatorial Africa experiences roughly equally TTL cloud fractions during the boreal

winter and spring. During June–August, TTL cirrus occurrence is dominated by the Indian and southeast Asian monsoon, and cloud fractions in excess of 0.25 are observed from the Arabian Sea to the Indochina Peninsula. Spatial correlations between the patterns for individual seasons and the annual mean pattern are 0.89 (December–February), 0.93 (March–May), 0.68 (June–August), and 0.95 (September–November).

The climatological impacts of TTL cirrus have been investigated in a number of previous studies. Radiative cooling (heating) prevails in the tropical troposphere (stratosphere), and the level of zero net radiative heating is within the TTL, near 125 hPa. Radiative properties of TTL cirrus have been deduced in modeling studies. The infrared radiation that they absorb produces heating rates of on average 1.5 K day^{-1} (Corti et al. 2006) and as high as several K day^{-1} (McFarquhar et al. 2000; Jensen et al. 1996). The time mean, tropical mean impact of TTL cirrus is on the order of tenths of a K day^{-1} and is of comparable magnitude to the clear sky heating rates (see Fueglistaler et al. 2009, and references therein).

Climatologically, the tropical troposphere is dominated by the convective overturning which comprises the Hadley circulation, while the tropical stratosphere contains the rising branch of the wave-driven Brewer-Dobson circulation. In order for a sufficient quantity of air to be provided to the Brewer-Dobson circulation, some ascent must also occur in the transition region between the troposphere and stratosphere. Mechanisms such as clear sky upwelling and overshooting convection can contribute to the required upwelling but are insufficient in themselves to explain the magnitude of the observed mass flux (see discussion in Corti et al. 2006). TTL cirrus, as well as occurring as a result of ascent within the TTL, can, once formed, enhance the upwelling. If the radiative heating of the cirrus layer described above is expressed in the form of a diabatic ascent rate, it can be viewed as providing a mechanism for transport across isentropic surfaces. A combination of mass flux due to cirrus cloud lofting and clear

sky upwelling can provide a sufficient supply of air for the Brewer-Dobson circulation (Corti et al. 2006), and trajectory analyses indicate that rapid ascent within convection to the upper troposphere, followed by slower upwelling through the TTL, does in fact occur (Fueglistaler et al. 2004).

TTL cirrus plays a role in the climate not only of the TTL itself, but also by extension the global stratosphere. Stratospheric water vapor mixing ratios are lower than would be expected given the zonal mean cold point temperature in the tropics. Rapid ascent within overshooting convection can introduce dehydrated air into the lower stratosphere (Danielsen 1993); however, it is thought that TTL cirrus plays a more important role in this process. Jensen and Pfister (2004) simulated ice cloud formation and dehydration using a Lagrangian, one-dimensional cloud model with imposed temperature perturbations due to both Rossby and Kelvin waves. They found that air that reached the cold point tropopause after residing in a TTL cirrus layer had been freeze-dried (having water vapor concentrations of approximately 2.5–3.2 ppmv, consistent with observed concentrations within the lower stratosphere). Thus, TTL cirrus plays an important role in regulating stratospheric water vapor, which in turn impacts greenhouse warming and aspects of stratospheric chemistry.

Two contrasting mechanisms for the formation of TTL cirrus have been advanced in the literature. The tropics is a very convectively active region, with deep cumulonimbus clouds frequently reaching the 12–13 km level. The extensive anvils of these clouds are one possible source of tropical cirrus. As a result of the deep convection below, the outflow from the anvil region has high ice water content. The larger ice crystals precipitate out within a few hours, according to modeling studies such as Jensen et al. (1996), but the remaining smaller crystals can form an optically thin cirrus cloud that may persist long after the underlying cumulonimbus has dissipated and be advected to regions far removed from the original convection.

The second mechanism for TTL cirrus formation is that it is accomplished in situ when the ascent of a moist layer takes place on a synoptic- or planetary-scale. The lower temperatures created by this rising motion can cause the layer to become supersaturated with respect to ice, and homogeneous freezing of aerosols and ice crystal formation can occur. This produces an optically thin cloud in the ascending layer, and if the fall rates of the ice crystals are slow enough, the cloud can persist for several days. In this mechanism, the coldness of the TTL (particularly over the warm pool region) is an important contributing factor — larger numbers of ice crystals are produced at lower temperatures, which increases the competition among the crystals for the ambient water vapor and results in overall smaller crystals. The requirement for extremely low temperatures also explains why extensive tropopause cirrus is not observed in mid-latitudes (Jensen et al. 1996).

Both of the above mechanisms are believed to be at work in the production of tropical cirrus (Winker and Trepte 1998; Massie et al. 2002; McFarquhar et al. 2000, and references therein). Once formed, thin TTL cirrus layers can potentially persist for days, until they receive sufficient heating from either absorbed solar radiation or external dynamical processes, such as large-scale subsidence or perturbations due to gravity waves, to dissipate (Jensen et al. 1996).

To force in situ cirrus formation in the manner described above, a region of ascent within the TTL is required. Modeling studies dating back to Matsuno (1966), Webster (1972), and Gill (1980) have investigated the atmosphere's response to diabatic heating in the upper troposphere. An example of the resulting geopotential height and wind perturbations is displayed in Figure 1.2 (originally Figure 1.8 in Dima 2005). For this figure, an equatorial heat source (in colors) was used to force the nonlinear shallow water wave equation of Van Tuyl (1986). In response to the heat source, an eastward-propagating equatorially-trapped Kelvin

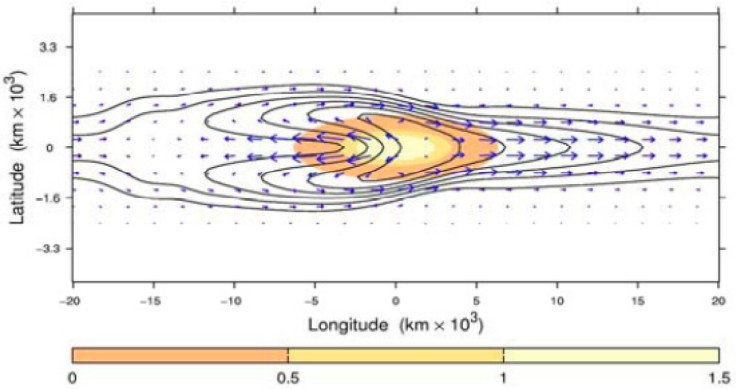

Figure 1.2 Non-linear solution of the shallow water wave equation forced by an equatorial heat source (indicated in color). Contours indicate the geopotential height field; the wind field is represented by arrows. Image courtesy Dima (2005).

wave with associated westerly winds develops to the east of the heat source, and a westward-propagating Rossby wave is observed to the west of the heat source, with anticyclonic gyres flanking the equator and easterlies along the equator. Dima (2005) has speculated that the extreme coldness of the TTL over the warm pool region might be related more to the slow ascent within waves of this type than to convective updrafts. Figure 1.3 (originally Figure 9 in

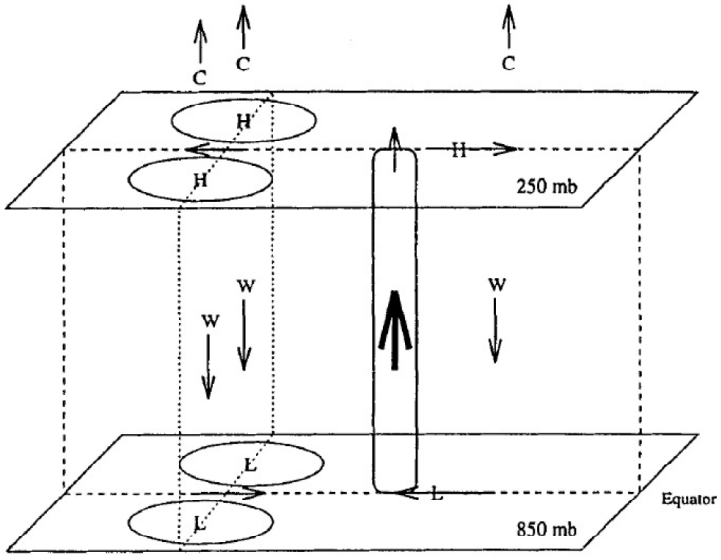

Figure 1.3 Schematic of the idealized equatorial atmosphere's response to convective heating within strong ascent (indicated by the bold arrow). H and L refer to pressure anomalies, while W and C indicate temperature anomalies. Image courtesy Highwood and Hoskins (1998).

Highwood and Hoskins 1998) shows a schematic that includes the temperature anomalies and vertical motions expected in various regions of the waves. Anomalously low temperatures and ascent should be observed above the level of maximum amplitude of these waves in the geopotential height and zonal wind fields. The formation and dissipation of TTL cirrus detected above the warm pool by a ship-based lidar during a boreal winter field campaign were observed to be controlled by the passage of convectively-induced perturbations in the TTL, with Kelvin wave packets exerting the stronger influence (Fujiwara et al. 2009).

Examining the radiosonde and lidar data from the ARM site at Nauru (see Section 2), Boehm and Verlinde (2000) found that TTL cirrus are detectable only during the cold phases of Kelvin waves propagating downward from the lower stratosphere into the TTL and that the temperature anomalies associated with those perturbations are in excess of 4 K. The waves they observed had 5–10 day periods; because of the limited data available, they were unable to investigate any relationship between cirrus and perturbations in the TTL with time scales longer than that. Similar results were obtained by Immler et al. (2008) based on lidar observations over Suriname.

TTL cirrus are often geometrically, as well as optically, thin. McFarquhar et al. (2000) observed mean geometric thicknesses near 0.47 km for cirrus near the tropopause during CEPEX; Winker and Trepte (1998) reported layer thicknesses between 0.25 km and 1 km for TTL cirrus identified by a space shuttle-borne lidar. These observations suggest that TTL cirrus are associated with perturbations that have short vertical wavelengths. Smaller-scale processes that could give rise to thin layers of cirrus are the subject of ongoing research. Results of a recent modeling study suggest that once a thin TTL cirrus cloud layer has formed, a cloud-scale circulation is induced with inflow at the bottom of the cirrus cloud and outflow

near the top. If the inflowing air is sufficiently moist, this cloud-induced circulation creates a mechanism for the cloud to become self-sustaining (Durran et al. 2009).

Variability in the tropical troposphere on intraseasonal time scales (roughly 20–60 days) is dominated by the Madden-Julian Oscillation (MJO, alternately referred to as an intraseasonal oscillation, ISO; Zhang 2005). Originally, the MJO was recognized in surface pressure data as a region of disturbed weather that appears first over the Indian Ocean and propagates eastward along the equator into the western and central Pacific. Accompanying the surface low are convective anomalies, low-level convergent winds, and a planetary-scale zonal circulation with strong upper tropospheric zonal wind anomalies (Madden and Julian 1971 and 1972; Zhang 2005).

Madden and Julian (1972) suggested that the convective centers might be accompanied by an eastward-propagating wave near the tropopause that circumnavigates the globe. Subsequent research has identified such a feature in the upper level divergent component of the wind field (Knutson and Weickmann 1987), in Microwave Sounding Unit channel-2 temperatures (Hendon and Salby 1994), and in upper tropospheric/TTL relative humidity (Eguchi and Shiotani 2004). The feature documented by Knutson and Weickmann (1987) was observed to circumnavigate the globe. Hendon and Salby (1994) identified two classes of perturbations within the TTL in response to MJO convection, one of which, a coupled Rossby-Kelvin wave similar to that of Gill (1980), migrates eastward along with the convective anomaly, and the other, a Kelvin wave, propagates eastward more quickly than the convection and can be tracked as it propagates into the western hemisphere. A relationship between TTL cirrus and the MJO has also been demonstrated. In an analysis of five separate MJO episodes, Eguchi and Shiotani (2004) observed cirrus at the 100 hPa level to the east of the convective

anomaly as it propagated into the western Pacific. They attributed the occurrence of the cirrus to the low temperatures produced by the convective system.

Global, vertically resolved views of TTL cirrus obtained from instrumentation carried aboard the CALIPSO satellite, launched in 2006, offer an unprecedented opportunity to investigate many aspects of TTL cirrus and its relationship with, and influence upon, the tropical atmosphere. The remainder of this thesis will be organized as follows: Section 2 will include details about the data sources and statistical analyses. In Section 3, we will use CALIPSO cloud profiles to examine two major proposed formation mechanisms for tropical cirrus. Section 4 will present our investigation of the vertical structure and characteristic magnitude of the temperature anomalies associated with tropical cloudiness. In Section 5, we will document the planetary-scale environment and circulations that exist in conjunction with TTL cirrus. A possible connection between TTL cirrus and the MJO will be explored in Section 6. Section 7 will include preliminary analysis of the annual and interannual variability of TTL cirrus. Discussion and concluding remarks will be presented in Section 8.

SECTION 2: DATA AND ANALYSIS TECHNIQUES

a. Data sources

The Cloud-Aerosol Lidar with Orthogonal Polarization (CALIOP) aboard the polar-orbiting Cloud-Aerosol Lidar and Infrared Pathfinder Satellite Observations (hereafter, this data source will simply be referred to as CALIPSO; see Winker et al. 2007 for a description of the instrumentation) has been gathering vertical profiles of clouds and aerosols around the world since June 2006. The satellite's orbital paths are such that it crosses the equator at over 230 discrete longitudes each during day and night; each of these orbital paths is traversed once every 16 days. CALIPSO data have high spatial resolution — 5 km in the horizontal (along-track) and 60 m in the vertical for the altitudes of interest (Winker et al. 2007). We will consider data from roughly the first 24 months of CALIPSO's operations (June 2006–June 2008).

The CALIPSO-acquired measurements that will be examined for this project are the cloud base and top heights, which are derived using an algorithm that identifies regions in which the attenuated scattering ratio of the lidar return signal exceeds altitude-dependent threshold values which are themselves functions of backscatter variability. A horizontal averaging scheme is also employed to identify extensive, faintly-scattering layers. These measurements provide a two-dimensional view of cloud occurrence (along-path location vs. altitude). The lidar is able to detect both cloud and aerosol layers, and NASA operates a cloud-aerosol discrimination (CAD) algorithm based on histograms of known scattering properties to classify each layer (algorithm documentations can be found at Atmospheric Science Data Center 2009). For the purposes of this study, we accept these layer boundaries and classifications at face value.

Following Fu et al. (2007), a cloud base at the Earth's surface is assigned to opaque cloud layers. In effect, we assume that clouds that are optically thick enough to fully attenuate the lidar beam are deep convective clouds, which normally have low-altitude bases. This assignment will doubtless result in a degree of overestimation of cloud fraction at low altitudes but will have essentially no impact on the description of the high-altitude cirrus with which we are concerned.

Because of background solar radiation, daytime lidar measurements contain much more noise than those acquired at night, making the determination of precise cloud boundaries and the detection of faint features more difficult during daytime orbits. The detection of faint features is of particular significance for this study, because the clouds with which we are concerned are often optically thin. In order to deal with this limitation, most analyses documented in this thesis have been performed separately using nighttime and daytime lidar data. If the two results differ significantly, we present them separately and place more confidence in the results obtained using the nighttime data. More often, the end results are qualitatively similar, and in such cases we combine the two to obtain a larger sample size.

To investigate the atmospheric conditions observed in conjunction with TTL cirrus, we will use variables from the initial analyses of the Global Forecast System (GFS) model, which is operated by the National Centers for Environmental Prediction (NCEP). GFS output resolution is 1° in the horizontal, spanning the entire globe, and in the vertical data are available at 27 standard pressure levels from sea level through the stratosphere (Seo et al. 2005). Operational analyses are produced four times daily (00Z, 06Z, 12Z, and 18Z).

The GFS output variables analyzed in this study are temperature, zonal and meridional wind, vertical velocity in pressure coordinates (ω), relative humidity (at 300 hPa only), and geopotential height at the 300, 250, 200, 150, 100, 70, and 50 hPa levels, which roughly

correspond to altitudes of 9.7, 10.9, 12.4, 14.2, 16.6, 18.6, and 20.6 km, respectively, and span the upper troposphere, TTL, and lower stratosphere. We focus on latitudes equatorward of 30° (hereafter, the term "tropics" will refer to this region unless otherwise specified) and include data from all longitudes in order to compare conditions above the Pacific warm pool to those in other geographic regions.

Relatively data-sparse areas such as oceans and developing countries comprise the majority of the tropics. Because of this, limited numbers of in situ observations of atmospheric variables in the tropical upper troposphere and lower stratosphere are available; these are combined with more extensive satellite observations for input into the GFS model. The GFS analyses for this area are thus somewhat more dependent upon the GFS model's internal dynamics and assumptions than those in better sampled regions. It will be seen from the analyses presented in this thesis that the results obtained using GFS variables are consistent with those obtained using data from other sources.

Another data source utilized in this study is the Global Precipitation Climatology Project (GPCP). The GPCP provides gridded (2.5° latitude × 2.5° longitude) pentad precipitation rates. This data set was created by combining precipitation estimates from microwave imagers, outgoing longwave radiation (OLR) sensors, and vertical sounders aboard an assortment of satellites with ground-based rain gauge data (Adler et al. 2003; Yin et al. 2004). As of the time of analysis, GPCP data were available only through the end of April 2008.

In addition, data from two locations in the tropical western Pacific (TWP) are analyzed in this study. These observing sites are maintained by the Atmospheric Radiation Measurement program (ARM), which is conducted by the United States Department of Energy. Operations at Manus Island, Papua New Guinea (2.060°S, 147.425°E), began in fall 1996, and

the Nauru observation site (0.521°S, 166.916°E) was established in summer 1998 (Mather et al. 1998; see Section 4 for a map of the ARM locations).

Although a variety of instruments are deployed at the ARM observation sites, only radiosonde data from the period following CALIPSO's launch are used in this study, and of the variables measured by the radiosondes, only the dry-bulb temperatures will be used. Twice-daily radiosonde launches are available for both observation sites. Launch times are approximately 00Z and 12Z, which correspond to 10:00 and 12:00 local time at Manus and Nauru, respectively. A major advantage of using these soundings is their high resolution. Data are gathered every two seconds during ascent, yielding soundings with roughly 10 m vertical resolution. As a quality control, at each vertical level, temperatures farther than five standard deviations from the mean at that site and that level (in all, less than 0.2% of the total data) are discarded.

b. Analysis techniques

As mentioned in Section 1, defining a tropopause within the tropical belt is not a straightforward matter; however, when analyzing the ARM radiosonde data, it will be useful to have some measure of its height and temperature. For this reason, we identify the level with the lowest reported temperature as the cold point tropopause, provided that its altitude is at least 15 km and that the temperature profile extends at least 1 km above it. Cold point temperatures that are more than five standard deviations from the mean at each site are disregarded.

The correlation coefficient between two variables, x and y, is defined as

$$r = \frac{1}{N}\sum_{i=1}^{N}\frac{(x(i)-\bar{x})\times(y(i)-\bar{y})}{\sigma(x)\times\sigma(y)},$$

where N is the number of observations, σ is the standard deviation, and overbars indicate means. The range of values for this quantity is $-1 \le r \le 1$. A least-squares linear fit between the two variables explains a fraction of the total variance equal to the square of the correlation coefficient; the sign indicates the nature of the relationship. Throughout this study, the Student's t-statistic is used to determine the statistical significance of correlations. The effective number of degrees of freedom of the datasets used in Sections 3, 5, and 6 (after filtering and temporal and spatial averaging, as discussed later in this and subsequent sections), calculated using the formula of Leith (1973), is at least 85, which means that correlations greater than 0.22 (0.28) in absolute value are significant at the 95% (99%) level when a two-sided distribution is assumed. Most of the relationships of interest in this study have correlation coefficients much higher than these threshold values. In Section 4, neither filtering nor time averaging is applied to the data, yielding an increased sample size but greater interdependence of individual data points. We use the 95% level to evaluate the significance of these results. In Sections 4 and 6, we also linearly regress one variable onto another; the regression coefficient is the slope of the least-squares linear fit of the predictand to the predictor.

In Section 4, we make use of the Monte Carlo test of statistical significance. In that section, CALIPSO data are used to separate radiosonde and GFS temperatures into "cloudy" and "clear" subsets. The difficulty arises in determining whether the difference between the mean temperatures of these subsets has statistical significance, given the greater temperature variability in the TTL and the small cloud fraction near the top of the TTL. The Monte Carlo method involves randomly assigning radiosonde or GFS temperatures to the data in the two subsets (of the same size as the cloudy and clear subsets) and calculating the difference between the mean temperatures of the two. The randomization is carried out for a large

number of iterations (here, 1,000), and the collective temperature differences create a quasi-normal distribution. The standard deviation of this distribution can then be used to objectively infer the statistical significance of the temperature anomalies associated with cloud occurrence.

Past research has established the existence of an annual cycle in tropical tropopause height and temperature, with the highest heights and lowest temperatures observed during the boreal winter months (Reed and Vlcek 1969). The cycle was originally attributed to stronger and more deeply penetrating convection within the Hadley cell and was later linked to a stratospheric pump, driven by stratospheric waves in extratropical latitudes. Stronger pumping during the boreal winter results in lower tropical cold point temperatures, allowing for deeper convection and a higher tropopause (Highwood and Hoskins 1998, and references therein). This cycle is noticeable in the cold point temperatures at the ARM site in Manus, presented in blue in the top panel of Figure 2.1 as a seven-day running mean. Mean cold point temperatures were near −84°C for the period June 2006–June 2008, and the peak-to-peak annual cycle during this period was in the range of 6 to 7°C. The coldest tropopause temperatures during each year were observed in January–February, and February 2008 was the coldest period, with seven-day running mean cold point temperatures dropping below −93°C. The warmest temperatures were observed during August–September of each year.

Zhang (1993) found an annual cycle with similarly timed extrema in the fraction of high clouds (tops above 12.8 km) identified in OLR data from the tropics; he also reported that the annual cycle signal was stronger for clouds whose tops exceeded 15 km. The fraction of CALIPSO profiles acquired within a 10° latitude × 10° longitude region centered on Manus that identify a cloud whose base is above the 15 km level is plotted in green in the top panel of Figure 2.1. Cloud fraction is calculated as a seven-day running mean in order to not give disproportionate weight to any single CALIPSO pass over the site. The annual cycle is evident

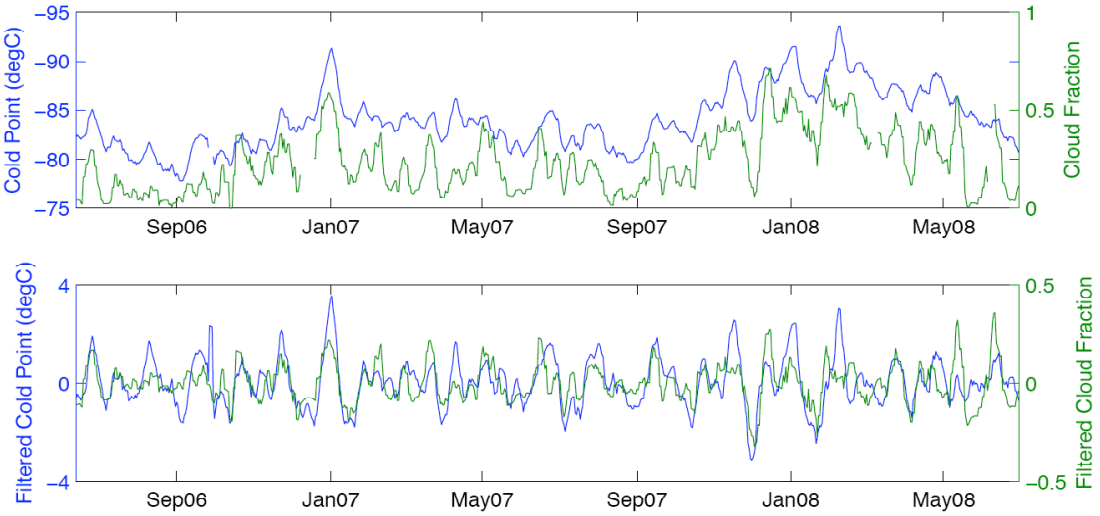

Figure 2.1 Panel A: Seven-day running mean cold point temperature at Manus (blue) and cloud fraction with base above 15 km within 10° × 10° region centered on Manus (green) during the period June 2006–June 2008. Panel B: as in panel A, but both variables have been filtered with a 60-day high-pass Lanczos filter.

in cloud fraction as well, with maximum TTL cirrus observed during the boreal winter, in agreement with previous observations of high cloud occurrence at Manus (Mather 2005). Seven-day running mean cloud fractions in Figure 2.1 range from near zero during August/September to maxima between 0.59 and 0.71 each January/February. Some interannual variability in both cold point temperature and cloud fraction is also apparent in these time series, with the winter of 2007–2008 colder, with a mean DJF cold point temperature of −88.8°C, and cloudier, with a mean DJF cirrus fraction of 0.46, than the winter of 2006–2007 (corresponding means are −84.9°C and 0.27, respectively). These differences are likely related to the pronounced La Niña event which was in progress during the former period (see Section 7 for further discussion of the influence of ENSO on TTL cirrus).

For the sake of comparison with the rest of the tropical belt, the fraction of CALIPSO profiles gathered equatorward of 20° latitude that identify a cloud whose base is above the 15, 16, and 17 km levels (depicted in blue, black, and red, respectively) for the length of the data record is shown in Figure 2.2. For this figure, in order to minimize the variability in cloudiness

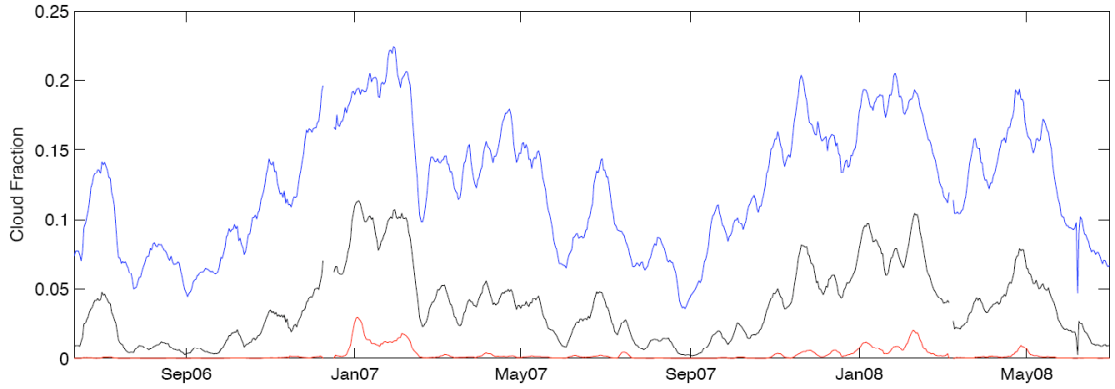

Figure 2.2 Seven-day running mean cloud fraction equatorward of 20° latitude with base above the 15 km (blue), 16 km (black), and 17 km (red) levels. Derived from CALIPSO profiles during the period June 2006–June 2008.

caused by CALIPSO's sampling of different geographic areas, cloud fraction is represented as a seven-day running mean. The annual cycle is evident at each altitude represented in Figure 2.2, with the highest cloud fractions during boreal winter and minimum cloudiness during August–September; it also increases in relative amplitude with increasing height, with a DJF/JJA ratio in cloudiness of ~2:1 at 15 km and ~4:1 at 16 km. We should note, however, that the annual cycle in TTL cirrus is by no means uniform throughout the tropics, as demonstrated in the seasonal cloud fractions presented in Figure 1.1.

Because of the similarities between cold point temperature and cloud occurrence illustrated in Figure 2.1, temporal correlation coefficients between them are strongly influenced by the variability on intraseasonal, seasonal, annual, and interannual time scales. For much of this study, we will focus on the relationship between TTL cirrus and the surrounding environment on the intraseasonal time scale; with only two years of data, quantitative study of the seasonal and interannual variability is possible only using very simple measures. For highlighting intraseasonal variability, a high-pass Lanczos filter has been applied to the GFS analyses and the CALIPSO and GPCP data as indicated. The cutoff frequency used for this filter is at 60 days. Filtered versions of the cold point temperature and cloud fraction time

series in the top panel of Figure 2.1 are shown in the bottom panel of that figure. The filtered time series are highly correlated ($r \approx -0.6$), implying a strong relationship between TTL temperatures and cirrus that we will investigate in the remainder of this thesis. Furthermore, both filtered time series exhibit a tendency for quasi-periodic behavior, with cycles about 40 days in length. A spectral peak in this frequency range is suggestive of an impact of the MJO on TTL temperature and cloud cover above Manus. The connection between the MJO and TTL cirrus throughout the tropics is explored in Section 6.

SECTION 3: FORMATION MECHANISMS

Two aspects of tropical clouds that can be studied by using CALIPSO data in isolation are their horizontal and vertical scales. Since we are most interested in the horizontal extent of TTL cirrus and the possible relationship to the underlying convection, we focus on the regions outlined in red in Figure 3.1, which is a repetition of the top panel of Figure 1.1. For each of these three regions, cloud composites are constructed in the following manner: a "composite cloud field" is determined for each CALIPSO profile gathered within the region that identifies a cloud at a specified reference altitude. The composite cloud fields extend from the ground to the lower stratosphere and from 5° south to 5° north of the profile's latitude. These composite cloud fields are then used to estimate the frequency of cloud occurrence when a cloud is present at the reference altitude. With this procedure, the point at the reference altitude above 0° relative latitude has, by definition, a cloud frequency of 1.0.

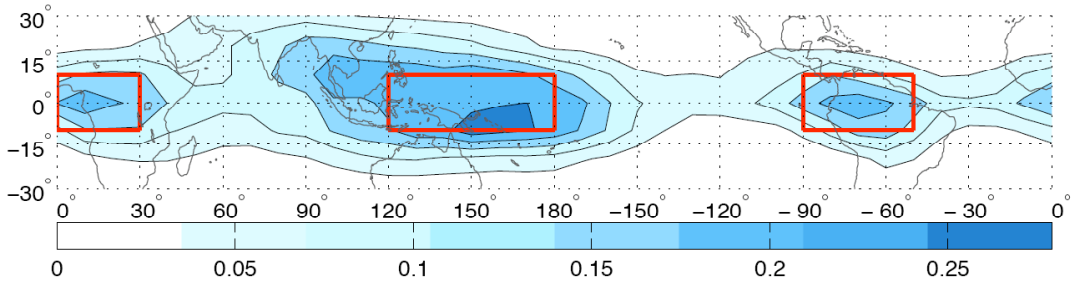

Figure 3.1 Repetition of top panel of Figure 1.1. Red rectangles identify regions to be used in composites.

Cloud composite frequencies for the warm pool region and equatorial Africa and South America are presented in Figure 3.2a (night) and 3.2b (day). The essential characteristics of the composites of the latter two geographic regions are very similar, so they have been combined and appear in the right column of Figure 3.2; warm pool composites appear in the left column. Each characteristic, similarity, and contrast documented below is observed in the individual African and South American composites and in the difference between each of them

and the warm pool composite. The reference levels used are 9 km (bottom panels), 12 km (middle), and 15 km (top). For each panel, the number of cloud fields included in the composite as a fraction of the total number of CALIPSO profiles taken during the indicated time of day within the geographic region is expressed as a percentage in the lower right corner. For example, in the uppermost left panel of Figure 3.2a, a cloud at the 15 km level was identified in 47% of the CALIPSO profiles acquired over the warm pool region during the nighttime hours (numerically, 352,045 out of 748,483 profiles, from a total of 1,667 nighttime CALIPSO passes over the warm pool).

Considering first the general characteristics of cloud frequency in Figure 3.2, we observe that for each category, the fraction of CALIPSO profiles used is larger for the warm pool region than for equatorial Africa and South America, indicating higher overall cloudiness in the upper troposphere and TTL in that area. In general, the fraction of profiles identified as cloudy increases with height. For all panels, the relative cloud fractions decrease rapidly above the 15–16 km level, in agreement with the findings of Fu et al. (2007) and others that mean cloud fraction in the tropics exhibits a mid-tropospheric minimum around 8 km, an upper tropospheric maximum near 14 km, and a rapid decrease with height above that level. If we take the altitude of the highest extent of the 50% contour as the mean cloud top height, we find that cloud tops identified during the nighttime passes are in all cases higher than those identified during the daytime passes; likewise, mean cloud top height is for each category higher over the warm pool region than over equatorial Africa and South America.

More CALIPSO profiles were classified as cloudy at the reference altitude during the night than during the day in every case in Figure 3.2. The percent difference between the fraction of included nighttime and daytime CALIPSO profiles increases with altitude but is at all altitudes larger for equatorial Africa and South America than for the warm pool region.

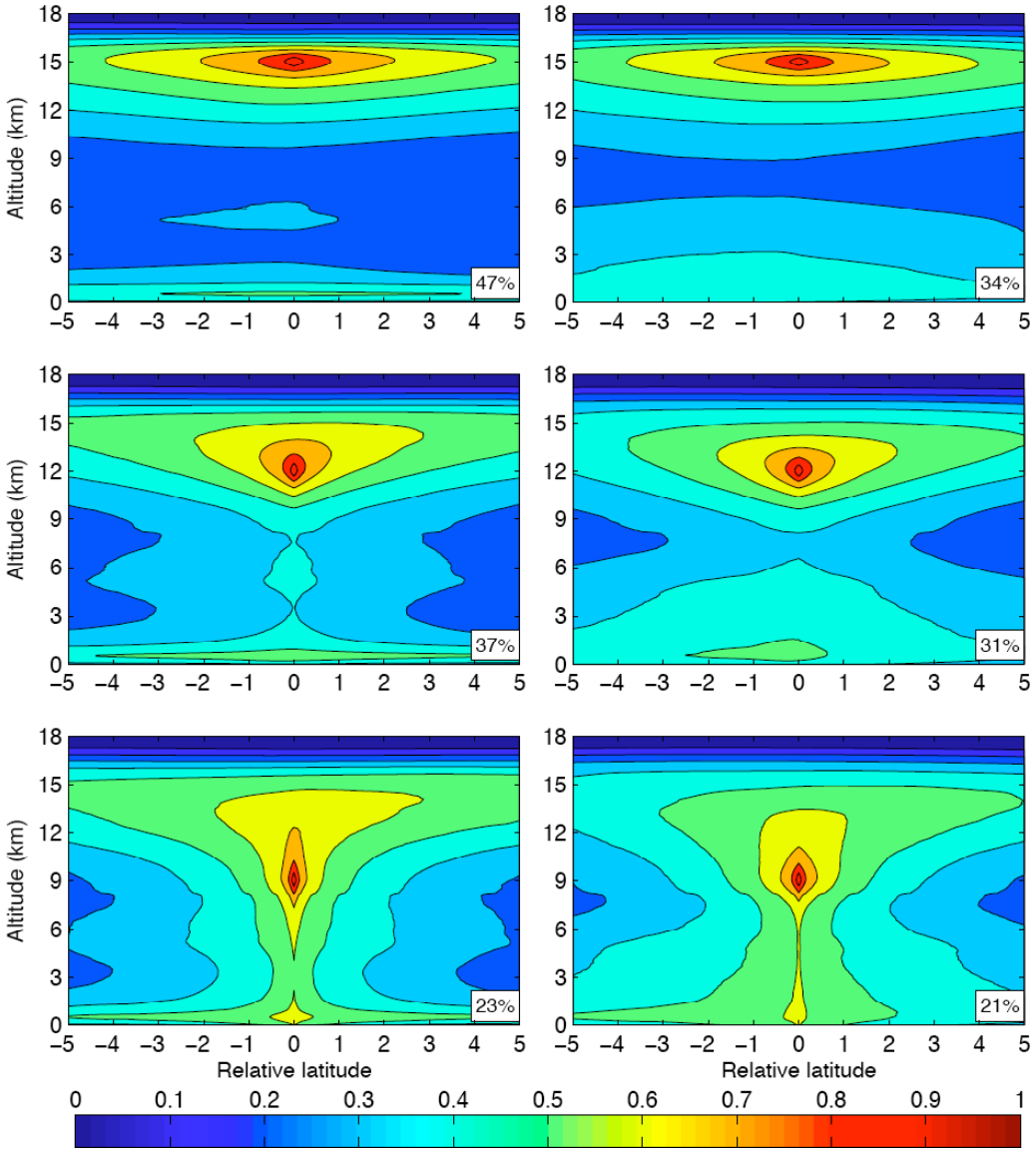

Figure 3.2a Altitude-relative latitude plots of relative nighttime cloud fraction based on CALIPSO profiles (see text for methodology) for the warm pool region (left column) and equatorial Africa and South America (right column). Composites based on 15 km (top panels), 12 km (middle), and 9 km (bottom) reference altitudes. Percentage of profiles used is in lower right corner. Contour interval is 0.1.

Considering, however, the uncertainties involved in cloud detection, particularly of optically thin layers, during the daytime hours (see discussion in Section 2), it is possible that these differences can be partially attributed to the CALIPSO instrument itself rather than the actual effects of the diurnal cycle.

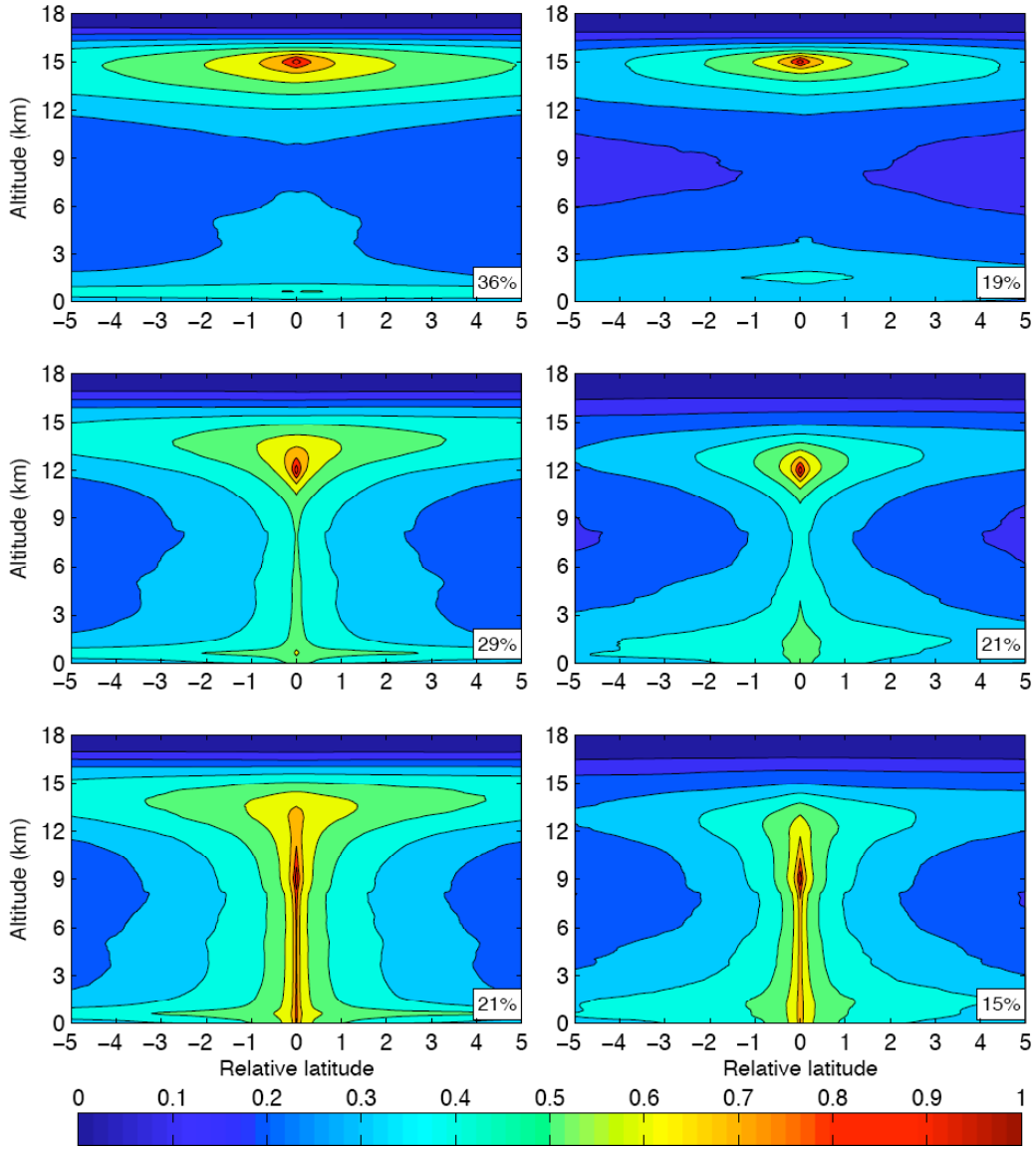

Figure 3.2b As in Figure 3.2a, but for daytime conditions.

The bottom panels in Figure 3.2 show the 9 km composites. The convective nature of many of the clouds identified is clear, with relative cloud frequencies of ~80% (~60%) extending from the 9 km reference point down to the Earth's surface in the daytime (nighttime) composites. Mean cloud top height appears to be near 15 km. In the 12 km composites (the middle panels in Figure 3.2), as well as in the 9 km, the connection to the surface immediately below the reference point is stronger during the day than during the night. This distinction is

also apparent in composites constructed for other regions throughout the equatorial belt (not shown).

In contrast to the 9 km and to some extent the 12 km composites, there is little suggestion of a connection with deep convective clouds in the 15 km composites (the top panels in Figure 3.2). The cloud frequency contours are strongly elongated in the horizontal and contracted in the vertical, with the 60% contour enclosing at most an altitude range of approximately 2.5 km. While the actual horizontal extent and thickness of these clouds cannot be determined from the composites, these results are consistent with the existence of tropical cirrus layers that can stretch for hundreds of kilometers (perhaps as much as 1,000 km, Winker and Trepte 1998) — when a cloud is identified at the 15 km level, a cloud is also observed out to ±4° relative latitude and 15 km altitude about 60% of the time at night, and between 40% and 50% of the time during the day. Repeating this analysis for individual CALIPSO orbital paths passing through the warm pool region yields similar results (not shown).

One caveat to this method of determining cloud depth and horizontal extent is that, for each cloud included, CALIPSO provides only one cross-section through it. Thus, if a particular cirrus cloud originally formed by being sheared off a cumulonimbus anvil, CALIPSO would detect both cloud types only if the convection had not already dissipated and if the cumulonimbus and cirrus clouds were oriented such that both lay along the satellite's orbital path. Another limitation is that these composites do not take into account the climatological-mean vertical profile of cloud frequency. For example, a local maximum in cloud frequency at low levels is evident in all twelve panels of Figure 3.2. In the upper left panel of Figure 3.2a, a cloud is identified around 1 km above the ground out to +4° relative latitude (~450 km) in both directions almost half the time that a cloud is identified at 15 km altitude at the reference location. This feature may well be due to the existence of numerous

shallow boundary layer clouds in the warm pool region rather than a significant relationship between TTL cirrus and low-level cloudiness at such distances.

Given these limitations, we need an additional means of diagnosing the influence of both large-scale ascent and convection on TTL cirrus formation. In order to do this, we investigate the relationships between cirrus occurrence and various indicators of convective intensity (e.g., ascent in the middle troposphere) and TTL perturbations (e.g., cold point temperatures from the ARM sites). For our purposes, CALIPSO's sampling in the along-path direction (5 km) is more than ample for comparison with the more coarsely gridded GFS and GPCP variables. The important limitation of the CALIPSO data in this context is the irregular sampling in time. Any particular location along CALIPSO's orbital path is sampled only once every 16 days, which is not frequent enough to detect any relationship with convection or to provide a representative time series of cloudiness there.

To circumvent this limitation, we divide the length of the CALIPSO record into 107 consecutive seven-day ("weekly") segments. Dividing the tropics into a 10° latitude × 10° longitude grid, we define a TTL cirrus index (also referred to as the "cloud index" or "cloud fraction") for each week as the fraction of CALIPSO profiles acquired within each region in which a cloud deck with a base above 15 km can be identified. On average, the CALIPSO satellite passes over some portion of a 10° × 10° region in the equatorial belt five times per week. By constructing the cloud index in this manner, we are sampling only the higher TTL cirrus (cf. discussion of Figure 1.1); however, the results presented in this section are largely insensitive to modifications to the cloud index definition (such as requiring cloud base to be above 14 or 16 km rather than 15 km). In all analyses in the remainder of this section, a 60-day high-pass Lanczos filter has been applied to the time series of cloud index at each grid point and to the environmental variables.

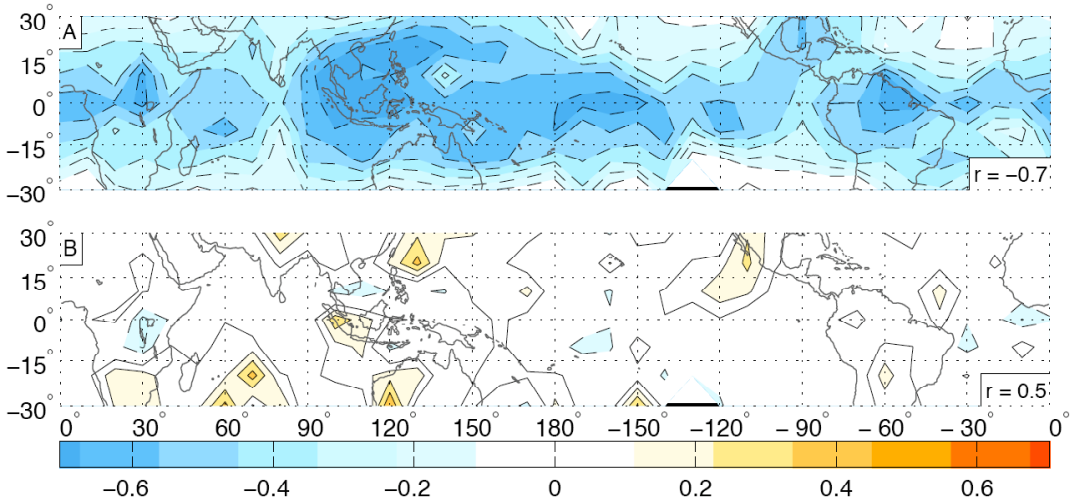

Figure 3.3 Latitude-longitude maps of grid point-wise correlations between CALIPSO 15 km base TTL cirrus index and GFS 100 hPa temperatures (panel A) and GPCP precipitation (panel B). Contour interval is 0.1. All variables have been filtered with 60-day high-pass Lanczos filter. Largest magnitude correlation in lower right corner.

As an overview, panels A and B of Figure 3.3 show the grid point-wise correlations between our TTL cirrus index and GFS 100 hPa temperatures and GPCP precipitation rates, respectively. For clarity, the strongest correlation in each panel is indicated in the lower right corner. In order to facilitate correlation with the cloud index, the 100 hPa temperatures have been averaged over each of the seven-day periods, which has the effect of applying a low-pass filter to this variable. For panel B, the cloud index has been recalculated to match the pentads of the GPCP data. This reduces the average number of CALIPSO passes included in each increment in the time series to four. Both the GFS and GPCP variables have been regridded to match the spatial grid of the cloud index.

It is evident from the top panel in Figure 3.3 that correlations between the TTL cloud index and GFS 100 hPa temperatures are negative throughout the tropics and are largest in magnitude above equatorial Africa, the Maritime Continent, the western to central tropical Pacific, and equatorial South America, which correspond roughly to the regions of maximum cloud occurrence in Figure 1.1. In contrast, the relationship between TTL cirrus and

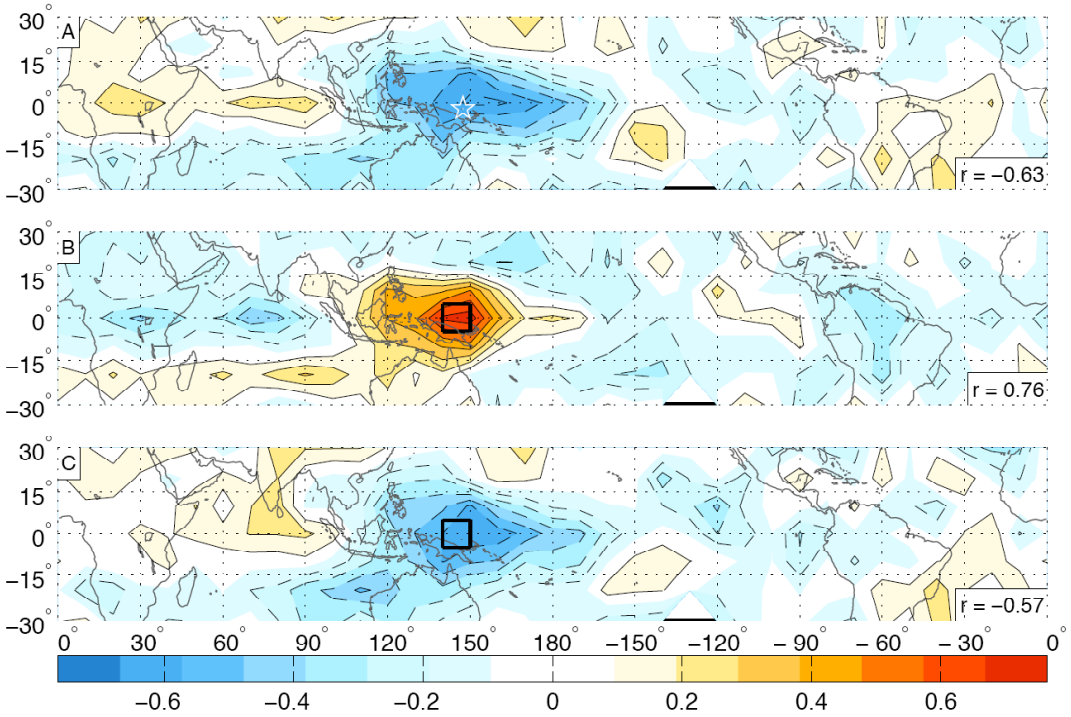

Figure 3.4 Latitude-longitude maps of correlations between CALIPSO 15 km base TTL cirrus index throughout tropics and cold point temperatures at the Manus ARM site (panel A; white star marks Manus location), CALIPSO 15 km base TTL cirrus index within reference box (panel B; reference box in black), and GFS 100 hPa temperatures within reference box (panel C). Contour interval is 0.1. All variables have been filtered with 60-day high-pass Lanczos filter. Largest magnitude correlation in lower right corner.

precipitation, as displayed in panel B of Figure 3.3, is generally weak, with correlations stronger than 0.2 in absolute value appearing only in isolated patches.

We first investigate the TTL cirrus associated with wave activity in the TTL. In Figure 3.4, the cloud index throughout the tropics is correlated with the radiosonde-derived cold point temperature at the Manus ARM site (identified with a white star in panel A), the cloud index within a 10° × 10° reference box centered near Manus (outlined in black in panel B), and 100 hPa temperature within the same box (panel C). TTL cirrus occurrence is significantly negatively correlated with both measures of TTL temperature over a broad region stretching from 120°W to the date line and poleward past 10° latitude in both hemispheres, with the strongest correlations near −0.6. The correlations are slightly stronger in panel A, in which

Manus cold point temperature is used as the reference time series, but the strong similarity between the cloud fields in panels A and C confirms that despite the coarser vertical resolution and the horizontal averaging applied, the NCEP 100 hPa temperature analyses accurately represent the temperature variations observed at Manus. Correlation of the cloud index with itself is higher in magnitude, but the cirrus signature is slightly smaller in geographic extent than in the other panels (note that the maximum correlation in panel B is less than unity because the reference box is not centered directly on a grid point of the tropical cloud index).

Figure 3.5 extends the analysis of Figure 3.4 to other tropical regions by correlating 100 hPa temperatures from the NCEP analyses averaged over five different reference boxes (outlined in black) with the gridded cloud index throughout the tropics. These reference boxes have been chosen to represent the three areas of maximum TTL cirrus occurrence — Africa, the Maritime Continent and western Pacific, and South America (compare with Figure 1.1). In each panel, 100 hPa temperature is significantly negatively correlated with TTL cirrus not only within the reference box, but over geographic regions sometimes exceeding 50° of longitude and 30° of latitude. This indicates ascent within the TTL throughout a broad, planetary-scale region.

Above the Maritime Continent and the western Pacific (panels B through D), the cirrus fields in Figure 3.5 assume roughly similar shapes. A nose of negative cirrus correlations extends along the equator eastward from the reference boxes; to the west of them, the stronger cirrus signals are centered between 10° and 20° north and south of the equator. Positive (though weaker) TTL cirrus anomalies are discernible to the east and/or west of the primary negative correlation centers in all panels of Figure 3.5.

Another measure of ascent within the TTL is the GFS's 100 hPa omega field. One-point correlations of ω (within the reference boxes) with the TTL cirrus index throughout the

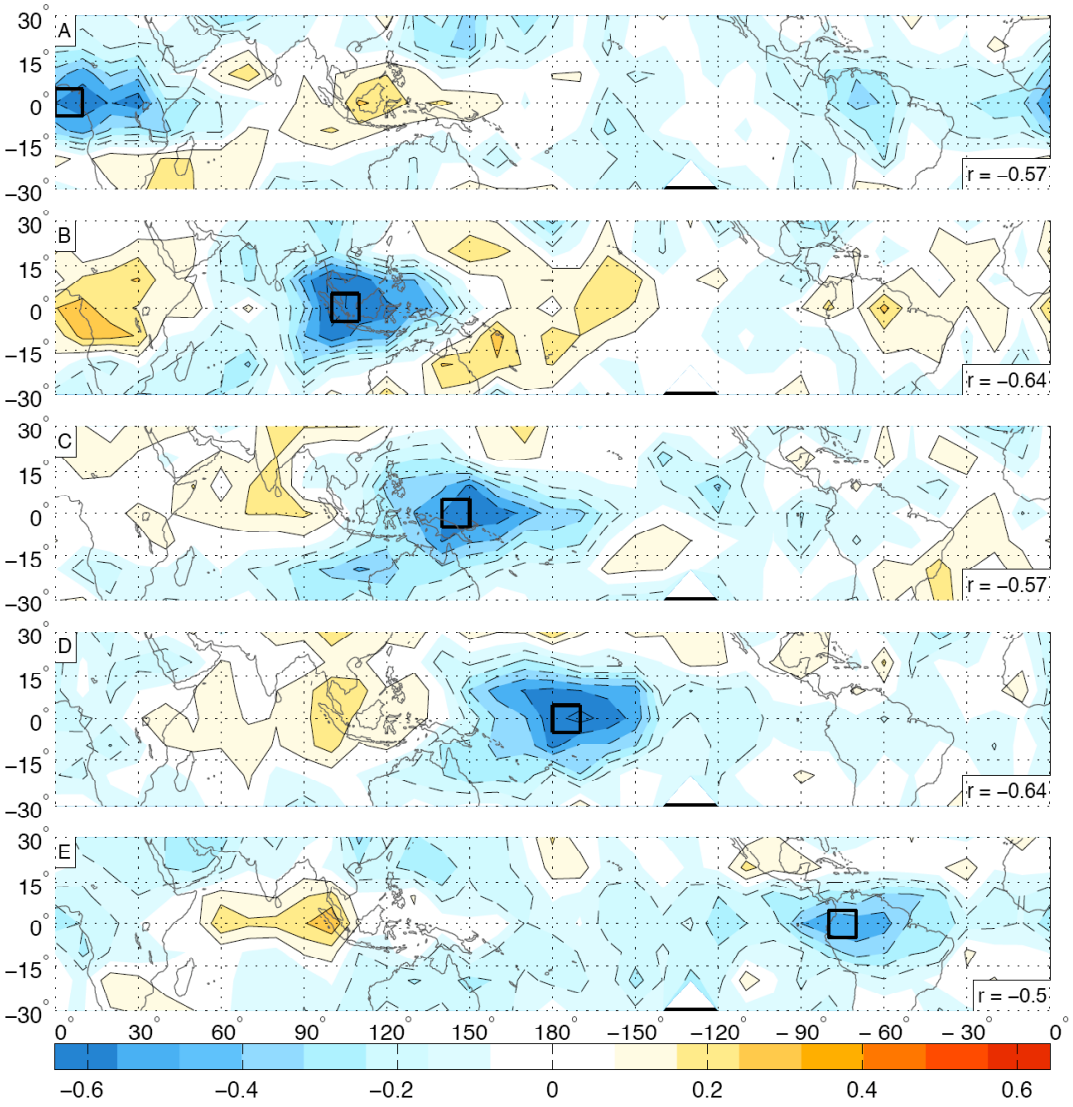

Figure 3.5 Latitude-longitude maps of correlations between GFS 100 hPa temperatures within black reference boxes and CALIPSO 15 km base TTL cirrus index throughout tropics. Contour interval is 0.1. Both variables have been filtered with 60-day high-pass Lanczos filter. Largest magnitude correlation in lower right corner.

tropics are plotted in Figure 3.6. The occurrence of TTL cirrus is significantly correlated with ascent at the 100 hPa level, but the correlations are weaker and do not extend over so broad a region as those with 100 hPa temperature. There is little consistency in the extent or orientation of the cirrus anomalies in Figure 3.6.

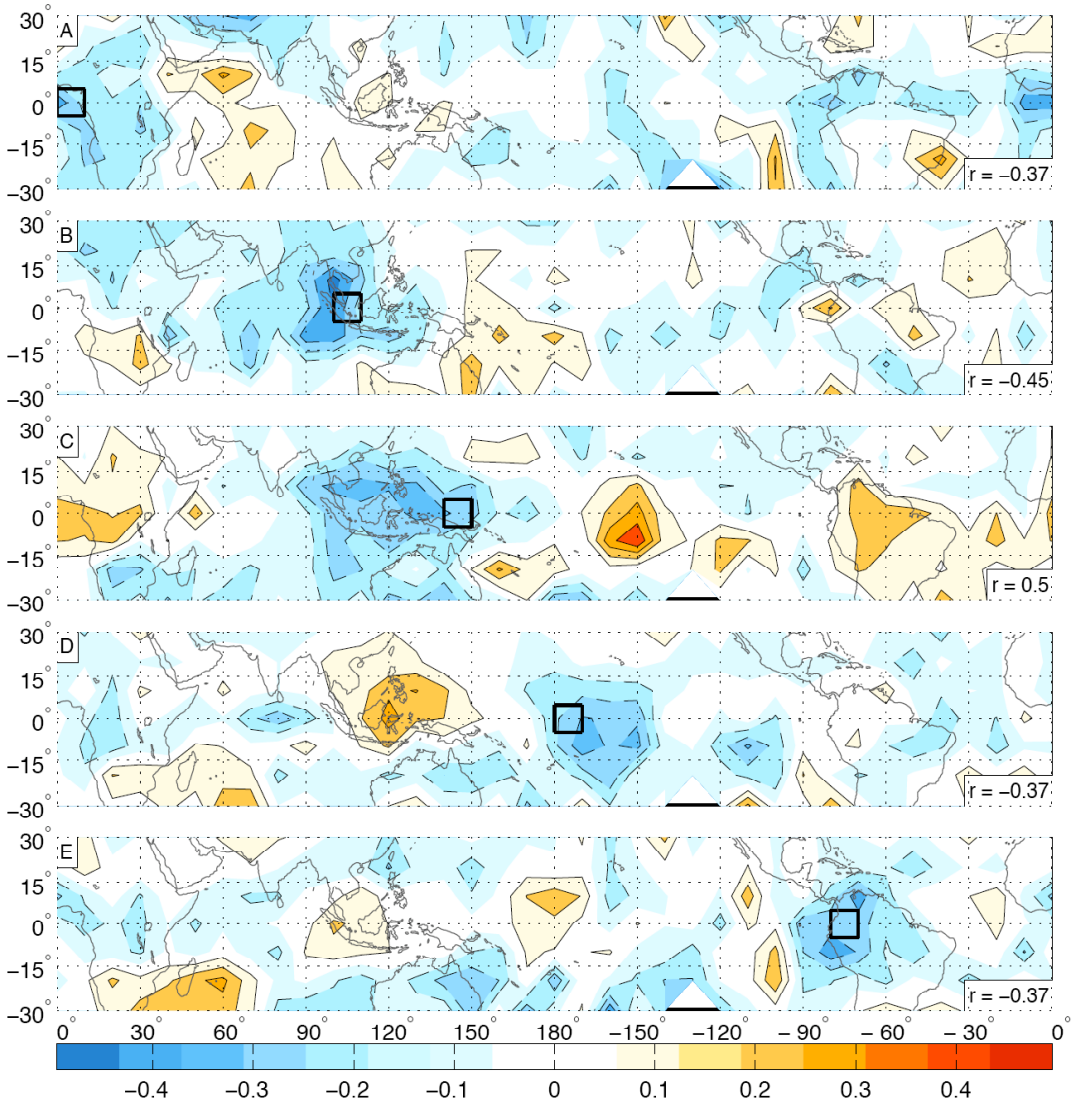

Figure 3.6 Latitude-longitude maps of correlations between GFS 100 hPa omega within black reference boxes and CALIPSO 15 km base TTL cirrus index throughout tropics. Contour interval is 0.1. Both variables have been filtered with 60-day high-pass Lanczos filter. Largest magnitude correlation in lower right corner.

As noted in Section 1, another proposed explanation for TTL cirrus formation is that the anvils of tropical cumulonimbus clouds and convective systems are sheared off and may persist for as long as several days (Jensen et al. 1996). In order to assess the relative importance of this mechanism, we repeat the analysis of Figures 3.5 and 3.6, but in place of 100 hPa temperature and ascent we will use, as indicators of convective activity, the vertical

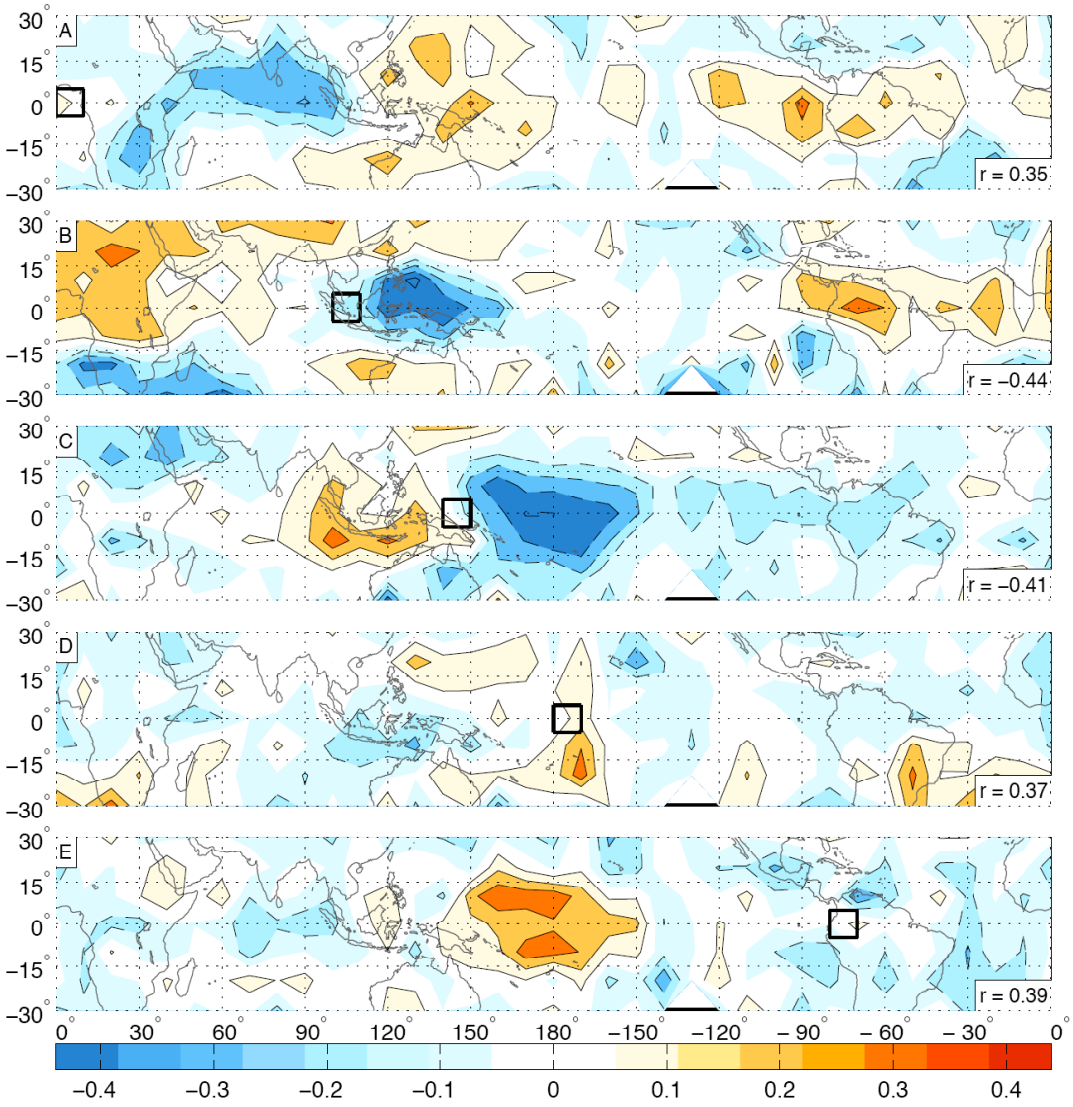

Figure 3.7 Latitude-longitude maps of correlations between GFS 300 hPa omega within black reference boxes and CALIPSO 15 km base TTL cirrus index throughout tropics. Contour interval is 0.1. Both variables have been filtered with 60-day high-pass Lanczos filter. Largest magnitude correlation in lower right corner.

motion (ω) at the 300 hPa level (~10.5 km altitude, just above the level of maximum ascent in the annual mean in the more convective regions of the tropics [Dima 2005]) and the satellite- and rain gauge-based GPCP data set, which we expect to be dominated by large convective systems.

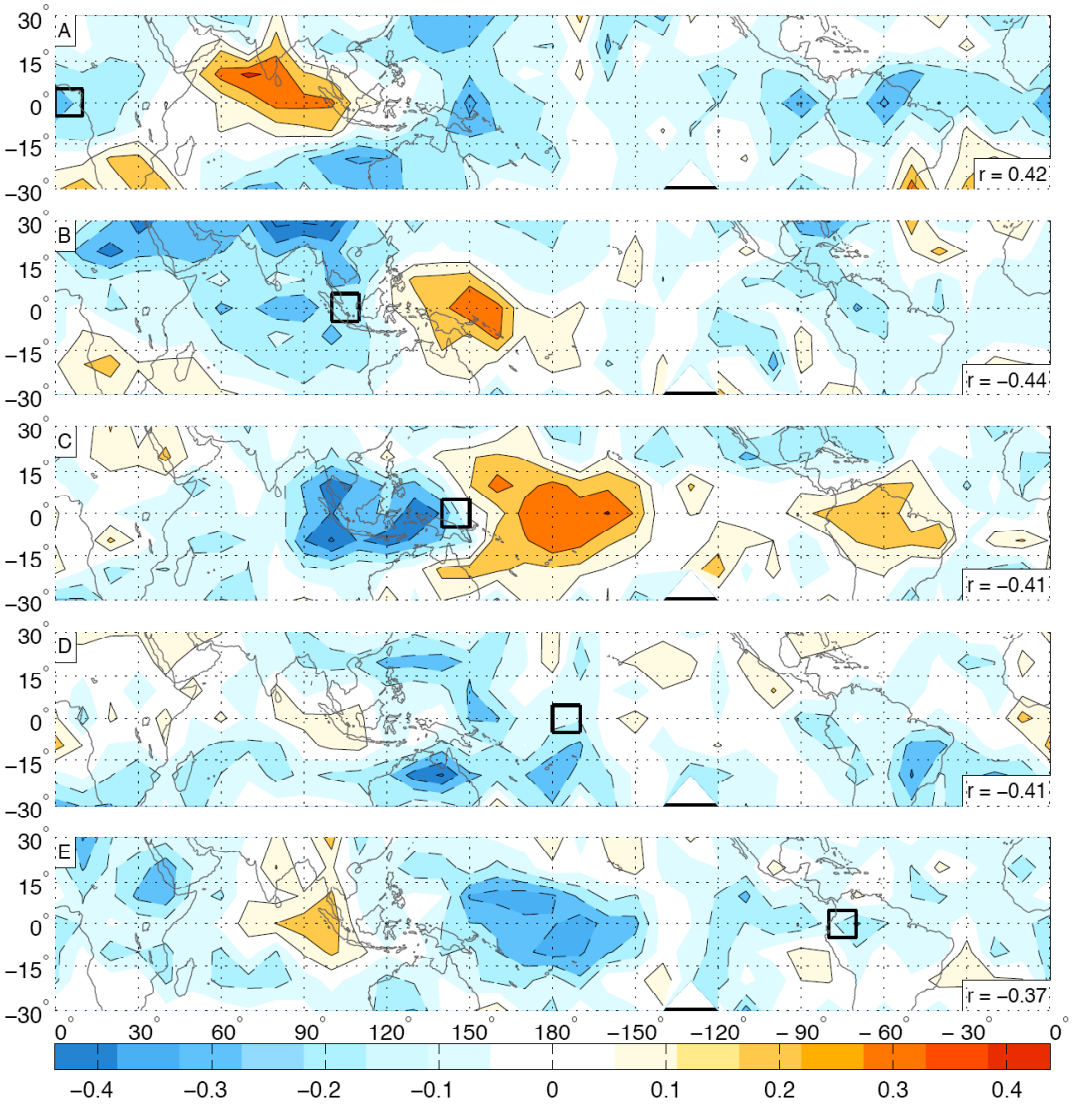

Figure 3.8 Latitude-longitude maps of correlations between GFS 300 hPa relative humidity within black reference boxes and CALIPSO 15 km base TTL cirrus index throughout tropics. Contour interval is 0.1. Both variables have been filtered with 60-day high-pass Lanczos filter. Largest magnitude correlation in lower right corner.

Figure 3.7 shows correlations between 300 hPa ω within the reference boxes and TTL cirrus throughout the tropics. In panels B and C, rising motion in the middle troposphere is significantly correlated with TTL cirrus, but these cirrus anomalies are centered between 20° and 30° longitude to the east of the reference boxes; in the vicinity of the reference box itself, the correlations are weak. Cloud occurrence does not assume any discernible pattern in the

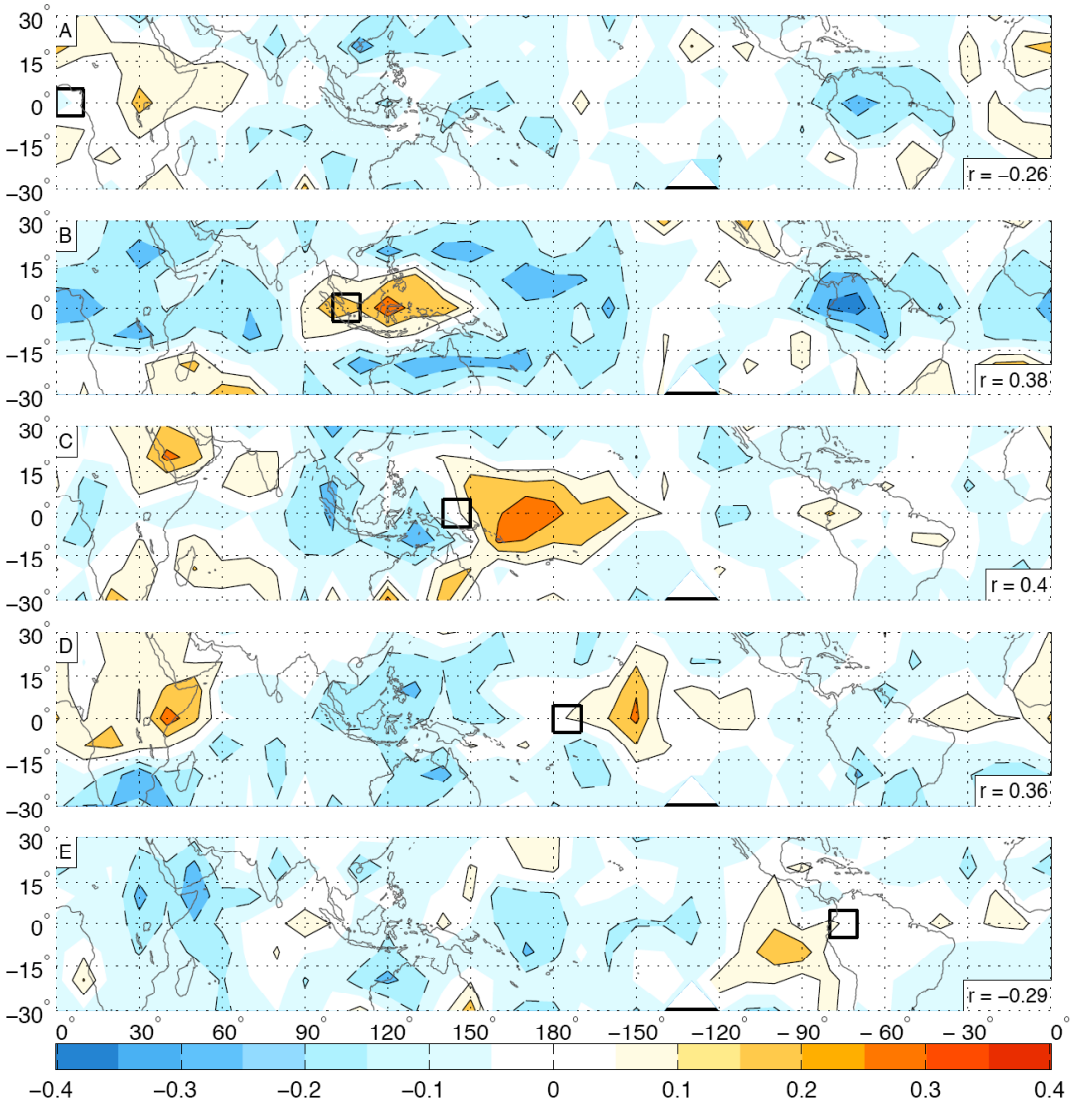

Figure 3.9 Latitude-longitude maps of correlations between GPCP pentad precipitation within black reference boxes and CALIPSO 15 km base TTL cirrus index throughout tropics. Contour interval is 0.1. Both variables have been filtered with 60-day high-pass Lanczos filter. Largest magnitude correlation in lower right corner.

vicinity of the reference boxes in the other panels of Figure 3.7. For the sake of comparison, an analogous correlation plot with GFS 300 hPa relative humidity in the reference boxes is presented in Figure 3.8. Interestingly, TTL cirrus occurrence is in each panel *negatively* correlated with upper tropospheric moisture in the immediate vicinity, though not significantly so. Positive cloud anomalies, if any, are displaced from the reference boxes.

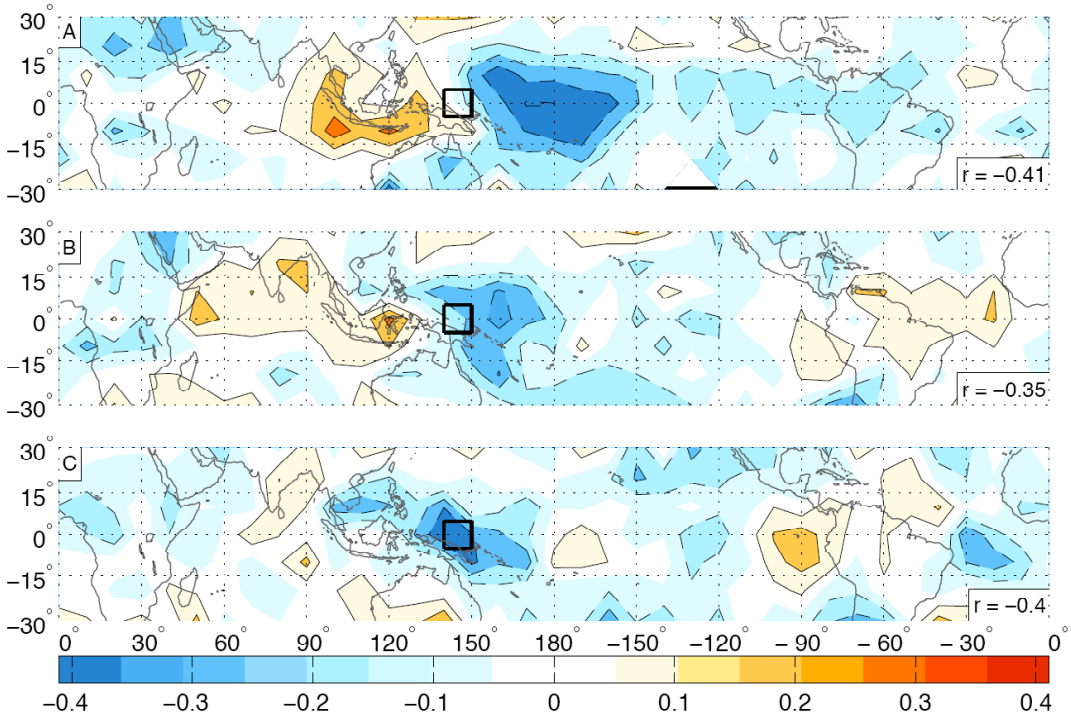

Figure 3.10 Latitude-longitude maps of correlations between GFS 300 hPa omega within black reference boxes and CALIPSO 15 km base TTL cirrus index (panel A), CALIPSO 12–15 km base cirrus index (panel B), and CALIPSO 9–12 km base cirrus index (panel C) throughout tropics. Contour interval is 0.1. All variables have been filtered with 60-day high-pass Lanczos filter. Largest magnitude correlation in lower right corner.

Figure 3.9 shows an analogous plot with GPCP precipitation used as the convective indicator within the reference boxes. In none of the panels of Figure 3.9 is precipitation significantly correlated with nearby TTL cirrus. Consistent with the other convective one-point correlation plots, the cirrus signal, if any, is displaced east of the reference box. The absence of consistent correlations between the convective and cloud indices within the reference boxes in Figures 3.7, 3.8, and 3.9 indicates that cirrus cloud formation is not dominated by the shearing of cumulonimbus anvils in regions of intense convection.

Should these results lead us to conclude more generally that sheared anvils do not play an important role in cirrus cloud formation? In order to answer this question, we modify our cloud index to capture other cirrus clouds. In Figure 3.10, we take one of our reference boxes

and correlate 300 hPa ω within it with the gridded tropical cloud index, defined as cloud fraction with base above 15 km (panel A), base between 12 and 15 km (panel B), and base between 9 and 12 km (panel C). As we saw in Figure 3.7, 300 hPa ascent and TTL cirrus are not correlated within this reference box; however, ascent is significantly correlated with TTL cirrus in the region roughly 30° to the east. At the 12–15 km level, there is weak correlation between ascent and cloud occurrence in the reference box. Cirrus clouds with bases in the 9–12 km range are significantly correlated with 300 hPa ω over an extended region. Hence, it is plausible that the shearing of cumulonimbus anvils could play an important role in cirrus cloud formation at levels below ~12 km.

Additional information regarding the relationship between TTL cirrus and both planetary wave and convective activity can be obtained by considering a vertical cross-section of the cloud field associated with each. For this purpose, we first create a height-dependent cloud index. This is defined within the same 10° latitude × 10° longitude regions and seven-day periods as our earlier TTL cirrus index but is calculated as cloud fraction within successive 200 m layers from the Earth's surface through the top of the TTL.

Figure 3.11 shows a cross section of the one-point correlations between 100 hPa temperature within our same five reference boxes (designated by the black vertical lines) and the height-dependent cloud index throughout the equatorial belt (equatorward of 5° latitude, with 10° longitudinal resolution). As expected given our results to this point, cloud fraction in the upper troposphere in Figure 3.11 is significantly negatively correlated with 100 hPa temperature. Below the ~14 km level, correlations between 100 hPa temperature and cloud fraction within the reference boxes are of small magnitude and inconsistent sign.

Above the Maritime Continent and western Pacific (panels B through D of Figure 3.11), the cloud signature within the TTL tilts eastward with increasing altitude. A marginally

significant cloud feature extending down to the Earth's surface approximately 30° of longitude to the west of the reference box indicates the location of the associated deep convection. No nearby convective signature or tilt with altitude of the primary TTL cloud signature appears in the African and South American panels of Figure 3.11.

Figure 3.12 shows an analogous plot but with 300 hPa ω as the reference variable. In each panel, a vertically aligned cloud feature exists in the reference box, although this convective signature is more apparent in panels A through C, where peak correlations are near –0.6. Given the smaller spatial scale of convection and limited spatial coverage of the CALIPSO dataset, the real correlation between ascent and collocated cloud occurrence is likely to be stronger than the results represented here. Below the 10–12 km level, the cloud field is almost completely vertical; above that level, it exhibits an eastward tilt with height. The tilting band of strong correlations should not be interpreted as indicating a continuous cloud extending from the top of the convective tower upward through a depth of several kilometers and being advected eastward over an extent of several thousand kilometers — such a feature would require cirrus layers more persistent and extensive, and stronger westerly winds and ascent within the upper troposphere and TTL, than have been consistently observed in the tropics (in fact, Massie et al. [2002] and Fujiwara et al. [2009] calculated back trajectories for air parcels containing tropical cirrus and found they had been advected by predominantly easterly winds). Even if such cirrus layers did exist, they could not be adequately sampled by CALIPSO, whose orbital paths are primarily north-south in orientation. Rather, the eastward tilt of the cloud field within the TTL should be viewed as mapping out the region of planetary-scale ascent and low temperatures within which the development of cirrus cloud decks is favored, as documented in Section 5 of this thesis.

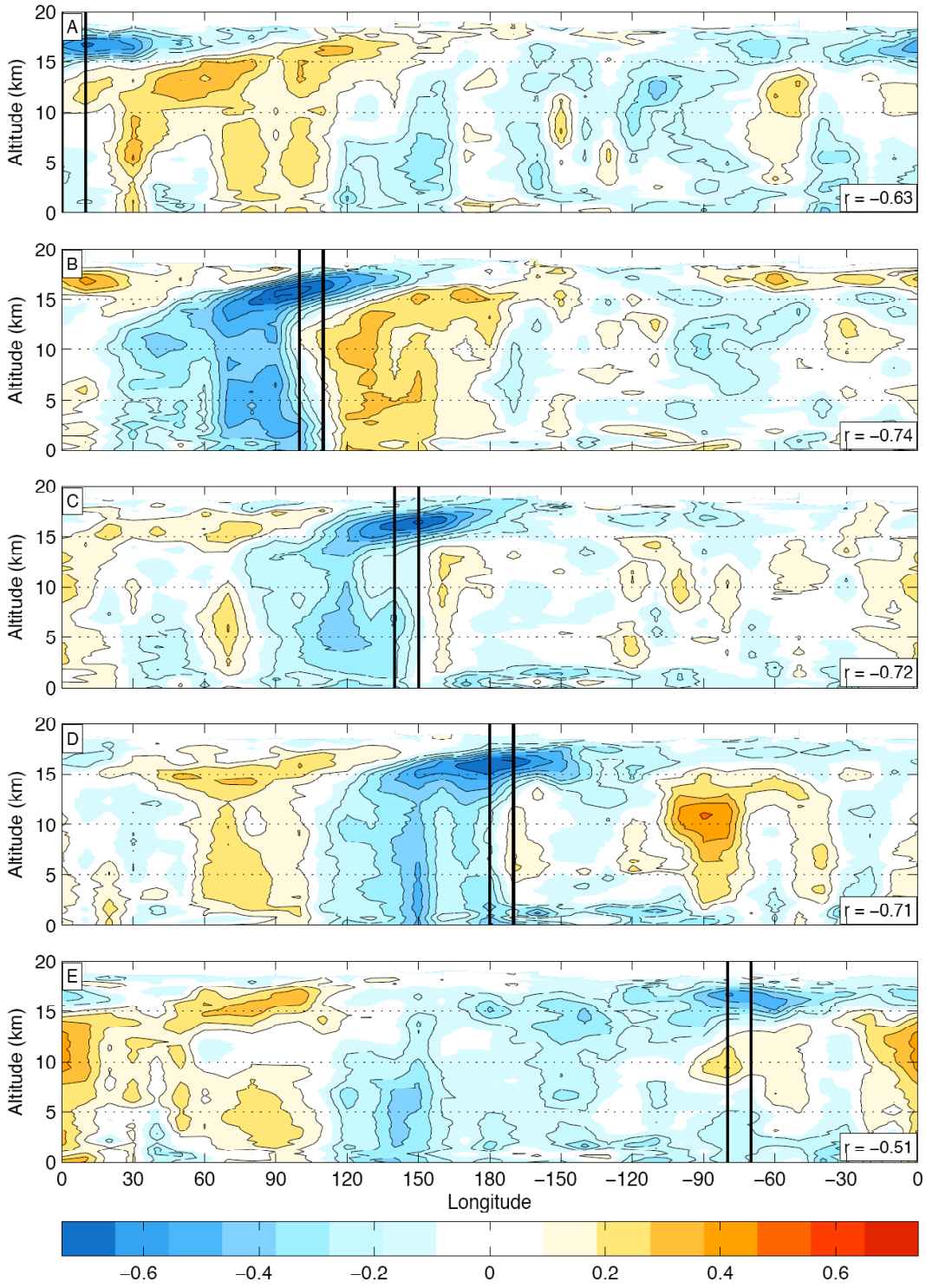

Figure 3.11 Longitude-height plots of correlations between GFS 100 hPa temperatures within 10° × 10° reference regions (black vertical lines) and CALIPSO height dependent tropical cloud index from 5°S to 5°N. Contour interval is 0.1. Both variables have been filtered with 60-day high-pass Lanczos filter. Largest magnitude correlation in lower right corner.

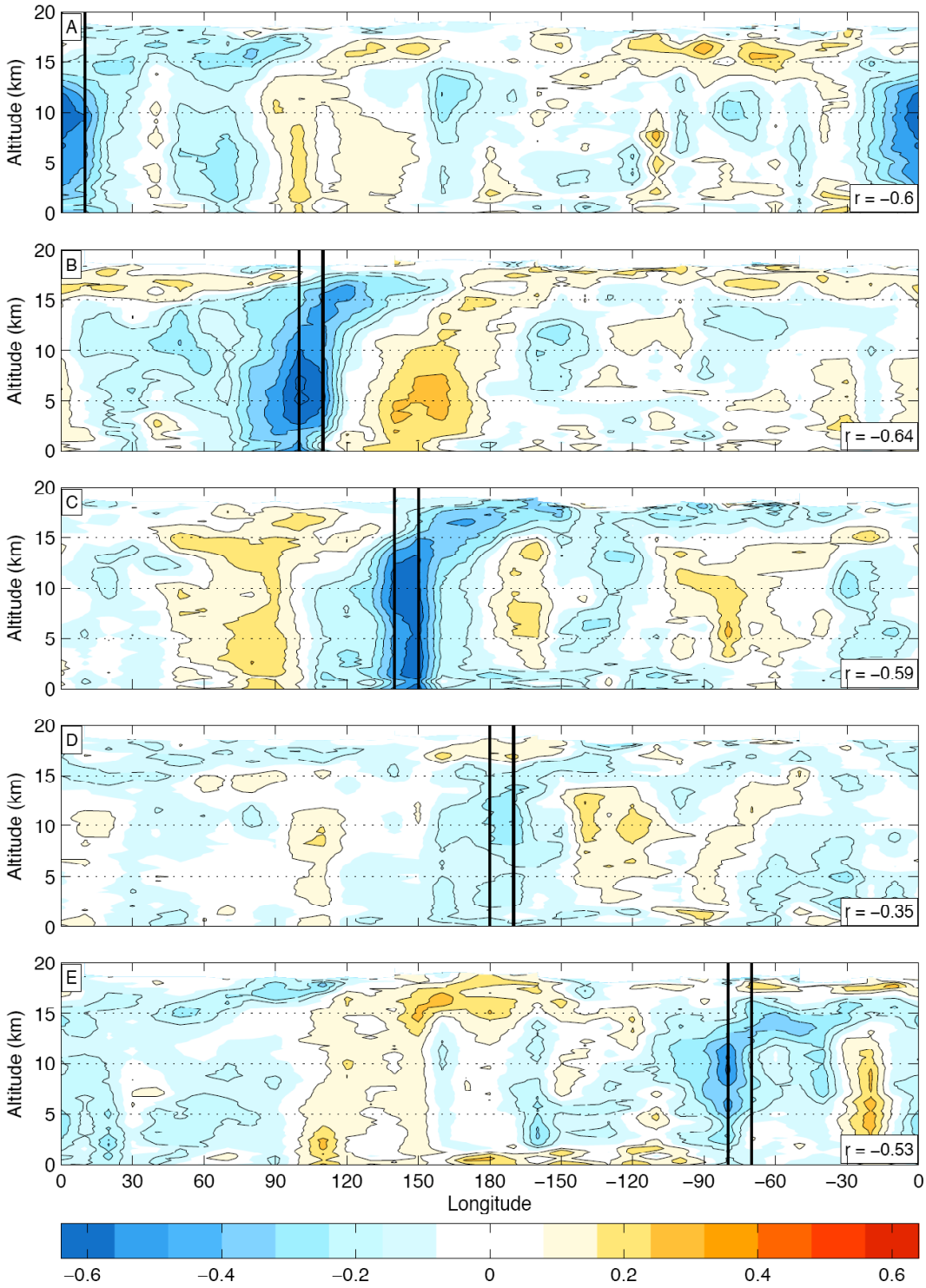

Figure 3.12 Longitude-height plots of correlations between GFS 300 hPa ω within 10° × 10° reference regions (black vertical lines) and CALIPSO height dependent tropical cloud index from 5°S to 5°N. Contour interval is 0.1. Both variables have been filtered with 60-day high-pass Lanczos filter. Largest magnitude correlation in lower right corner.

The analyses presented in Figures 3.10, 3.11, and 3.12 imply that lower altitude tropical cirrus may indeed be formed from cumulonimbus anvils, while the higher cirrus occur as a result of planetary-scale ascent in the TTL.

SECTION 4: INFLUENCE OF THE LOCAL ENVIRONMENT

Thus far, we have concluded that TTL cirrus form primarily within regions of large-scale ascent within the TTL. We now seek to identify characteristics of the local environments in which tropical clouds are observed to exist. The high vertical resolution of the ARM temperature profiles allows a more detailed study of the relationship between cloudiness and ambient conditions in the troposphere and TTL.

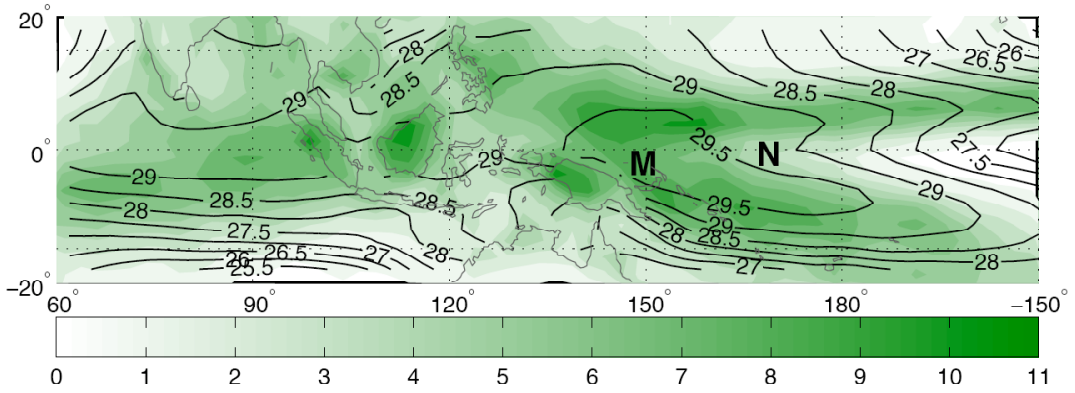

Figure 4.1 Locations of ARM sites Manus (**M**) and Nauru (**N**) in relation to GPCP mean daily precipitation (mm/day; in colors, with contour interval 1 mm/day) and mean sea-surface temperatures (°C, with contour interval 0.5°C) during the period June 2006–June 2008.

Figure 4.1 shows the locations of the ARM sites relative to the surrounding region's mean sea-surface temperatures (SSTs) and mean daily rainfall rates during the period coinciding with the CALIPSO data record. The highest SSTs and highest rainfall rates are observed in the Pacific waters surrounding Manus Island. Nauru also lies in the warm pool region, though it received less precipitation during this period than Manus and the areas just to its north and south, which were impacted by convective precipitation associated with the intertropical convergence zone (ITCZ) and South Pacific convergence zone (SPCZ).

In order to compare the ARM and CALIPSO data, we first isolate CALIPSO profiles acquired within 5° latitude × 5° longitude boxes centered on Manus and Nauru. Each site was overpassed more than 300 times between June 2006 and June 2008, with approximately half of

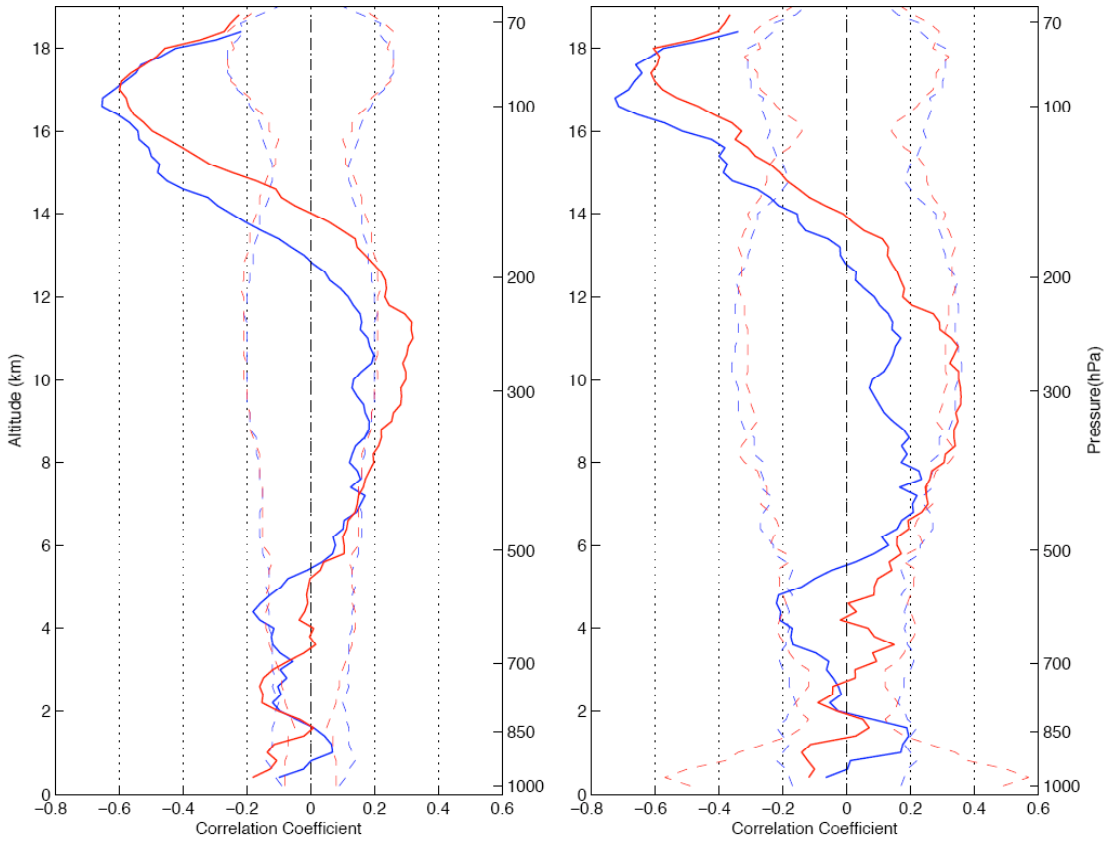

Figure 4.2 Correlations between CALIPSO-derived cloud fraction and ARM radiosonde temperatures as a function of height for the sites Manus (red) and Nauru (blue). Dashed lines show 95% significance level for each site. All months (June 2006–June 2008) included in left panel; only November–March in right panel.

the passes occurring at night. We then construct a vertical profile of cloud fraction within consecutive 200 m layers for each CALIPSO pass over each box. The closest radiosonde launch in time is designated as indicative of the environmental conditions, with the additional requirement that the launch took place within 24 hours of the time of the CALIPSO overpass. Temperatures are taken as averages over the same 200 m layers.

The left panel of Figure 4.2 shows correlations between cloud fraction and temperature at Manus (red) and Nauru (blue) as a function of altitude. The right panel of Figure 4.2 shows corresponding correlations from data gathered only during the months November through

March to ensure that the correlations are not solely due to seasonal variations in temperature or cloudiness. The 95% significance level for each site is plotted as a dashed line.

In the region between roughly the 6 and 13 km levels, correlations are predominantly positive, though weak. Only the correlations from the Nauru site with all months included are significantly positive through an extended layer; however, the prevalence of correlations of the same sign indicates that this result is more statistically significant than indicated by the Student's t-statistic test applied at individual vertical levels. Taking cloud occurrence as a proxy for rising motion, the circulations within this layer can thus be viewed as thermally direct. This observation is consistent with our understanding of the convectively-driven tropical circulations (Hartmann 1994). In describing the vertical structure of the annual-mean planetary wave structure over the warm pool, Dima and Wallace (2007) refer to the region between 400 and 175 hPa as the "middle baroclinic layer," in which thermally direct circulations result in large releases of potential energy.

Above the 14–15 km level, correlations between cloud fraction and ambient temperature become significantly negative, with values as low as –0.6 near the 17 km level in both profiles in the left panel of Figure 4.2. When considering only the November–March data, even stronger negative correlations are observed within the TTL: those from the Manus site exceed –0.7. These negative correlations are an indication of thermally indirect circulations within the TTL, in agreement with the observations of Dima and Wallace (2007), who include the TTL within their thermally indirect, baroclinic "capping layer."

Correlations such as these are instructive, but we would also like to know the magnitude of the temperature perturbations associated with cloud occurrence in the upper troposphere and TTL. As a first step toward doing so, we regress temperature onto cloud fraction at each vertical level above the ARM sites to obtain a measure of $\partial T/\partial CF$, where T is

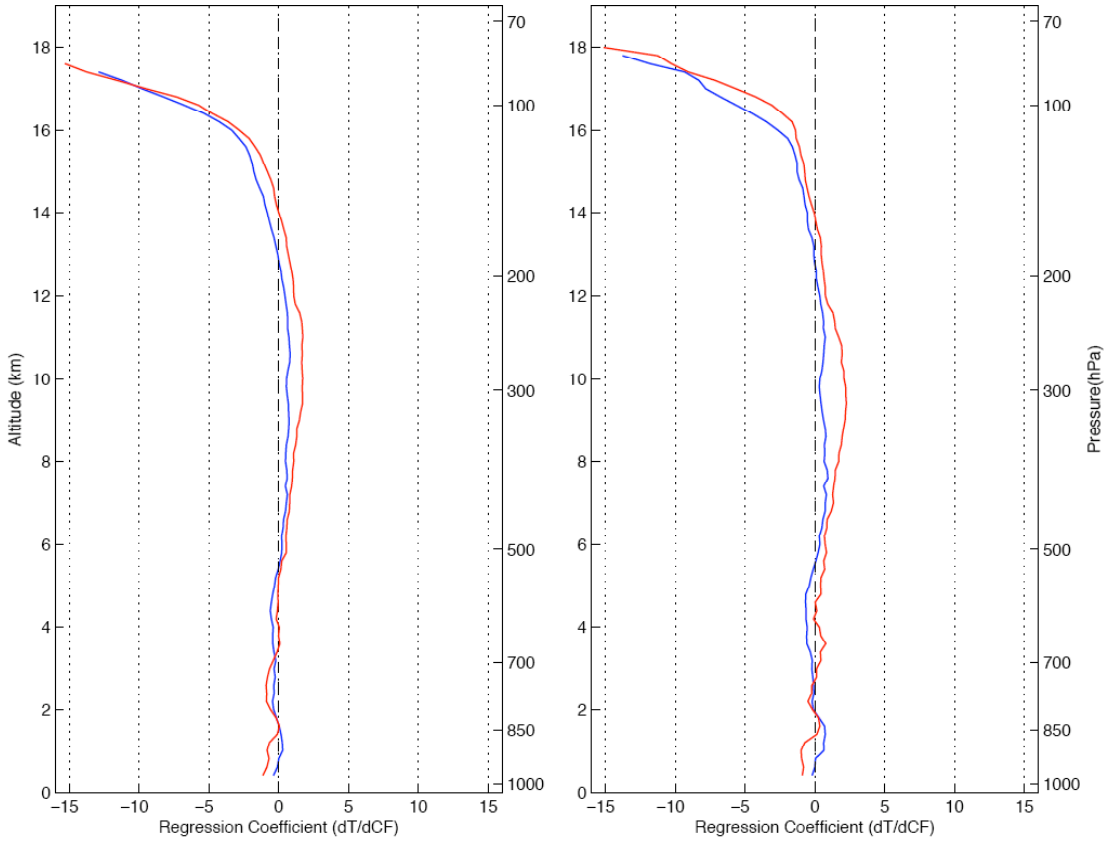

Figure 4.3 Regression coefficients between CALIPSO-derived cloud fraction and ARM radiosonde temperatures as a function of height for the sites Manus (red) and Nauru (blue). All months (June 2006–June 2008) included in left panel; only November–March in right panel.

temperature and *CF* is cloud fraction. Regression coefficients from Manus and Nauru are plotted as functions of height in Figure 4.3. Data from all months were included in the left panel; the right panel represents conditions during November – March.

Between 6 and 13 km, regression coefficients are positive and range in value between 0 and 2.5°C, indicating positive temperature differences of at most ~2°C between clear and cloudy skies. Within the TTL, the regression coefficients become strongly negative, indicating that much colder temperatures are observed when clouds are present. At 17 km, the regression coefficients are near –9.5°C (or a temperature drop of 0.95°C per 10% increase in cloud

fraction) for all months and between approximately −5.5°C and −7.5°C during the extended boreal winter months.

To further investigate the temperature anomalies associated with tropical clouds, we determine the mean cloud fraction at each vertical level for each site and then designate cloud fractions (and their associated radiosonde temperatures) less than the mean as "clear" and those greater than the mean as "cloudy." This yields an estimate of the mean temperatures observed in association with relatively clear and cloudy conditions at each altitude (irrespective of whether clouds are observed at other altitudes).

The composite temperature profiles derived from this analysis are shown in Figure 4.4. Results from Manus and Nauru are displayed in the top and bottom panels, respectively. CALIPSO passes from all months were included in the left column of Figure 4.4, while only those from November – March were used to create the profiles in the right column. Because there is general agreement between the daytime and nighttime results, the composite temperature profiles are not separated by time of day. A Monte Carlo significance test (as described in Section 2) has been performed at each vertical level. The temperature differences representing two standard deviations of the resulting distributions have been added and subtracted from the clear temperature profiles at each level and are plotted in the red dashed lines. The roughness of the cloudy profiles at higher altitudes is a reflection of the small number of radiosonde profiles that could be classified as cloudy at those levels.

Below the 14 km level, the temperature anomalies associated with greater than average cloudiness are generally positive, but no greater than 0.8°C in magnitude and are thus not discernible in this plot. This is not surprising given the relative uniformity of the radiosonde temperatures in that region — between the top of the boundary layer and the base of the TTL, the standard deviation of the temperature at any given level is only ~1°C.

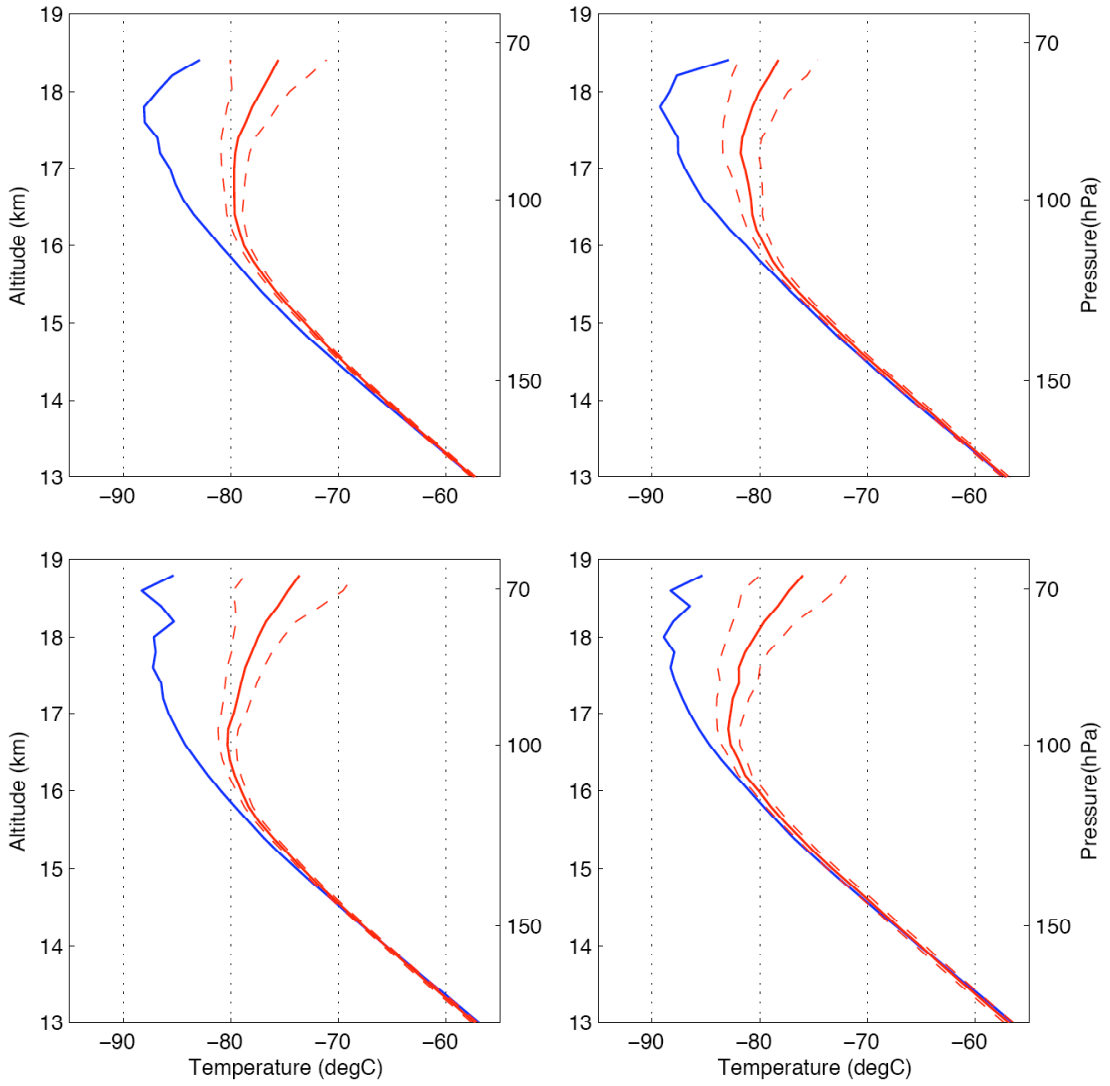

Figure 4.4 Composite "clear" (red) and "cloudy" (blue) temperature profiles, constructed from CALIPSO cloud profiles and ARM radiosonde temperatures, along with two-standard deviation temperature difference from Monte Carlo testing (red dashed; see text for methodology). Top panels represent Manus; bottom panels represent Nauru. Left panels include all months (June 2006–June 2008); right panels include only November–March.

Within the TTL, temperature differences between the cloudy and clear profiles are much larger, with the cloudy profiles being colder. For example, during November – March, at the 17 km level above Manus (Nauru), the mean cloudy temperature is 5.6°C (3.8°C) lower than the mean clear temperature, which amounts to over six standard deviations according to the Monte Carlo method. At this level, 33% (38%) of CALIPSO passes were classified as

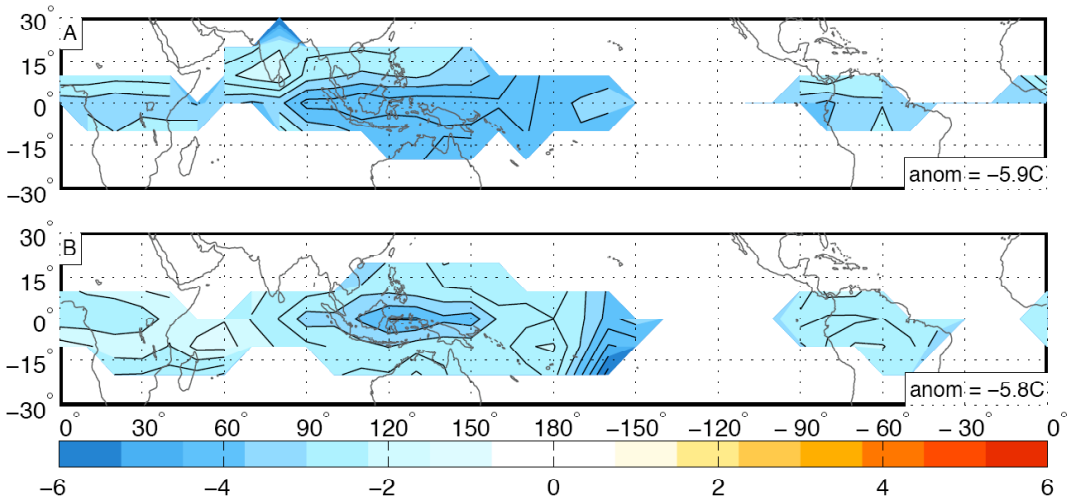

Figure 4.5 Latitude-longitude maps of temperature differences between clear and cloudy conditions at the 100 hPa level (negative values indicate colder cloudy conditions). Panel A includes all months (June 2006–June 2008); panel B includes only November–March. Contour interval is 1°C.

cloudy. To put the anomalies in perspective, the standard deviation of all wintertime temperatures at 17 km is 3.4°C (2.9°C). Even stronger negative temperature anomalies are observed at the 18 km level in Figure 4.4.

Having determined the magnitude of the temperature anomalies associated with cloud occurrence above the two ARM sites, we now seek to perform a similar analysis for the entire tropical region using GFS variables and CALIPSO data. GFS and CALIPSO data are combined in the following manner: for each run of the GFS model, we obtain 10° latitude × 10° longitude gridded 100 hPa geopotential heights and temperatures. Each orbital pass of the CALIPSO satellite is assigned to the closest GFS run in time. For 10° latitude segments along CALIPSO's path, cloud fraction is calculated within a 1 km layer centered on the altitude of the 100 hPa level. After completing this analysis, we have over 500 temperature and cloud fraction pairs for each 10° × 10° region. As with the ARM profiles above, we designate cloud fractions less than the mean for that grid box as "clear" and those greater than the mean as "cloudy."

The difference between the mean cloudy and mean clear temperatures is plotted in Figure 4.5. Panel A is calculated using data from all months, while panel B includes only November – March data. A Monte Carlo significance test has been conducted at each grid point, and only temperature differences greater than two standard deviations of the resulting distribution are plotted. In addition, regions where the mean cloud fraction at the 100 hPa level is smaller than 0.1 are ignored. Negative values prevail throughout the tropics, indicating that cloudy conditions are colder than clear conditions at the 100 hPa level. Temperature differences between 4°C and 6°C are observed above the Maritime Continent and warm pool; anomalies of such magnitude are consistent with our localized findings at the ARM sites. Over Africa and South America, temperature anomalies on the order of 2°C to 4°C are observed when clouds are present.

SECTION 5: INFLUENCE OF THE PLANETARY-SCALE ENVIRONMENT

In Section 4, we examined the local conditions associated with tropical cloudiness. We now investigate the features of the planetary-scale circulation that appear in conjunction with TTL cirrus occurrence. To this end, the analytic protocol of Section 3 is reversed, and cloud fraction within specified reference boxes is correlated with GFS variables throughout the tropical belt. In order to facilitate correlation with the cloud index, GFS variables are recalculated as the means during each of the seven-day periods over which the CALIPSO data were averaged. This has the effect of applying a low-pass filter to the GFS variables. All CALIPSO and GFS variables in this section have also been filtered using the 60-day high-pass Lanczos filter.

Figure 5.1 shows correlations between the CALIPSO cloud index within our same five reference boxes (identified as heavy black boxes) and GFS 100hPa temperatures (denoted by colors and contours) and winds (represented as arrows) equatorward of 40° latitude. The cloud index used here is cloud fraction with base above 15 km, as defined in Section 3. For smoothing and ease of viewing, GFS temperatures have been interpolated onto a 5° latitude × 5° longitude grid. As before, the strongest correlation in each panel is indicated in the lower right corner.

In each panel of Figure 5.1, TTL cirrus are clearly (and significantly) negatively correlated with 100 hPa temperatures over regions about as large as the regions of the significant cloud correlations in Figure 3.5. Above the warm pool and western Pacific regions, these correlations exceed 0.6 in absolute value. The temperature fields exhibit a high degree of equatorial symmetry throughout the tropics, and the off-equatorial features tend to be more

pronounced than in Figure 3.5. In contrast, any equatorial symmetry in the zonal and meridional wind fields disappears far away from the reference box.

Similar patterns are apparent in the temperature and wind signatures in the vicinity of the reference boxes for the Maritime Continent and western Pacific regions (panels B through D of Figure 5.1). In each of these panels, a nose of low temperatures extends along the equator to the east of the reference box. To the west, the strongest negative correlations are observed between 10° and 15° latitude in each hemisphere, straddling a band of relatively weak temperature correlations along the equator. The wind correlations are indicative of divergence in the vicinity of the reference boxes — in each panel, anomalous westerlies (easterlies) are observed along the equator to the east (west) of the reference box. These characteristics are similar to those found in the wave patterns forced by an idealized equatorial heat source by Gill (1980), Highwood and Hoskins (1998), and others (see Figure 1.2). The idealized solutions also predict ascent in the TTL within these waves in much the same areas in which TTL cirrus is evident in Figure 3.5 (compare with Figure 1.3).

There is a suggestion of a wave-train in the temperature correlations in panels A through C of Figure 5.1, with the secondary maximum correlations exceeding 0.3 in each panel. In panel A, for example, positive temperature anomalies are centered at approximately 110°W. Positive temperature correlations extend eastward along the equator past 120°W. Convergence in the wind field is evident along with the temperature signature, implying descent in the troposphere below. The patterns in several panels are suggestive of an out-of-phase relationship between the Maritime Continent and equatorial Africa and South America.

An analogous plot for GFS 150 hPa geopotential height is presented in Figure 5.2. This level is used because it corresponds to the peak wave amplitude in the geopotential height field (Dima and Wallace 2007). Geopotential height and TTL cirrus are significantly

positively correlated in the vicinity of each of the reference boxes, though the correlations are not as strong as for 100 hPa temperature. Physically, this indicates that TTL cirrus exist in a region of large-scale ascent above regions of upper-level high pressure. The geopotential height correlations exhibit some degree of equatorial symmetry, but this is less prominent than the temperature correlations in Figure 5.1. Similar wave-like features are observed around the reference box in panels C and D, with a ridge of high pressure extending along the equator to the east; to the west, regions of higher pressure are centered between 10° and 15° latitude. Secondary negative correlation centers can also be observed at this level, most prominently in panel B, where the negative correlations over eastern equatorial Africa exceed 0.4 in absolute value.

Figure 5.3 shows longitude-pressure cross sections of the temperature correlations. The GFS temperatures used to create these cross sections are meridional averages from 2.5°S to 2.5°N; the longitudinal resolution is 5°. The TTL cirrus index is calculated in the same manner as described earlier in this section. Reference boxes in this figure are the same as in the figures above and are indicated by black vertical lines.

A change in the sign of the temperature anomalies in the waves is evident near the 150 hPa level within and around the reference box in each panel of Figure 5.3. The strongest negative correlations are found at the 100 hPa level, while the strongest positive correlations lie between the 350 hPa and 200 hPa levels. The significant temperature anomalies associated with the TTL cirrus extend up to ~70 hPa. In Figure 5.3, anomalously cold temperatures at 70 hPa are located to the east of the cold anomalies at the 100 hPa level. In panels A through C, warm anomalies at 150 and 100 hPa also appear to the east of the corresponding anomalies between 300 and 200 hPa, indicating an eastward tilt with height above the level of waves' maximum amplitudes, similar to that identified in composites of the vertical structure of Kelvin

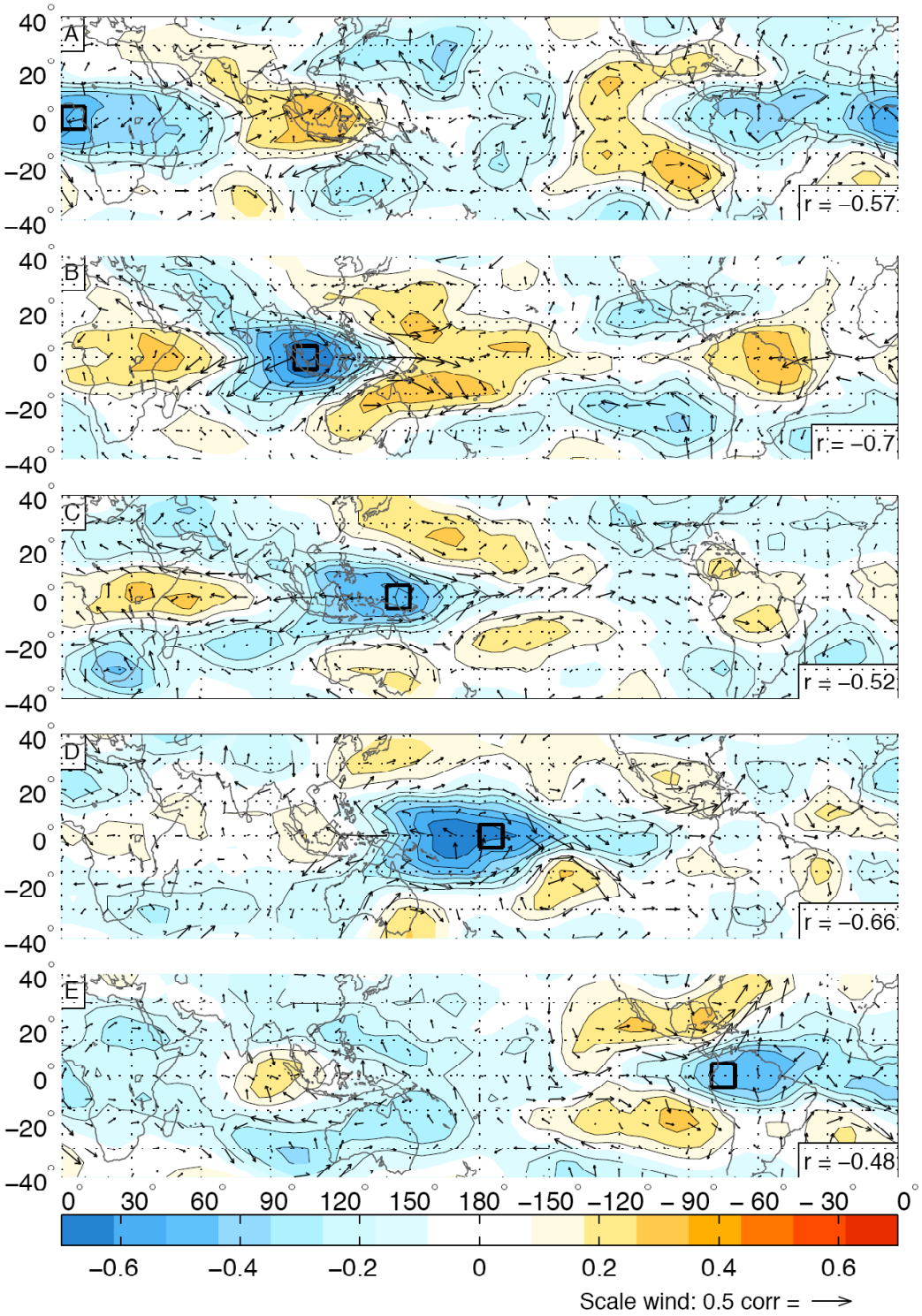

Figure 5.1 Latitude-longitude maps of correlations between CALIPSO 15 km base TTL cirrus index within black reference boxes and GFS 100 hPa temperatures (colors and contours) and winds (vectors) throughout tropics. Contour interval is 0.1. All variables have been filtered with 60-day high-pass Lanczos filter. Largest magnitude correlation in lower right.

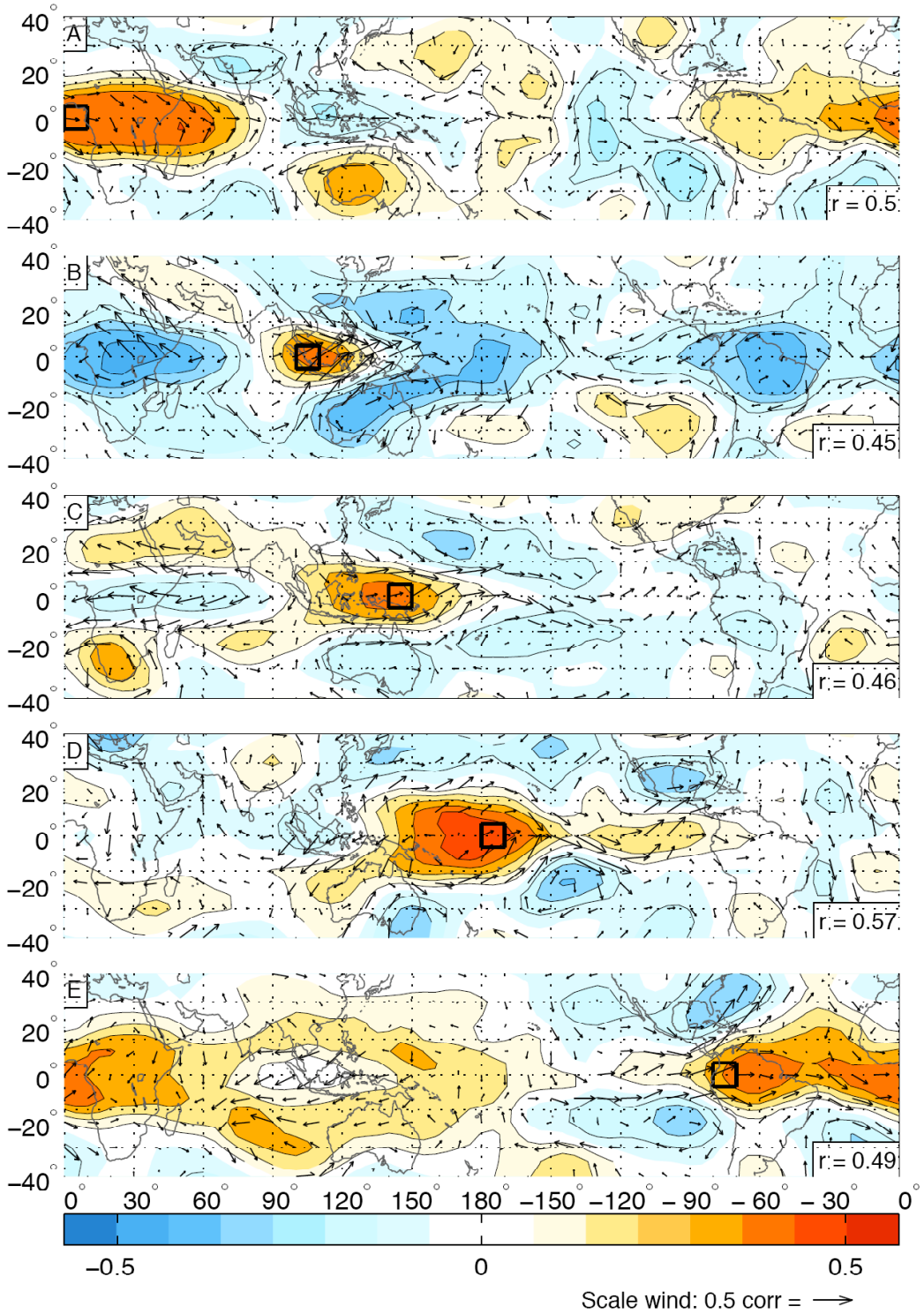

Figure 5.2 Latitude-longitude maps of correlations between CALIPSO 15 km base TTL cirrus index within black reference boxes and GFS 150 hPa geopotential heights (colors and contours) and winds (vectors) throughout tropics. Contour interval is 0.1. All variables filtered with 60-day high-pass Lanczos filter. Largest magnitude correlation in lower right.

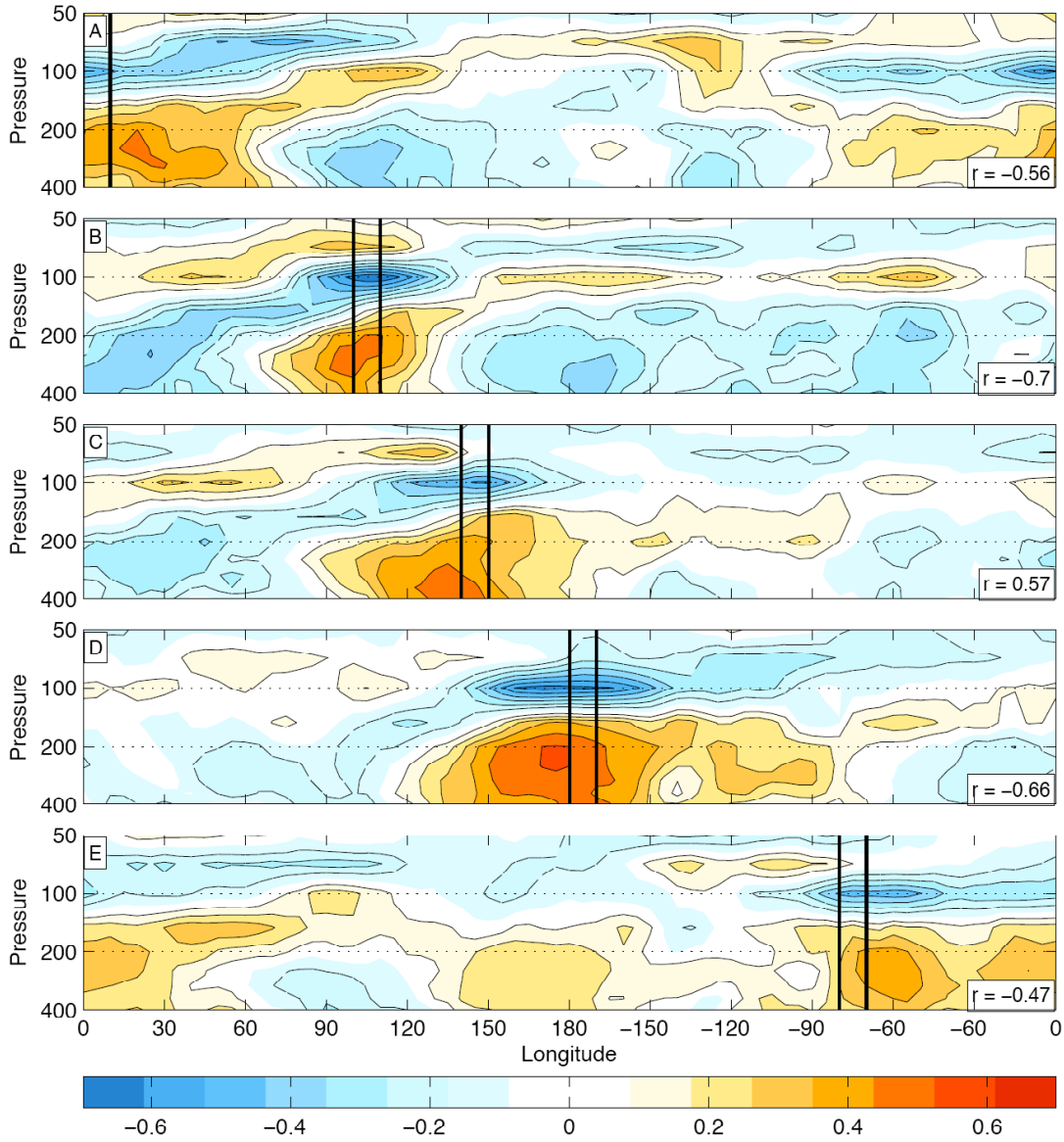

Figure 5.3 Longitude-pressure plots of correlations between CALIPSO 15 km base TTL cirrus index within 10° × 10° reference regions and GFS temperatures (colors and contours) from 2.5°S to 2.5°N. Contour interval is 0.1. All variables have been filtered with 60-day high-pass Lanczos filter. Largest magnitude correlation in lower right corner.

waves over the Indian Ocean in Roundy (2008) and in cross-sections of idealized equatorially-trapped Kelvin waves in Wallace and Kousky (1968) and Holton (1979). The cloud fields in Figure 3.11 exhibit a similar eastward tilt with height. The temperature fields in panels D and E of Figure 5.3 do not show such a pronounced eastward tilt.

Cold anomalies between the 400 and 200 hPa levels to the east (panel A), the west (panel C), and both sides (panel B) of the reference boxes, and the warm temperature anomalies above them at 100 hPa, mark the regions of subsidence in the wave-train (see discussion of Figure 5.1). Repeating the analysis of Figure 5.3 using geopotential height in place of temperature (not shown) confirms both a tilt with height (most evident in panels A, B, and E) and the correlation centers of opposing sign in panels A through C, consistent with an interpretation in terms of an anomalous wave-train.

One interesting aspect of Figure 5.3 is the difference in vertical structure between the African panel (A) and those from the Maritime Continent and western Pacific (B through D). In panel A, significant negative temperature correlations are observed at the 70 hPa level, covering the region from approximately 45°E to 100°E. In contrast, temperature correlations at 70 hPa in panels B through D are weak and insignificant. One might tend to think that this has some relation to the upper tropospheric anticyclone associated with the Indian monsoon; however, the temperature correlations at 70 hPa in this region (not shown) exhibit a high degree of equatorial symmetry, which makes this explanation unlikely. The significant cold anomalies at the 100 hPa level also span a larger portion of the equatorial region in panel A than in any of the other panels. Investigation into the reasons for these differences is beyond the scope of this paper.

Taking Figures 5.1, 5.2, and 5.3 together, then, we can conclude that TTL cirrus are significantly correlated with Gill (1980)-like planetary-wave perturbations within the TTL. The maximum amplitude of the perturbations in the Φ field occurs at the level of the sign reversal in the temperature correlations in Figure 5.3, just above the 150 hPa level.

SECTION 6: INTRASEASONAL VARIABILITY OF TTL CIRRUS

Having demonstrated that TTL cirrus are associated with planetary-scale waves, we now consider a possible source of these waves. We demonstrated in Section 5 that TTL cirrus is associated with planetary-scale waves over the Maritime Continent and western Pacific regions that bear certain similarities to modeled convectively-induced waves. As noted in the discussion of Figure 2.1, the filtered cold point temperature and cloud fraction time series at the Manus ARM site exhibit cyclic behavior with a period of ~40 days. The Madden-Julian Oscillation dominates variability in the 40–50 day range in the tropics and most strongly impacts the area from the Indian Ocean to the central Pacific (Zhang 2005). Thus, it seems reasonable to expect to observe some relationship between the convection associated with the MJO and TTL cirrus.

Convection associated with the MJO is known to have its genesis in the western and central Indian Ocean, to propagate eastward over the Maritime Continent, and to dissipate as it reaches the cooler waters of the central Pacific (Madden and Julian 1994; Zhang 2005). One means of quantifying the progression and strength of the MJO is the multivariate MJO index defined by Wheeler and Hendon (2004). This index is a time series with two components that are calculated by projecting daily observations, with the annual cycle and components of the interannual variability removed, onto two empirical orthogonal functions (EOFs) of a multivariate field comprised of near-equatorial OLR and lower- (850 hPa) and upper-tropospheric (200 hPa) zonal winds. The two components of the time-varying MJO index, RMM1 and RMM2, are orthogonal and can be used to define the phase space illustrated in Figure 6.1, which is a modified version of Figure 7 in Wheeler and Hendon (2004). The idealized evolution of the MJO, as represented on this chart, appears as a counterclockwise

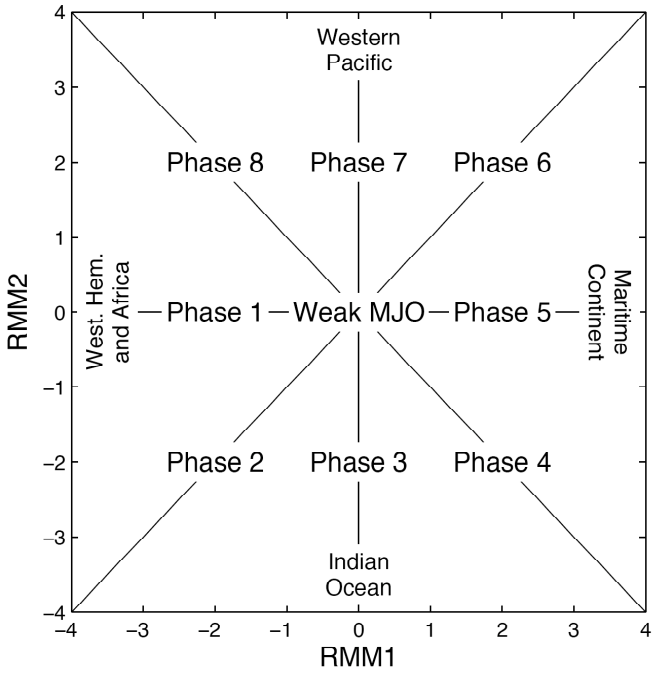

Figure 6.1 Phase space defined by two components of MJO index created by Wheeler and Hendon (2004), with eight directional phase vectors. Modified from Figure 7 of Wheeler and Hendon (2004), but retaining their indicated regions of maximum MJO-related convection.

rotation. The geographic regions of enhanced MJO-related convection as indicated in Wheeler and Hendon (2004) are retained for reference in Figure 6.1.

In order to relate observations of precipitation and TTL cirrus to the MJO, eight phases are defined as directional vectors in the RMM2 vs. RMM1 diagram and indicated in Figure 6.1. These are not precisely the same as the eight phases originally identified in Wheeler and Hendon (2004), which instead correspond to *sectors* of the diagram. We then use the daily values of RMM1 and RMM2 to create a set of eight different time series, each one representing the projection of the daily index onto a particular phase. Each of the MJO time series was adjusted to match the temporal resolution of the precipitation and TTL cirrus datasets and then renormalized.

We begin in Figure 6.2 by regressing filtered GPCP precipitation onto the time series for each phase of the MJO. Because of the way the phases have been defined, the regression

patterns for Phase 5 are of equal magnitude and opposite sign to those for Phase 1. For clarity, however, patterns for all eight phases are included in Figure 6.2.

Phase 1 marks the onset of an MJO episode, with convection forming over the central equatorial Indian Ocean. The remnants of the previous active phase are visible along the date line near 10°S. In Phase 2, these remnants have essentially dissipated, while convection in the Indian Ocean has intensified and shifted eastward. The region of enhanced convection continues its eastward propagation through Phase 4, weakening as it crosses the Maritime Continent (due to interaction with the local topography; Hsu and Lee 2005; Roundy 2008). In Phase 5, the convective center emerges into the western Pacific, reintensifies, and begins to split in two, with one focused on the ITCZ and the other on the SPCZ. By Phase 8, the northern feature has dissipated, while the southern one is still discernible near and to the east of the date line. Throughout the MJO cycle, only weak precipitation signals are present near the Americas, and no connection with the African continent is observed. The existence and northward migration of precipitation anomalies over India (Phases 2 through 5) and to the east of the Philippines (Phases 5 through 7) suggests that the MJO index is capable of resolving some of the intraseasonal variability related to the Indian monsoon (Knutson and Weickmann 1987; Wheeler and Hendon 2004).

Similarly constructed plots of the filtered TTL cirrus index (cloud fraction with base above 15 km) regressed onto the time series of each of the phases of the MJO are shown in Figure 6.3. In Phase 1, a weak maximum in the TTL cirrus field is observed over the equatorial Indian Ocean. From Phase 1 to Phase 5, this feature intensifies and propagates eastward over the Maritime Continent and into the western Pacific. Some reorganization in the cirrus field takes place around Phase 4 (not shown), seemingly related to the disruption in the convective anomaly. The cloud signal in the Pacific weakens during Phases 6 and 7 and no

longer appears in Phase 8. The TTL cirrus fields exhibit a higher degree of equatorial symmetry than the precipitation fields in Figure 6.2.

In Phases 3 through 6 of Figure 6.3, the convectively-induced wave signature, which we have documented in the one-point correlation plots above, is discernible to some degree, with maxima in the TTL cirrus field extending eastward along the equator from the location of maximum positive regression coefficient, and flanking the equator to the west of it. A Gill (1980)-like perturbation in the TTL in conjunction with the MJO has also been identified in past research (e.g., Hendon and Salby 1994, who focused on tropospheric-mean temperatures and 200 hPa wind fields, and Tian et al. 2006, who examined 100 hPa temperatures). The Rossby lobes, which are less conspicuous than the Kelvin feature in most of the phases in Figure 6.3, are more pominent in composites of total ozone column (Tian et al. 2007). Comparing Figures 6.2 and 6.3, it can be seen that the TTL cirrus signature is centered between 20° and 30° to the east of the primary convective center during Phases 2 through 7 (e.g., during Phase 3 the precipitation maximum is centered on 90°E, while the TTL cirrus signal is strongest near 120°E). A similar longitudinal displacement was observed by Eguchi and Shiotani (2004), who created composites of temperature and cirrus occurrence relative to the passage of five different MJO-related convective systems. They observed the lowest 100 hPa temperatures and the highest cirrus cloud fractions at that level between 15° and 25° to the east of the convective centers, implying an eastward tilt with height of the TTL disturbance. Consistent with this interpretation, Schwartz et al. (2008) found positive water vapor anomalies at the 100 hPa level to the east of the enhanced MJO-related convection. A similar displacement is evident in panels B and C of Figures 3.7 and 3.9, which indicate that convection near Indonesia and New Guinea is most strongly correlated with TTL cirrus between 20° and 30° to the east.

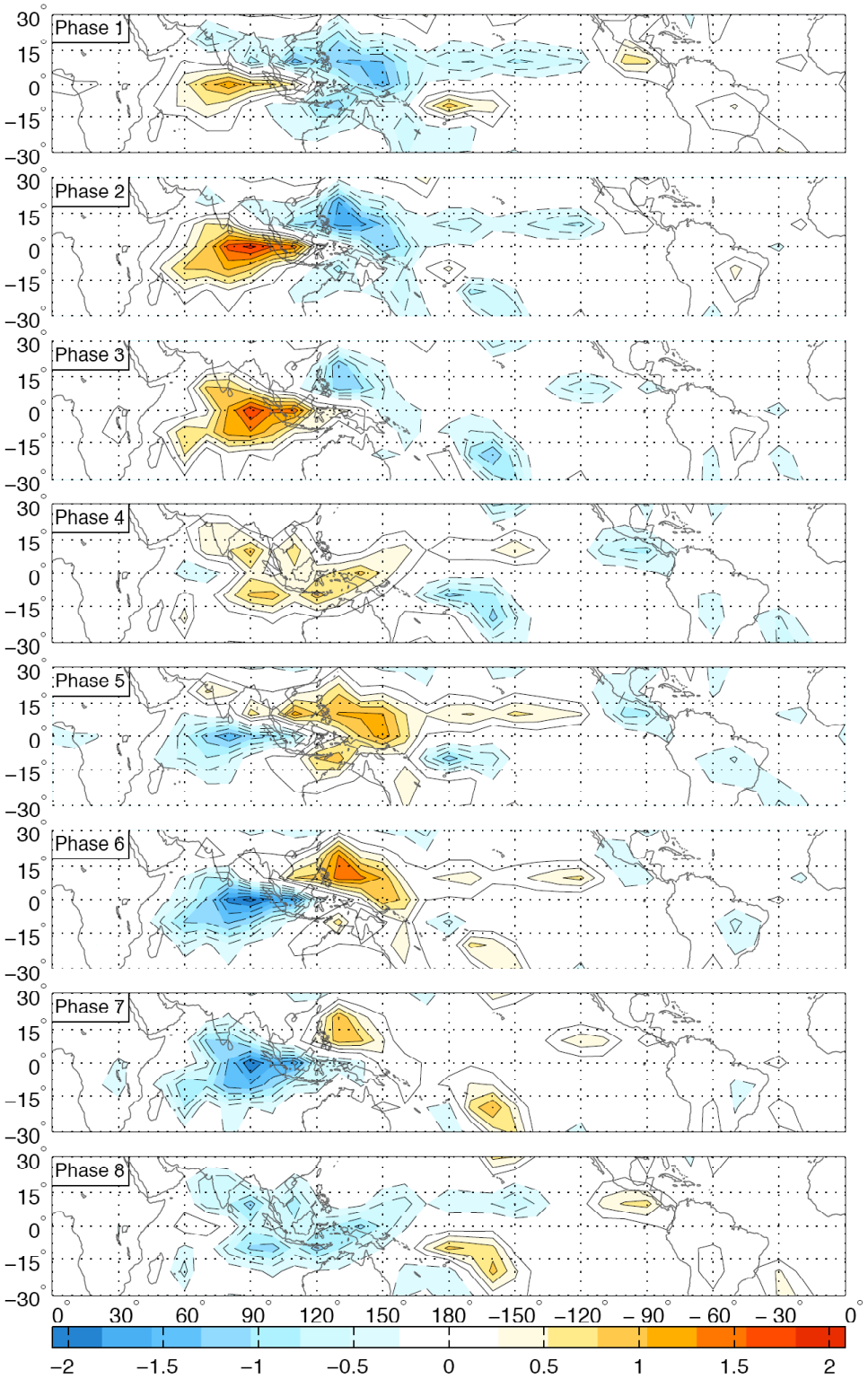

Figure 6.2 Latitude-longitude plots of GPCP precipitation (mm/day) throughout tropics regressed onto eight phases of MJO evolution. Contour interval is 0.25. Precipitation values have been filtered with 60-day high-pass Lanczos filter.

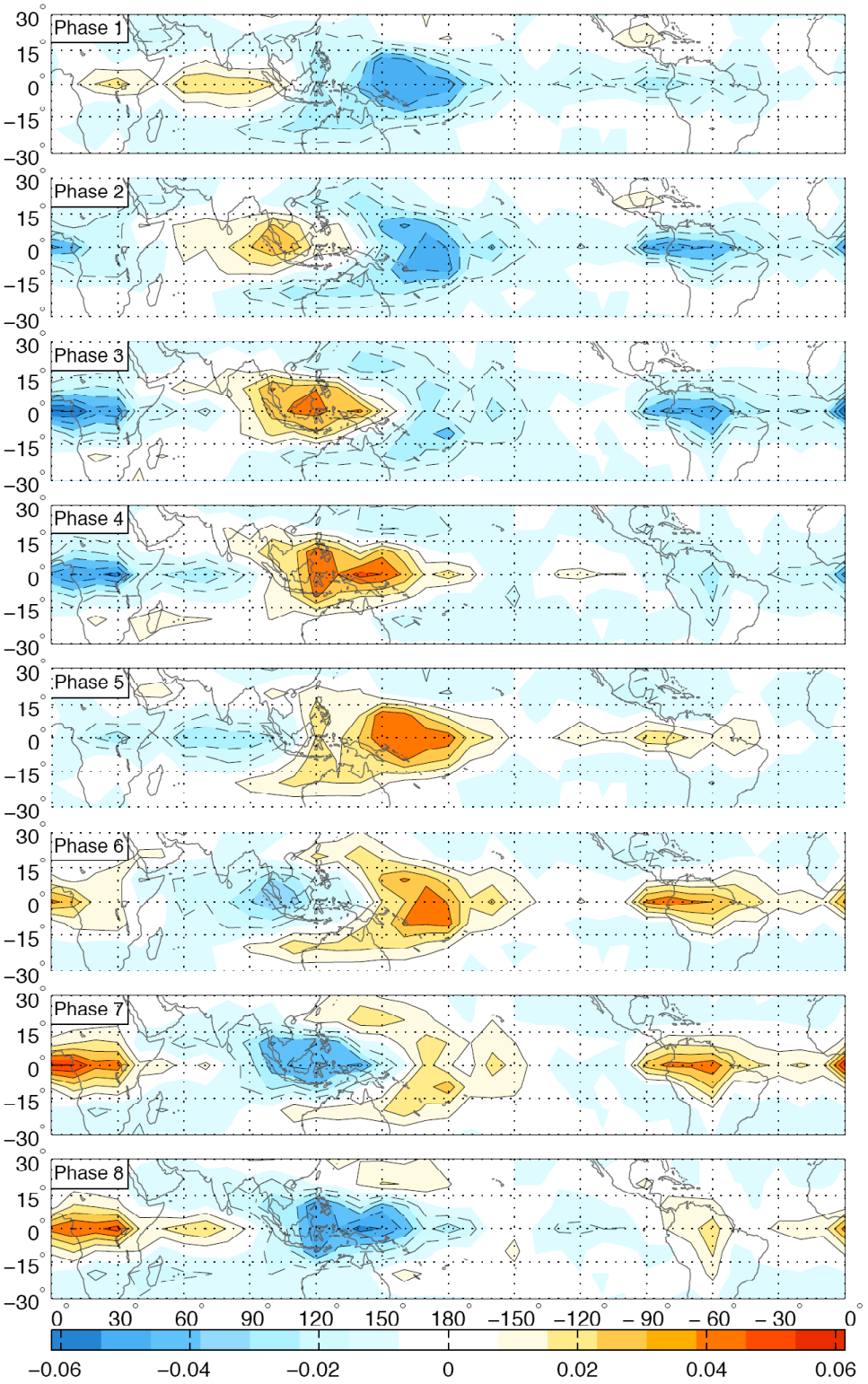

Figure 6.3 Latitude-longitude plots of CALIPSO 15 km base TTL cirrus index throughout tropics regressed onto eight phases of MJO evolution. Contour interval is 0.01. Cloud index has been filtered with 60-day high-pass Lanczos filter.

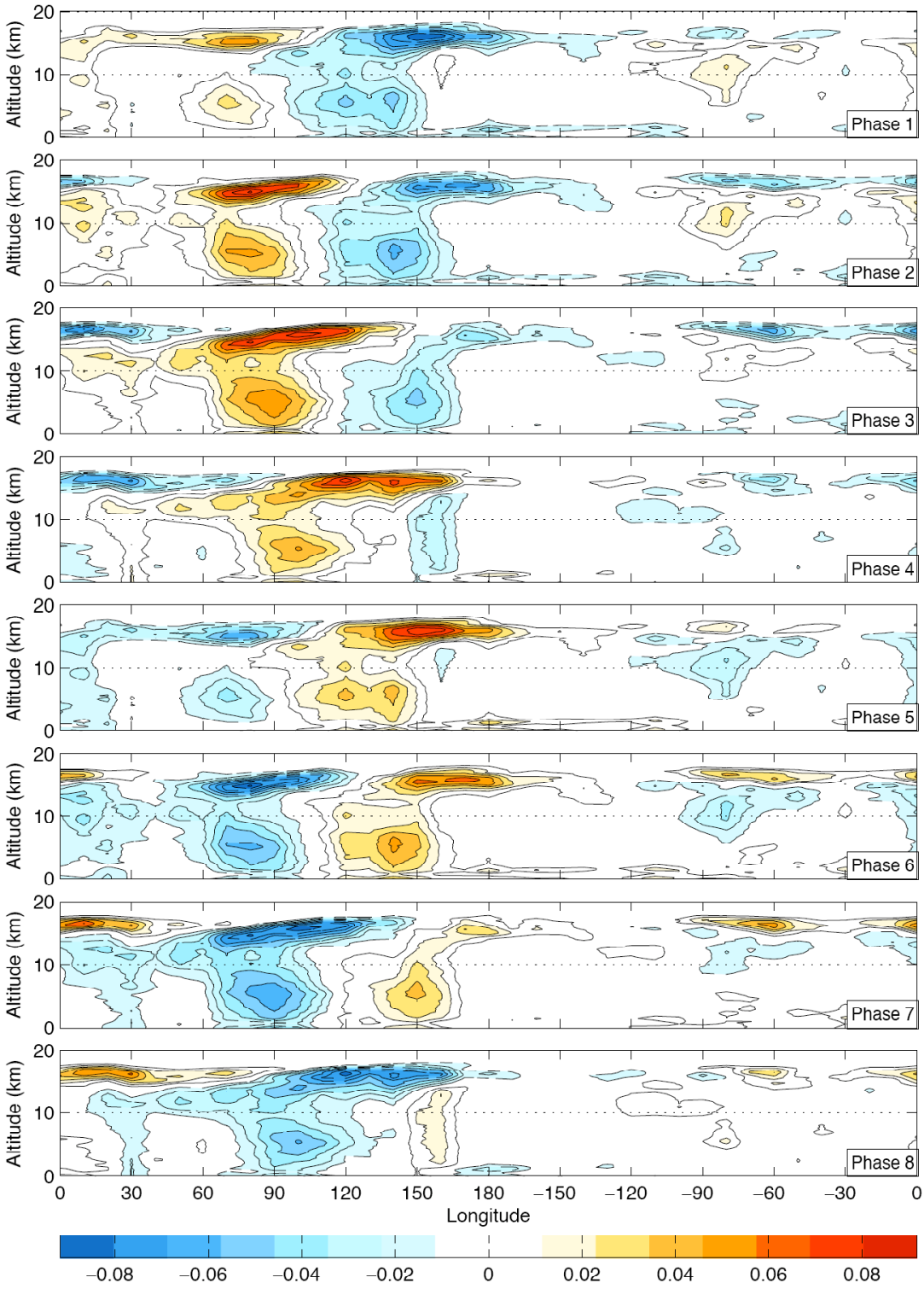

Figure 6.4 Longitude-height plots of CALIPSO height dependent tropical cloud index from 5°S to 5°N regressed onto eight phases of MJO evolution. Longitudinal resolution is 10°. Contour interval is 0.01. Cloud index has been filtered with 60-day high-pass Lanczos filter.

Another interesting feature of Figure 6.3 is the existence of TTL cirrus maxima over both equatorial South America and Africa during the latter stages of the MJO cycle. The cirrus signal over South America during Phases 6 and 7 and over Africa during Phases 7 and 8 is nearly as strong as the signal over the warm pool region during Phases 3 through 6, although cirrus signals over Africa and South America are more narrowly confined to the equatorial belt. These results are in agreement with previous studies of Knutson and Weickmann (1987), Hendon and Salby (1994), and Bantzer and Wallace (1996), which indicated that the upper-level perturbation associated with the MJO circumnavigates the equatorial belt.

The vertical structure of the cloud field associated with the MJO can be seen more clearly in Figure 6.4, in which the equatorial height-dependent cloud index (cloud fraction within successive 200 m layers, as defined in Section 3) is regressed onto the time series for the respective MJO phases. In Phase 1, a cirrus signal is evident between 60°E and 90°E, and a weak convective signal in the lower troposphere is visible beneath it. Both cloud features intensify and propagate eastward into the western Pacific, although, as mentioned above, the convective signature weakens as it crosses the Maritime Continent while the associated cirrus signature undergoes some reorganization. The convective signal becomes less prominent in the latter half of the MJO's evolution as the convective center shifts off the equator (see Figure 6.2) and decays.

As noted previously, the cirrus feature in Phase 1 is centered almost directly above the convection. As the MJO evolves, the cirrus feature propagates eastward more rapidly than the convection, eventually leading it by more than 30° longitude. This observation is in agreement with previous work which has suggested eastward propagation speeds of $3-6$ m s^{-1} for MJO-related convection and 10 m s^{-1} for the large-scale circulation features within which the TTL cirrus are embedded (Knutson and Weickmann 1987). An eastward tilt with increasing altitude

is also evident in the cirrus signatures, particularly in Phases 2 through 4; a similar eastward tilt with height was found in equatorial cross-sections of Microwave Limb Sounder (MLS)-acquired TTL water vapor anomalies composited relative to the progression of the MJO (Schwartz et al. 2008). As noted in Section 5, this eastward tilt with height is characteristic of the structure of an equatorial Kelvin wave in a stably stratified atmosphere (Wallace and Kousky 1968; Holton 1979; Roundy 2008).

A cirrus signal above South America (Phases 6 and 7) and Africa (strongest during Phases 7 and 8) is also apparent in the vertical regressions in Figure 6.4. This feature is smaller in both horizontal and vertical extent than the cirrus signal above the warm pool and displays no noticeable tilt with height. It is also higher in altitude, confined almost completely above the 15 km level, in contrast to the cirrus signature over the Maritime Continent, which extends as low as 13 km. From an inspection of the patterns for Phases 8 and 1, it is evident that the TTL cirrus maximum is already in place above Africa and the equatorial Indian Ocean as the convective anomaly begins to develop; whether the circulation feature associated with the TTL cirrus plays any role in initiating the convection of the subsequent MJO episode cannot be determined from our analyses.

The regression plots presented in this section have demonstrated the existence of a TTL cirrus signature in conjunction with the MJO and have revealed some of its characteristics. We would now like to determine to what extent the unfiltered cloud fraction varies during an MJO evolution. To explore this using a compositing analysis, we first return to the phase space defined by the two MJO indices of Wheeler and Hendon (2004). Figure 6.5 is a repetition of Figure 6.1, but in this case we define eight sectors in the MJO index plane; these sectors correspond to the eight phases originally defined by Wheeler and Hendon (2004). Each day of our observation period falls into one of these eight sectors.

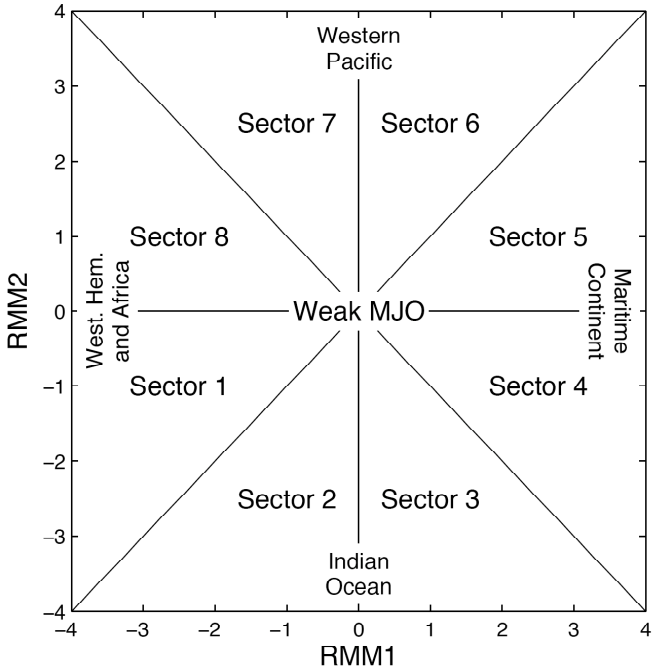

Figure 6.5 Phase space defined by two components of MJO index created by Wheeler and Hendon (2004), with eight MJO sectors. Modified from Figure 7 of Wheeler and Hendon (2004), but retaining their indicated regions of maximum MJO-related convection.

We begin by compositing unfiltered GFS 100 hPa temperatures and winds according to MJO sector. For this analysis, we include only those days when the magnitude of the MJO vector is greater than one standard deviation from zero, so that the 120 days on which the MJO signal was weakest, or 16% of the total data period, are discarded. The composite 100 hPa temperature and wind fields for each sector are plotted in Figure 6.6. In Sector 1, a weak temperature signature is observed above the eastern Indian Ocean and Maritime Continent. This feature intensifies and propagates eastward as the MJO cycle progresses and eventually weakens in Sectors 7 and 8.

Over the Maritime Continent and western Pacific, temperatures near 193 K and 194 K are observed in Sectors 1 and 8 of Figure 6.6, during the MJO's initial and dissipating stages. Temperatures between 191 K and 192 K are observed above this region when the MJO signature is directly overhead. Lower temperatures are also observed above equatorial South

America in Sectors 4 through 7 and above equatorial Africa in Sectors 6 through 8; 100 hPa temperatures above these locations vary as much as 3 K during the MJO cycle. The temperature and wind fields in Sectors 2 through 7 resemble the planetary wave signature of Gill (1980), which we have previously observed in the TTL cirrus regression plots. The Rossby lobes are more defined in these composite maps than in any of our previous plots and in some sectors extend westward over 90° of longitude from the location of minimum temperature.

We now repeat this compositing analysis for TTL cirrus. Figure 6.7 shows composite cloud fractions (with base above 15 km, in line with our TTL cirrus index) for each MJO sector. Modulation of TTL cirrus by the MJO is evident in these plots. Cloud fractions above the warm pool region vary from $\sim 0.15-0.2$ when the MJO is in its initial and dissipating stages to $\sim 0.3-0.35$ during Sectors 3 through 6. Larger variations in cloud fraction take place above equatorial Africa and South America, where TTL cirrus are almost non-existent in Sector 2 and are observed between 35% and 40% of the time during the later stages of the MJO. The physical meaning of the negative cloud signatures in Figure 6.3 becomes clearer upon examination of Figure 6.7. During Phases 7 and 8 of Figure 6.3, for example, negative regression coefficients are observed above the Maritime Continent. In Sector 7 in Figure 6.7, cloud fractions above this region are in the range of $0.15-0.2$. The climatological mean cloud fraction for this region is in the range of $0.2-0.25$ (see Figure 1.1), indicating suppression of TTL cirrus during this portion of the MJO cycle.

Thus far, we have focused on specific circulation and cirrus features associated with the MJO. The notion that the fields of certain variables averaged over the tropics as a whole pulsate in association with the MJO cycle has been suggested in previous studies (e.g., Hendon 1995). Considering tropical fields which included the zonal mean, Bantzer and Wallace (1996)

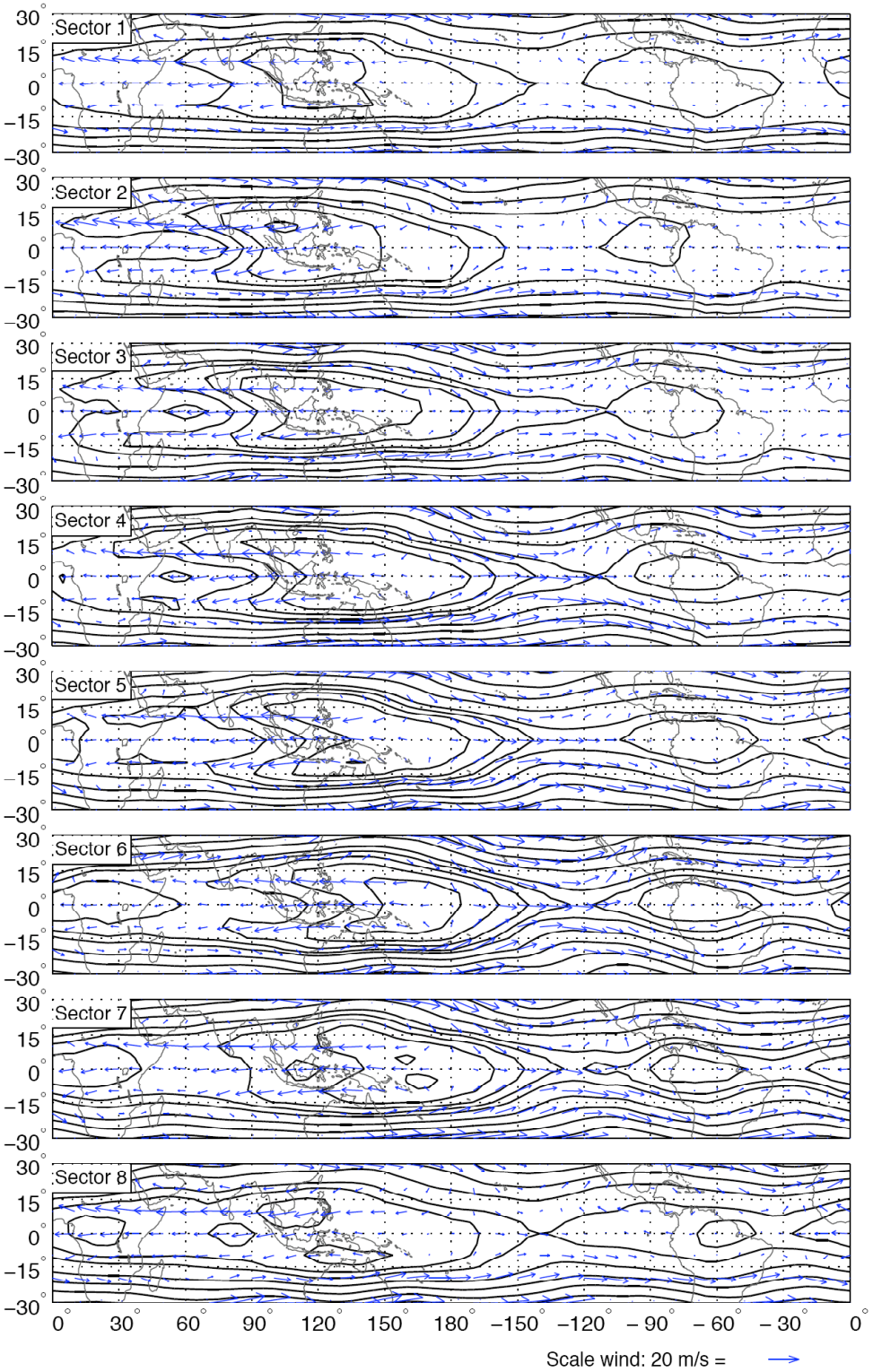

Figure 6.6 Latitude/longitude composites of unfiltered GFS 100 hPa temperature (contours) and winds (vectors) in eight MJO sectors, limited to days with magnitude of MJO vector greater than one standard deviation from zero. Contours at …194, 195, 197.5, 200, … Kelvin.

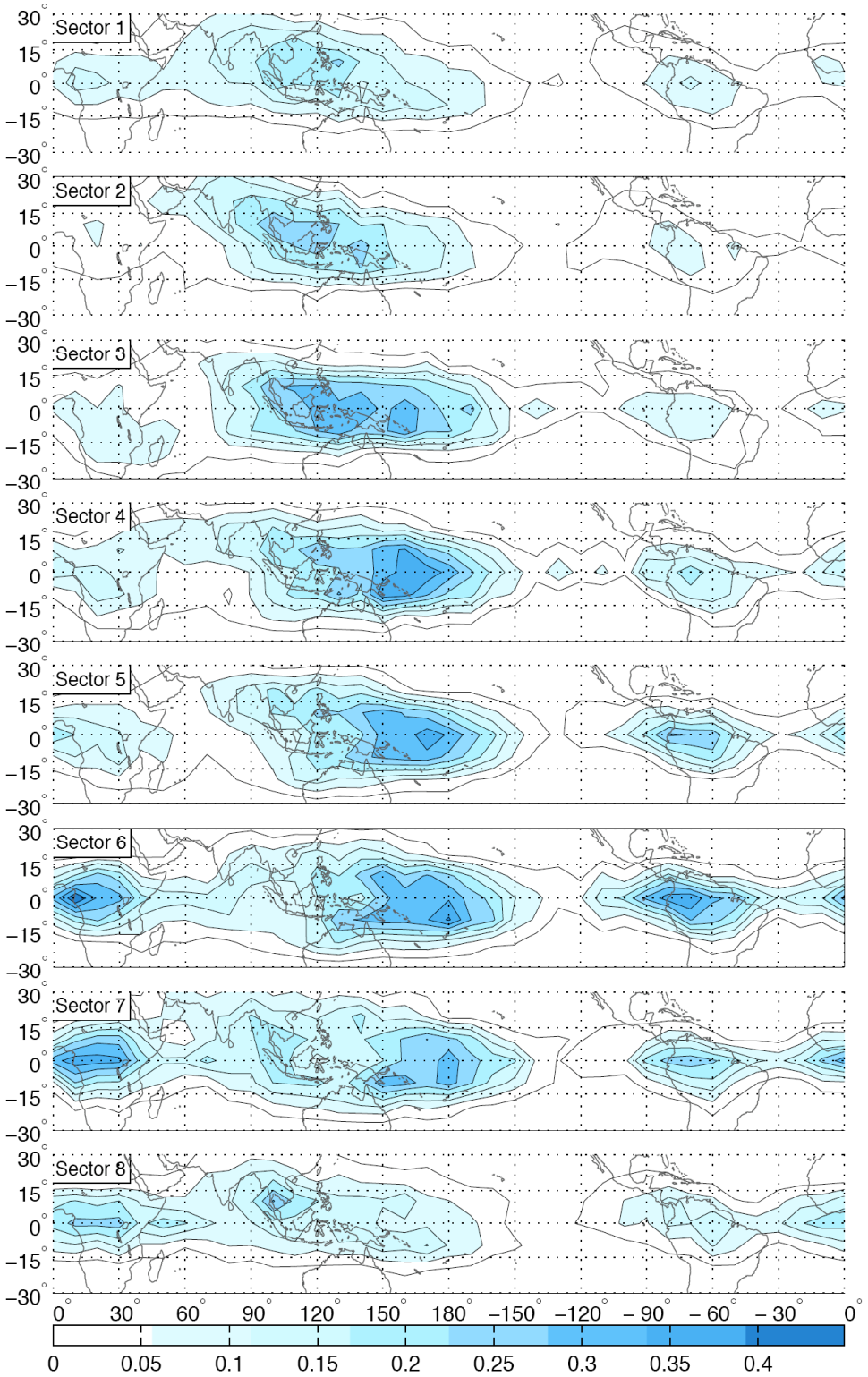

Figure 6.7 Latitude/longitude composites of unfiltered CALIPSO 15 km base TTL cirrus index (colors and contours) in eight MJO sectors, limited to days with magnitude of MJO vector greater than one standard deviation from zero. Contour interval is 0.05.

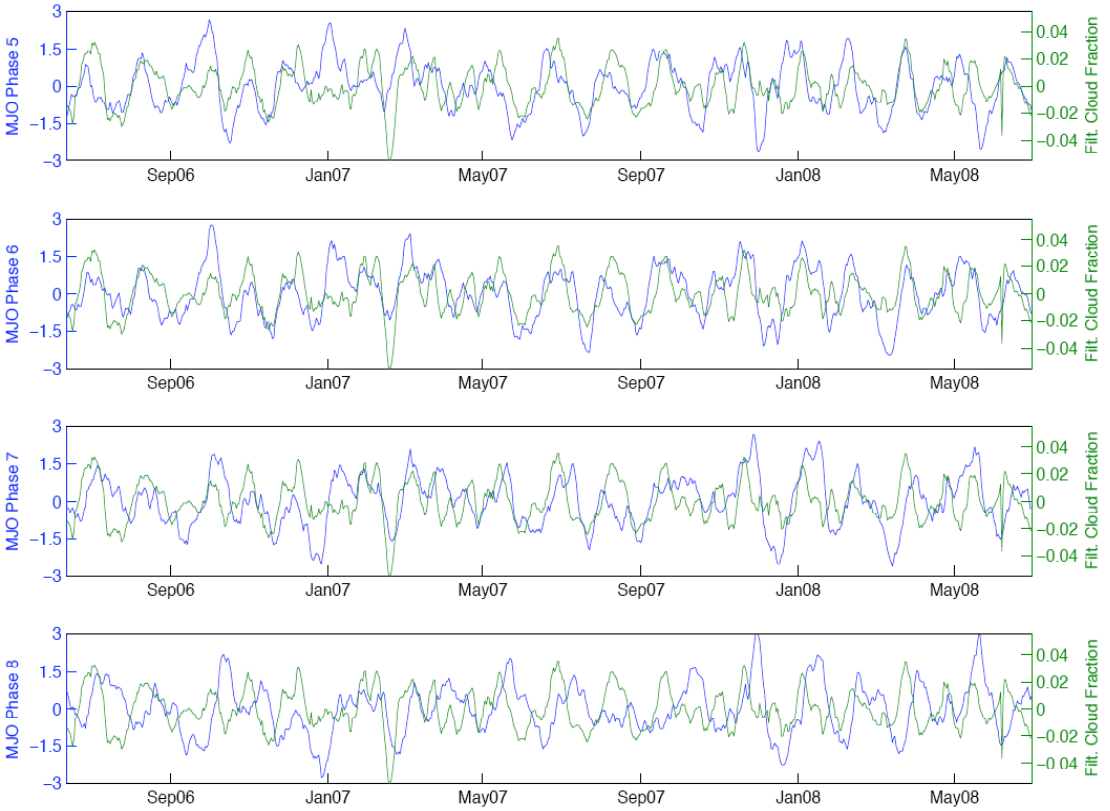

Figure 6.8 Time series of Phases 5 through 8 of the MJO index from June 2006–June 2008, plotted along with seven-day running mean cloud fraction equatorward of 20° latitude with base above 15 km, derived from CALIPSO profiles. Cloud fraction has been filtered using 60-day high-pass Lanczos filter.

observed an upper-tropospheric temperature signal propagating quickly (at ~40 m/s) eastward from the convective region of the MJO following the time of maximum tropical mean precipitation, resulting in a ~0.15 K increase in the tropical mean temperature during the MJO's later stages.

In order to investigate this possibility, we make use of the seven-day running mean tropical mean TTL cirrus fraction (defined as the fraction of CALIPSO profiles gathered equatorward of 20° latitude in which a cloud with base above 15 km was identified), which was first plotted in Figure 2.2. The tropical mean TTL cirrus fraction, after being filtered using the 60-day high-pass Lanczos filter, is plotted with the time series of MJO Phases 5 through 8 in Figure 6.7. Periodic behavior is evident in the cloud fraction time series, and visual

inspection reveals similarities in the timing of the peaks and valleys of this and the MJO time series during some phases, particularly during Phase 6.

That the MJO modulates tropical mean 100 hPa temperature and TTL cirrus is also apparent from a close examination of Figures 6.6 and 6.7. The coldest, cloudiest conditions occur in Sector 6, when MJO-related activity is observed above the western Pacific and equatorial Africa and South America, while the warmest, clearest conditions occur in Sector 2. The tropical mean temperature difference (equatorward of 10° latitude) between these two sectors is ~1.8 K, and tropical mean TTL cirrus fraction ranges over nearly a factor of 2, from 0.110 in Sector 2 to 0.212 in Sector 6.

SECTION 7: ANNUAL AND INTERANNUAL VARIABILITY OF TTL CIRRUS

As noted in Section 2, TTL cirrus also varies on annual and interannual time scales. With just two years of data, definitive analysis of these phenomena is not yet possible; however, the basic characteristics of this variability will be documented in this section based on the data available to date.

The annual cycle in GPCP precipitation and GFS 150 hPa geopotential height during the two-year CALIPSO period of record is illustrated in Figure 7.1, in which mean values from June–August and December–February are shown along with the difference between them. The precipitation field during JJA is dominated by the Indian and Southeast Asian monsoon and by the Pacific and Atlantic ITCZs. The upper tropospheric high associated with the Indian monsoon is visible in the geopotential height field. During DJF, there is a stationary, planetary-wave signature above the warm pool, and precipitation is heaviest over the SPCZ, the Indian Ocean ITCZ, and tropical South America. The difference plot in the bottom panel emphasizes the contrast between the winter and summer hemispheres, with the summer hemisphere typically experiencing greater tropical rainfall and higher geopotential heights than the winter hemisphere.

Analogous plots for the TTL cirrus index, a measure of the areal coverage of clouds with bases above 15 km, are shown in Figure 7.2. The JJA and DJF panels were previously shown in Figure 1.1 and, as mentioned in the discussion of that figure, TTL cirrus during JJA are most frequently observed above southern Asia, in association with the monsoon. During DJF, TTL cirrus maxima are centered on or just south of the equator. Massie et al. (2002) observed similar patterns in boreal winter and summer tropical cirrus identified during the Halogen Occultation Experiment (HALOE). The difference plot in the bottom panel of Figure

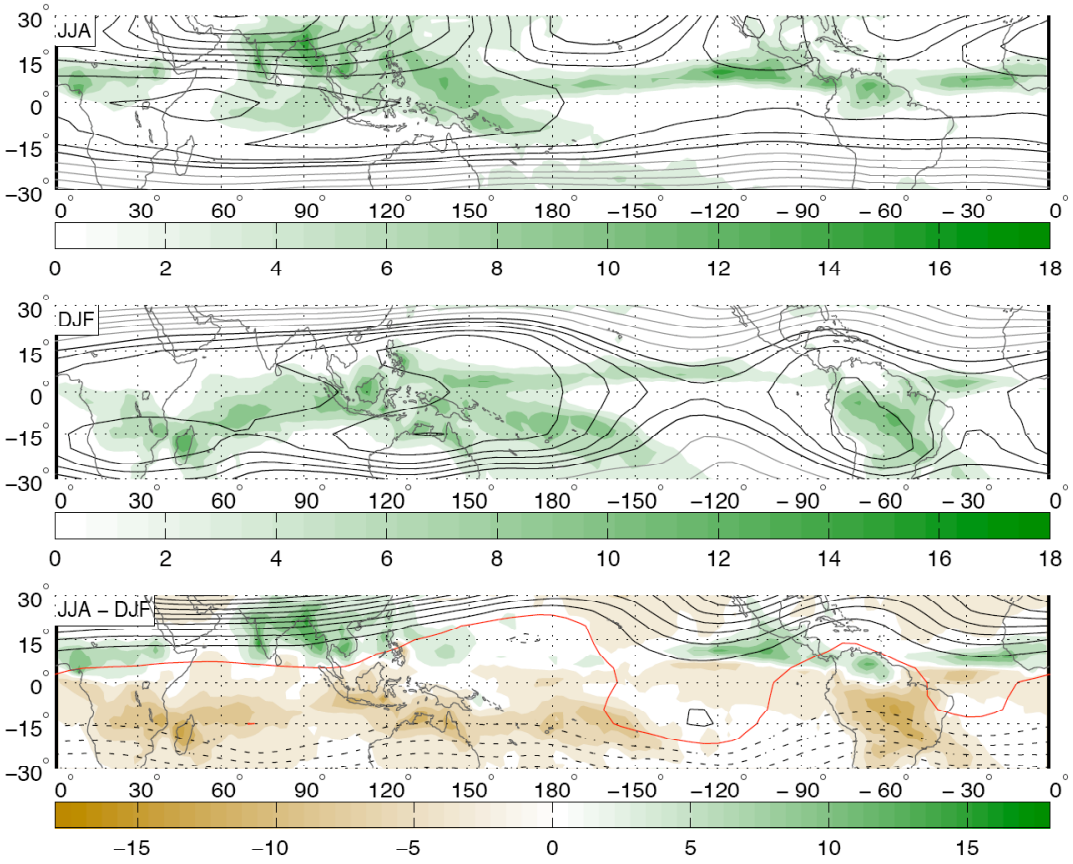

Figure 7.1 Mean atmospheric conditions during June–August (panel A) and December–February (panel B), as well as the difference between them (panel C). GPCP precipitation (mm/day) in colors, with contour interval 3 mm/day. GFS 150 hPa geopotential height is contoured, with contours at …14050, 14100, 14150, 14175, 14200, … meters (panels A and B) and every 50 m (panel C). All variables are unfiltered.

7.2 indicates that the Southern Hemisphere and equatorial belt both tend to be cloudier during DJF; some locations experience variations in cloud fraction as large as 0.3 in association with the annual cycle. Inspection of Figure 7.2 also reveals that the boreal winter months tend to be cloudier over the tropics as a whole; this observation is consistent with the findings of Zhang (1993). Tropical mean TTL cirrus fraction equatorward of 10° latitude varies from 0.091 during JJA to 0.223 during DJF, an increase of almost 145% during the boreal winter. In the mean over the entire tropics equatorward of 30° latitude, DJF TTL cirrus fraction is ~63% larger than JJA cloud fraction.

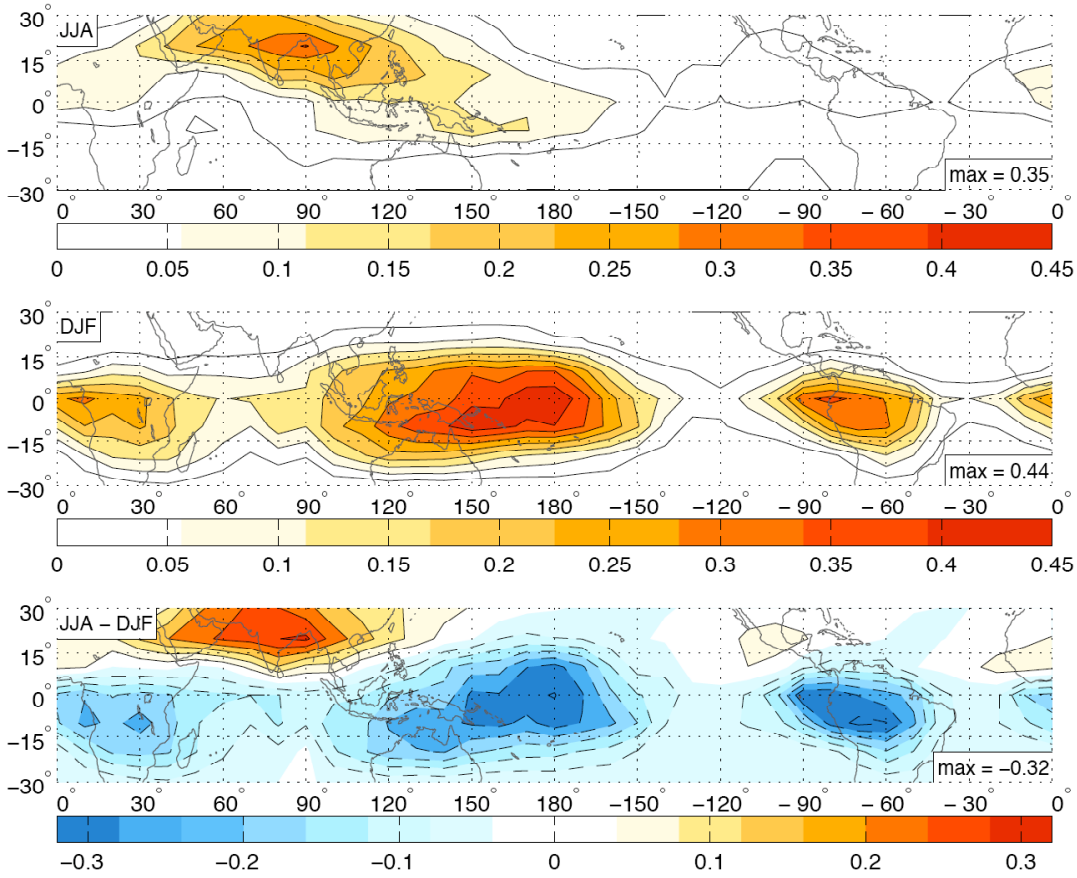

Figure 7.2 Mean TTL cirrus fraction (with base above 15 km) during June–August (panel A) and December – February (panel B), as well as the difference between them (panel C). Contour interval is 0.05. Cloud fraction is unfiltered.

The tropical lower stratosphere experiences a strong annual cycle with $\geq 5°$C in peak-to-peak amplitude, with the lowest temperatures in both hemispheres observed during the boreal winter months and a high level of even symmetry about the equator (Reed and Vlcek 1969). The tropical troposphere, on the other hand, witnesses a seasonal shifting of the rising branch of the Hadley circulation back and forth across the equator so as to remain in the summer hemisphere (Hartmann 1994); i.e., it exhibits odd symmetry about the equator. The TTL, which serves as a transition zone between troposphere and stratosphere, exhibits elements of both even and odd symmetry, as evidenced by the JJA–DJF difference plot shown in the

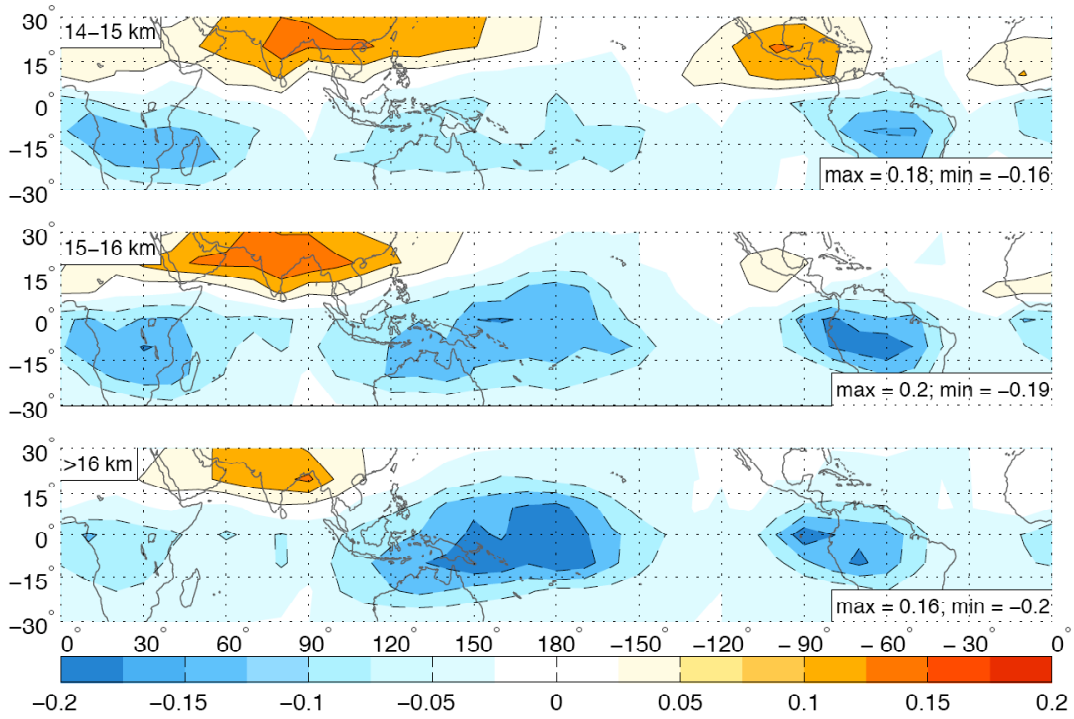

Figure 7.3 Difference between mean cloud fraction during June – August and December – February (negative values indicate cloudier DJF). Cloud fractions calculated for clouds with base between 14 and 15 km (top panel), between 15 and 16 km (middle), and above 16 km (bottom). Contour interval is 0.05. Cloud fraction is unfiltered.

bottom panel of Figure 7.2. We can investigate the transition in further detail by isolating cirrus within several altitude ranges.

Figure 7.3 shows the JJA–DJF difference plots for cirrus with bases in the altitude ranges indicated in the upper left corner of each panel. For cirrus with bases between 14 and 15 km, more cirrus are observed in the summer hemisphere. In the 15–16 km layer, portions of the northern tropics experience greater cloud cover during the boreal winter than during the boreal summer. Above the 16 km level, more cirrus is observed during the boreal winter than the boreal summer throughout the tropics except over southern Asia, where cloudiness associated with the Indian monsoon is still the stronger influence. Hence, the transition of the structure of the annual cycle from tropospheric with odd equatorial symmetry reflecting the meridional shifting of the Hadley cell, to stratospheric with even equatorial symmetry

reflecting the strengthening and weakening of the Brewer-Dobson circulation takes place mainly within the 15–16 km layer.

A major component of tropical interannual variability is El Niño/Southern Oscillation (ENSO). Dima (2005) generated composites of tropical geopotential height and winds for both the ten strongest El Niño and La Niña months during the period 1979–2001 and found that the equatorial planetary wave signature at the 150 hPa level above the warm pool is very pronounced during the strongest La Niña episodes and only barely discernible during the strongest El Niño episodes. Yulaeva and Wallace (1994) found that MSU channel-4 (lower stratospheric) temperatures also tended to be lower during La Niña years. Other studies have found that convective activity related to the Madden-Julian Oscillation extends farther into the Pacific during El Niño, feeding off the anomalously warm surface waters (Eguchi and Shiotani 2004), and that cirrus within the TTL experiences a similar eastward shift during El Niño (Gettelman et al. 2001).

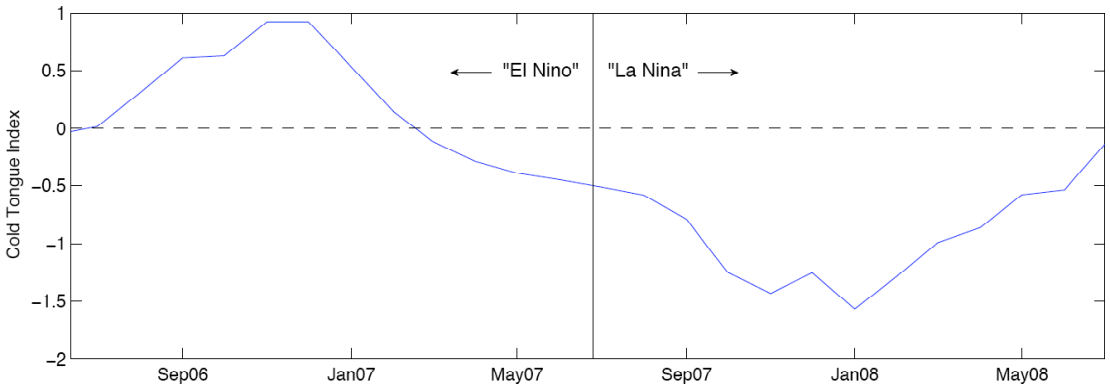

Figure 7.4 Monthly values of cold tongue index (CTI) during the period June 2006–June 2008. CTI calculated by averaging sea surface temperature (SST) anomalies within the region 6°S–6°N, 180°–90°W and subtracting from this the global mean SST. Anomalies calculated relative to the period 1845–2008. Designations of "El Niño" and "La Niña" years indicated.

A convenient measure of the ENSO phase is the so-called "cold tongue index" (CTI), the departure of the sea surface temperature (SST) anomalies averaged over the region 6°S–6°N, 180°–90°W from the global-mean SST (Deser and Wallace 1990). CTI values during the

period June 2006–June 2008 are plotted in Figure 7.4 (SST anomalies have been calculated relative to the period 1845–2008). The CTI is weakly positive during the latter part of 2006 and early 2007. In March 2007, the CTI becomes negative, and pronounced La Niña conditions prevail through the remainder of the observation period. In light of this behavior, we can gain a simplified view of the impact of ENSO by comparing the first and second halves of the data period, as indicated by the vertical dividing line in Figure 7.4.

We begin by comparing the mean atmospheric fields during the El Niño and La Niña years. Figure 7.5 contrasts mean GPCP precipitation rates and GFS 150 hPa geopotential heights for the two years, and difference fields are plotted in the bottom panel. During the El Niño year, precipitation rates were higher over the western Pacific and along the ITCZ, and lower over the Maritime Continent and SPCZ, than during the La Niña year, in agreement with composites based on longer periods of record (Ropelewski and Halpert 1987). The convectively-induced planetary wave signature over the eastern hemisphere is more pronounced during the La Niña year (Dima 2005; Eguchi and Shiotani 2004), although geopotential heights throughout the tropics were on average higher by nearly 20 m during the El Niño year (a similar result was noted during the boreal winter months by Horel and Wallace [1981]). The difference plot reveals lobes of anomalously high heights flanking the equator near 150°W during the El Niño year; similar anticyclonic features were noted by Horel and Wallace (1981), Yulaeva and Wallace (1994), and Gettelman et al. (2001).

Mean TTL cirrus cloud fractions during the El Niño and La Niña years are contrasted in Figure 7.6, and the diffrence field is shown in the bottom panel. Cloud fractions for the tropics as a whole are slightly larger during La Niña than El Niño — tropical mean cloud fraction equatorward of 10° was 0.1471 during the El Niño year versus 0.1702 during the La Niña year, meaning that the La Niña year was 15.6% cloudier in the TTL than the El Niño

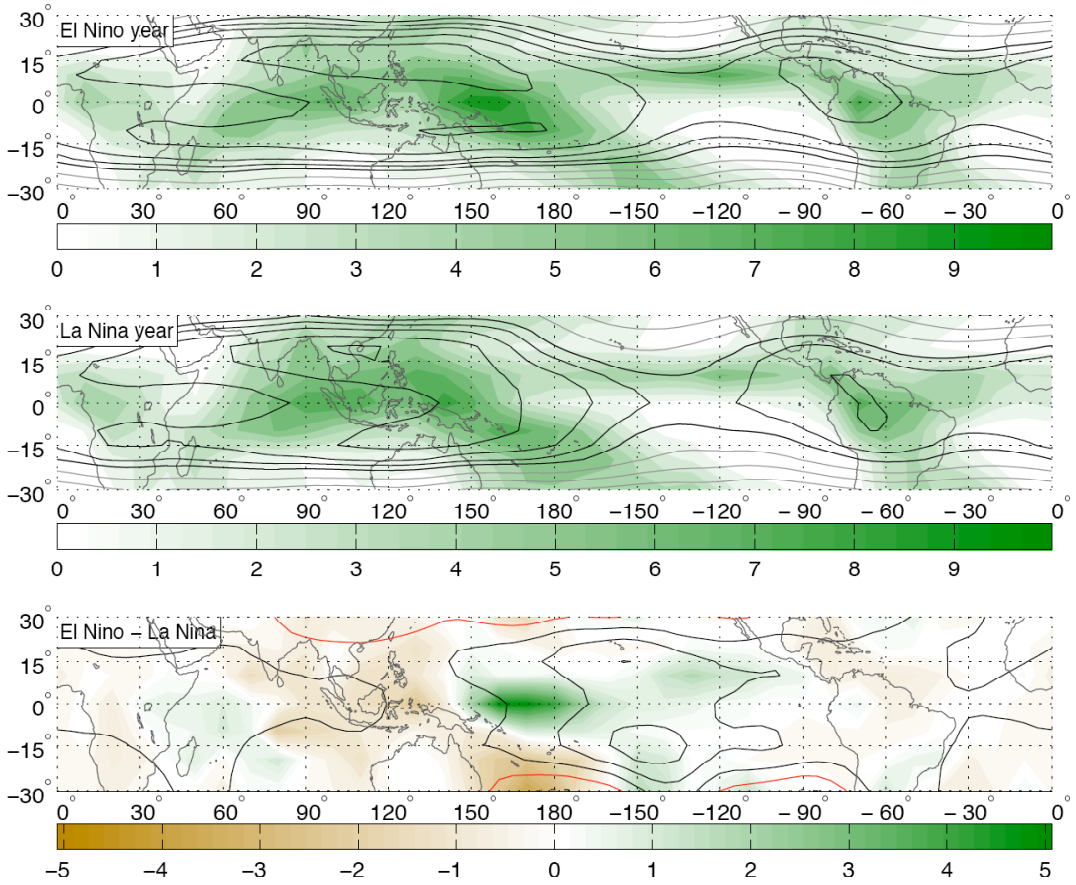

Figure 7.5 Mean atmospheric conditions during "El Niño" (June 2006–June 2007; panel A) and "La Niña" (June 2007–June 2008; panel B) years, as well as the difference between them (panel C). GPCP precipitation (mm/day) in colors, with contour intervals 1 mm/day (panels A and B) and 0.25 mm/day (panel C). GFS 150 hPa geopotential height is contoured, with contours at …14050, 14100, 14150, 14175, 14200, … meters (panels A and B) and every 20 m (panel C). All variables are unfiltered.

year. These year-to-year differences are also evident in the time series of TTL cloudiness in Figure 2.2. Given the weakness of the El Niño during June 2006–June 2007, the real magnitude of the fluctuations in cloud cover associated with the ENSO cycle may well be somewhat larger than the values given above.

During the El Niño year, TTL cirrus occurrence was highest over the western to central Pacific; this maximum shifted westward and strengthened during the La Niña year. As a result, more TTL cirrus were observed over the central Pacific, between 180° and 130°W, during the El Niño year, while cloud fractions over the Maritime Continent and western Pacific were as

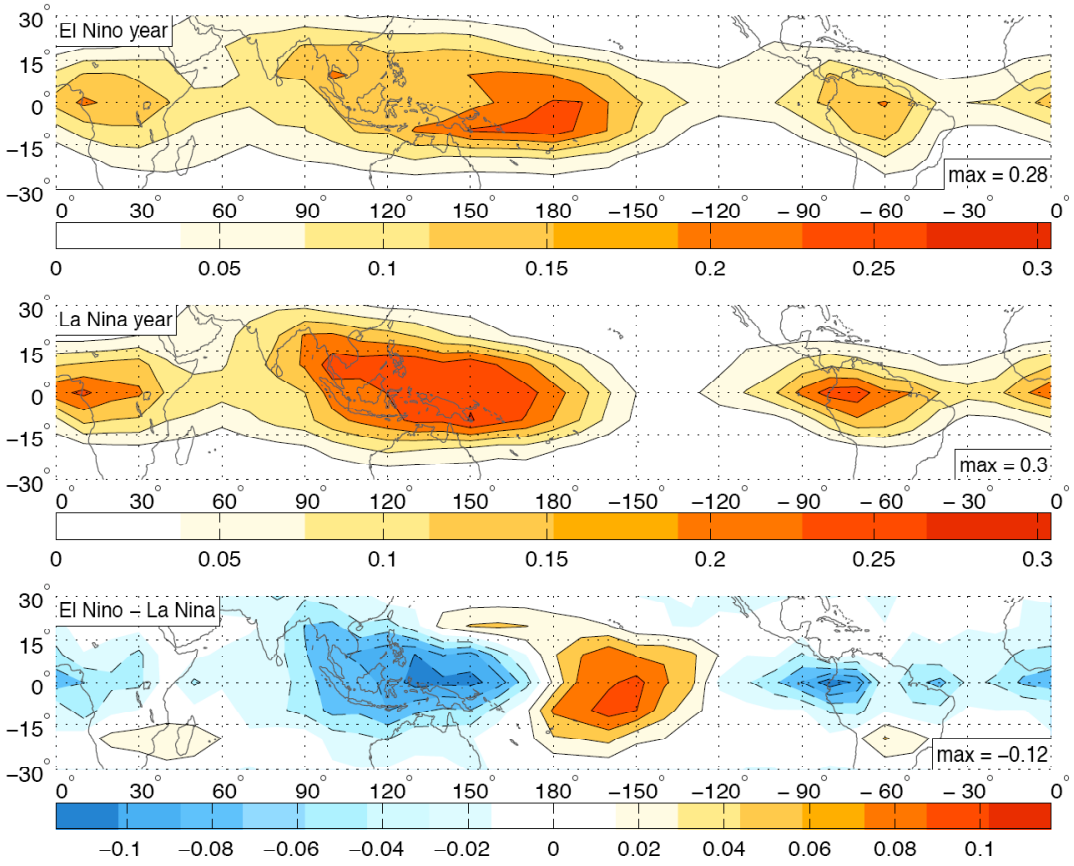

Figure 7.6 Mean CALIPSO TTL cirrus index (cloud fraction with base above 15 km) during "El Niño" (June 2006–June 2007; panel A) and "La Niña" (June 2007–June 2008; panel B) years, as well as the difference between them (panel C). Contour intervals are 0.05 (panels A and B) and 0.025 (panel C). Maximum cloud fraction in lower right. Cloud fraction is unfiltered.

much as 40% larger during the La Niña year. A similar zonal shift in cirrus occurrence above the Maritime Continent and Pacific during the strong ENSO events of the late 1990s was observed by Gettelman et al. (2001) based on boreal wintertime data from the HALOE experiment. Equatorial South America and, to a lesser degree, Africa also experienced more TTL cloudiness during the La Niña year. The limited CALIPSO data record presently at our disposal allows for only this simplified means of diagnosing the impact of ENSO on TTL cirrus, but based on our results, further study of this relationship seems warranted.

SECTION 8: SUMMARY AND CONCLUSIONS

In this study, we have used data from the CALIPSO satellite to investigate a variety of characteristics of TTL cirrus — where they are most frequently found, the mechanisms involved in their formation, the characteristics of the local and planetary-scale environment that influence their frequency of occurrence, and their intraseasonal, annual, and interannual variability. In this section, we summarize our results using composite plots and time series and comment on the use of the CALIPSO data set for analyses such as the ones we have conducted.

A composite view of the relationship between TTL cirrus and 100 hPa temperature is presented in panel A of Figures 8.1 and 8.2. For this figure, the equatorial belt is divided into 36 adjacent 10° latitude × 10° longitude boxes, and mean TTL cirrus cloud fractions (with base above 15 km) are calculated for each. Boxes whose mean cloud fraction exceeded 0.2 are included in this composite; a total of 13 boxes (eight from the Maritime Continent/western Pacific, three from equatorial South America, and two from equatorial Africa) pass this criteria. The time series of 100 hPa temperature in the selected boxes are correlated with the TTL cloud index throughout the tropics, as in Figure 3.5, or the height-dependent cloud fraction throughout the equatorial belt, as in Figure 3.11. The resulting one-point correlation maps and cross-sections are then shifted zonally such that the reference boxes are all located at 0° relative longitude. The mean correlations at each grid point are plotted in panel A of Figures 8.1 and 8.2. Similarly constructed composite correlations with 100 hPa ω, 300 hPa ω, and 300 hPa relative humidity as the reference variables are shown in panels B, C, and D, respectively. Variables in these and subsequent composites have been filtered using the 60-day high-pass Lanczos filter.

The composites in Figures 8.1 and 8.2 summarize our findings from Section 3. TTL cirrus are most strongly correlated with 100 hPa temperature, which is an indicator of the

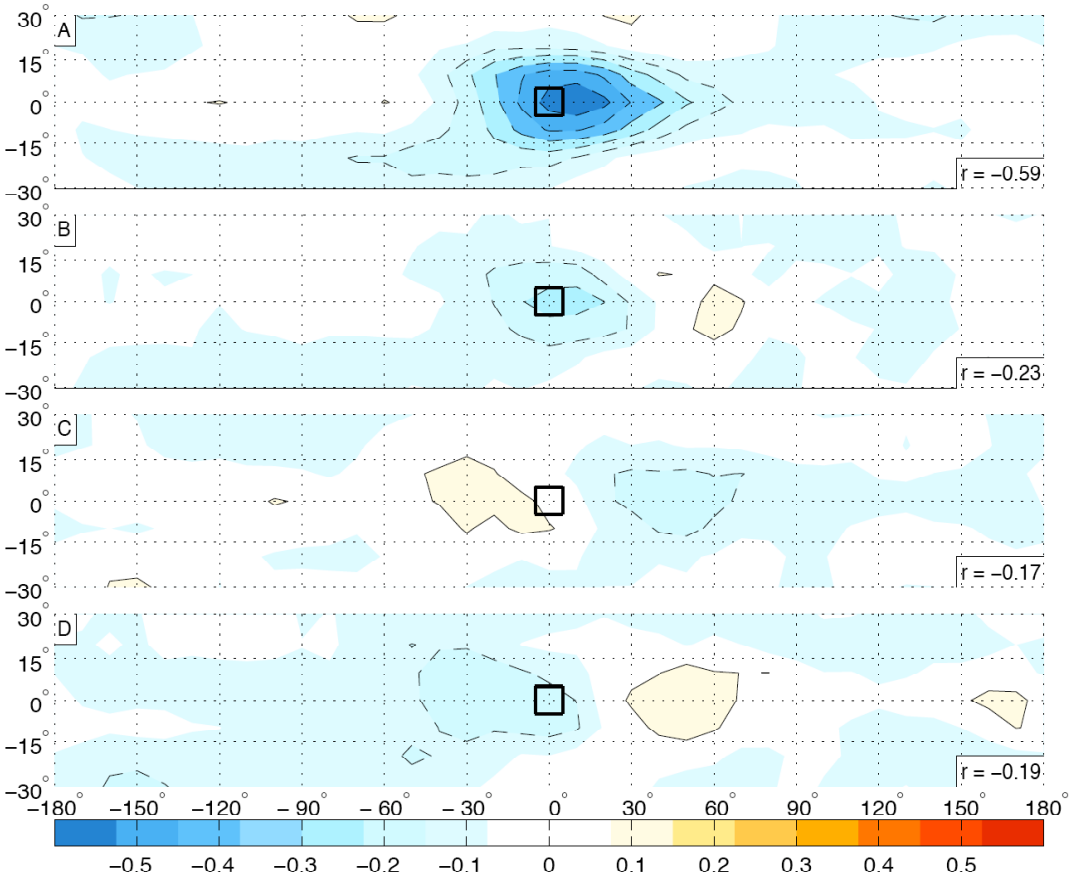

Figure 8.1 Latitude-longitude maps of composite correlations between CALIPSO 15 km base TTL cirrus index throughout tropics and GFS variables within reference regions. Variables used are A) 100 hPa temperature, B) 100 hPa ω, C) 300 hPa ω, and D) 300 hPa relative humidity. Selected reference regions have mean TTL cirrus fraction >= 0.2 (see text for further details). Contour interval is 0.1. All variables have been filtered with 60-day high-pass Lanczos filter. Largest magnitude correlation in lower right corner.

planetary wave configuration in the TTL. The strongest correlations are near –0.6. The relationship between temperature and cirrus occurrence is not limited to the immediate vicinity of the reference box; significant correlations with the cirrus field extend eastward from the reference box, along the equator, for over 30° of longitude. To the west of the reference box, the cirrus field tends to flank the equator. The cloud signature associated with 100 hPa temperature tilts eastward with height within the TTL, and a weak convective signature extends down to the Earth's surface approximately 30° of longitude to the west of the reference box. TTL cirrus is positively correlated with ascent at the 100 hPa level, but the composite

correlations displayed in panel B of Figures 8.1 and 8.2 are not nearly as strong as those for 100 hPa temperature. The weaker signal may also be due in part to unreliability in the GFS 100 hPa ω field itself, and temperature perturbations might be a better indicator of the cumulative lifting that mediates cirrus formation at this level.

While TTL cirrus are well correlated with 100 hPa temperature, they are not consistently correlated with 300 hPa ascent in the vicinity of the reference boxes, as demonstrated in panel C of Figures 8.1 and 8.2. A vertically oriented convective signature exists in the reference box, but the weak cirrus signal that does exist in the composite field above the 15 km level is displaced eastward from the reference box by between 30° and 60° of longitude. Similarly, TTL cirrus clouds above the 15 km level near the reference boxes are *negatively* correlated with 300 hPa relative humidity (see panel D of Figures 8.1 and 8.2).

Combining these observations with the relative cloud frequency composites in Figure 3.2, which demonstrate the limited vertical extent of TTL cirrus, we can conclude that the primary formation mechanism for TTL cirrus is ascent within planetary-scale waves. Tropical convection may, however, be a greater contributor to lower-based tropical cirrus, as demonstrated in Figure 3.10.

In Section 4, an analysis of the more localized correlations between temperature and cloud fraction at two ARM sites in the warm pool region yielded marginally significant positive correlations in the middle and upper troposphere. Within the TTL, cloud fraction and temperature are strongly negatively correlated, with correlation coefficients of similar magnitude to the peak correlations in Figure 3.3. Temperature anomalies between 4°C and 6°C are observed above the warm pool region in association with TTL cirrus based on analysis of both the ARM radiosonde profiles and GFS 100 hPa temperatures; anomalies over equatorial Africa and South America are on the order of 2°C to 4°C.

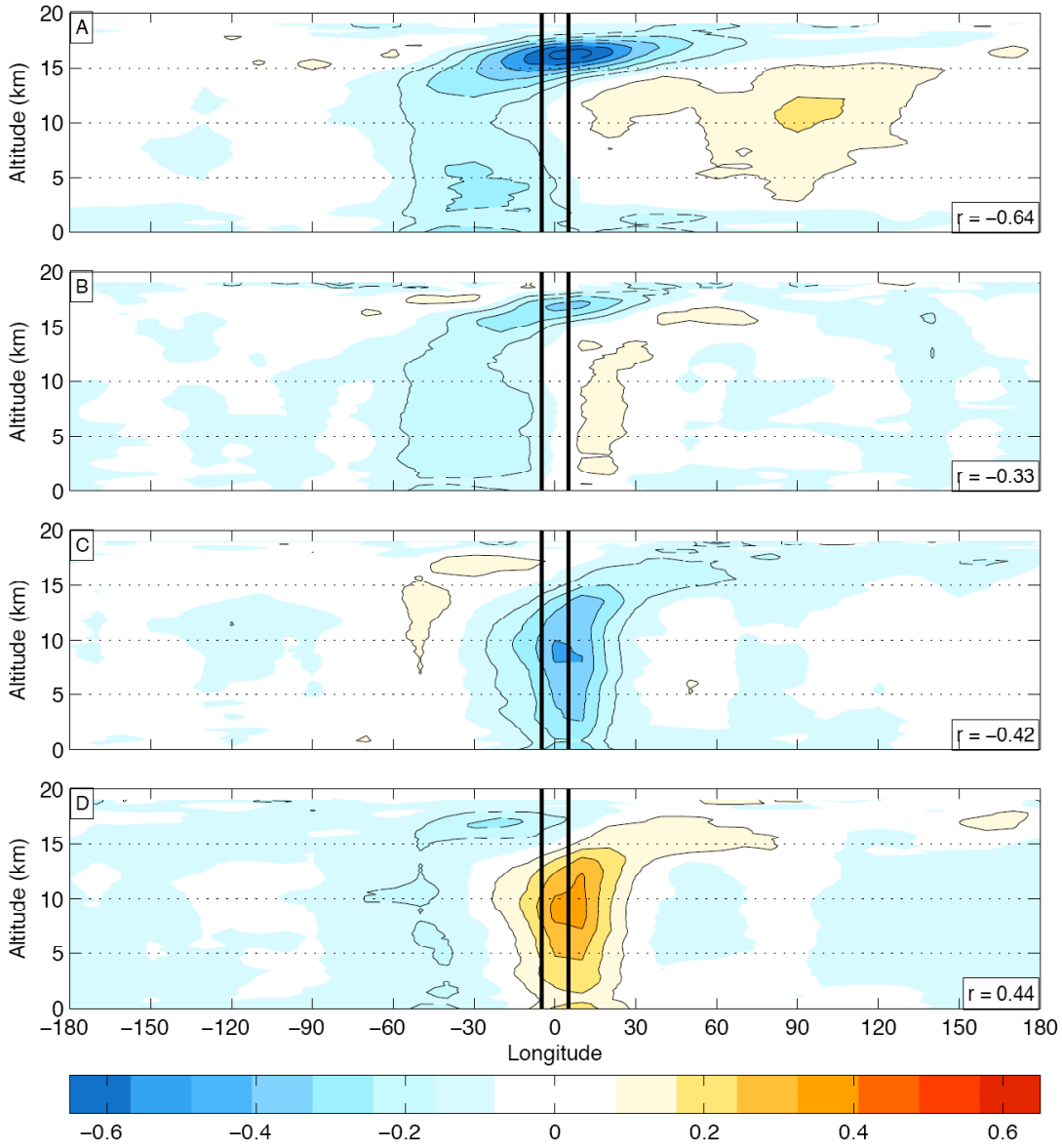

Figure 8.2 As in Figure 8.1, but longitude-height composite correlations between GFS variables in black reference regions and CALIPSO height dependent cloud fraction index from 5°S to 5°N.

The same compositing method described above can also be applied to the one-point correlation analyses presented in Section 5. Composite correlations between the TTL cirrus index within the selected reference boxes and 100 hPa temperatures and winds are plotted in panel A of Figure 8.3; the corresponding composite of correlations with 150 hPa geopotential heights and winds is plotted in panel B.

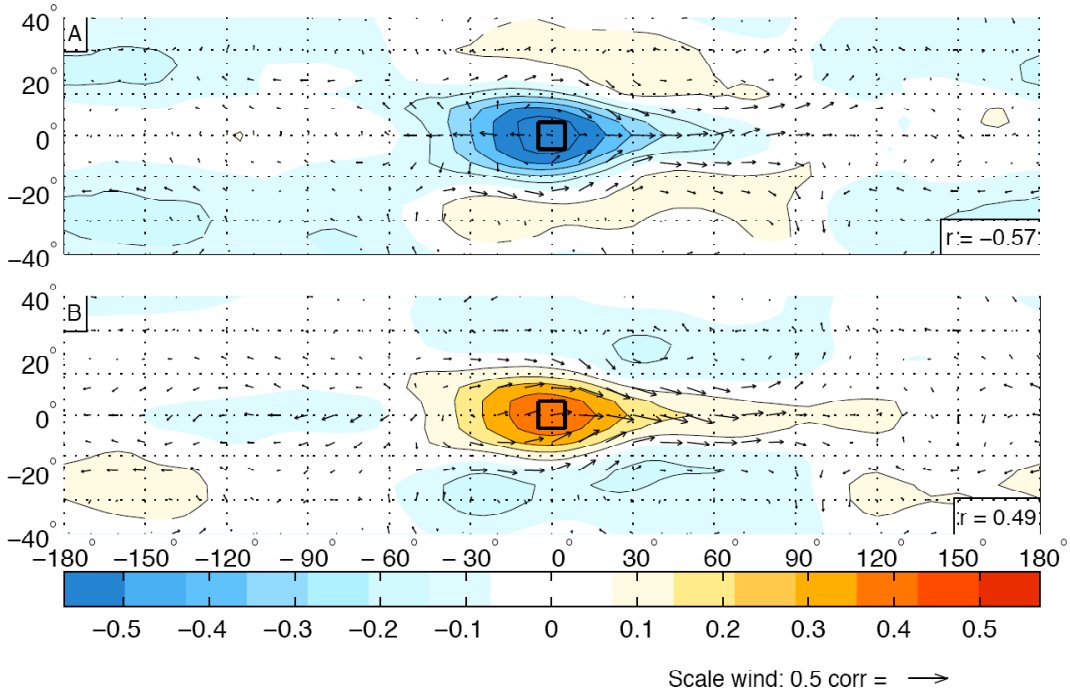

Figure 8.3 Latitude-longitude maps of composite correlations between CALIPSO 15 km base TTL cirrus index within reference regions GFS variables throughout tropics. Variables used are A) 100 hPa temperature and winds, and B) 150 hPa geopotential height and winds. Selected reference regions have mean TTL cirrus fraction >= 0.2 (see text for further details). Contour interval is 0.1. All variables have been filtered with 60-day high-pass Lanczos filter. Largest magnitude correlation in lower right corner.

At 100 hPa, TTL cirrus occurrence is significantly correlated with anomalously low temperatures over a broad region similar in extent and shape to the cirrus field in panel A of Figure 8.3. Easterly winds are observed to the west of the reference box, while winds to its north, south, and east are westerly, resulting in divergence within the reference box itself and convergence to the east of it. In panel B, we observe that TTL cirrus is also significantly positively correlated with geopotential height, although the relationship with geopotential height is weaker than that with temperature. At this level, the region of high geopotential heights corresponds almost perfectly with the region of westerly wind anomalies. Secondary temperature and geopotential height features can be seen along the northeastern and southeastern flanks of the primary correlation centers in both panels of Figure 8.3, but they are not statistically significant.

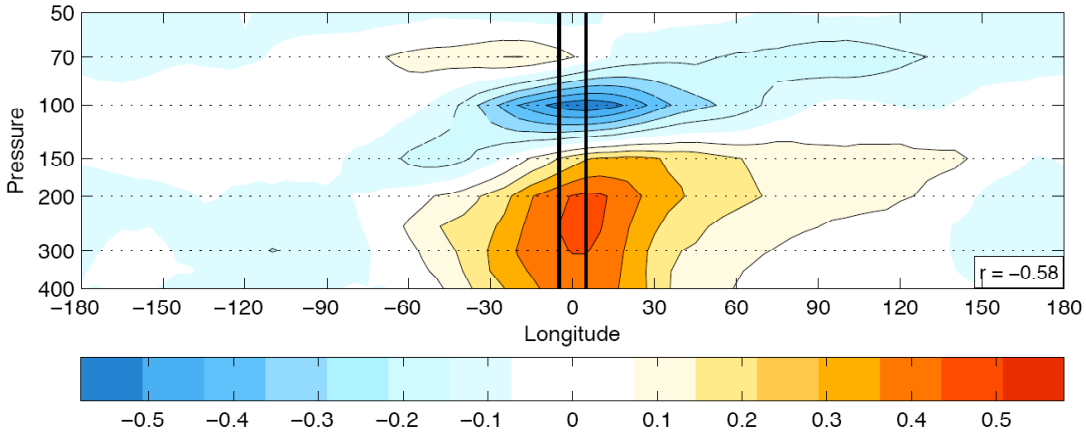

Figure 8.4 Longitude-pressure plot of composite correlations between CALIPSO 15 km base TTL cirrus index within 10° × 10° reference regions and GFS temperatures (colors and contours) from 2.5°S to 2.5°N. Selected reference regions have mean TTL cirrus fraction >=0.2 (see text for further details). Contour interval is 0.1. All variables have been filtered with 60-day high-pass Lanczos filter. Largest magnitude correlation in lower right corner.

A similarly constructed composite of the longitude-pressure correlations between TTL cirrus within the reference boxes and GFS temperatures throughout the tropical upper troposphere, TTL, and lower stratosphere is shown in Figure 8.4. The strongest temperature anomalies are observed at the 100 hPa level, while positive temperature anomalies prevail below the 150 hPa level and are strongest near 250 hPa. An eastward tilt with height is observed above the ~250 hPa level. At the 70 hPa level, positive temperature anomalies are observed between 0° and 60° to the west of the reference box. These anomalies are not statistically significant, but this element of the planetary wave signature is more clearly seen in some of the individual correlation plots in Figure 5.3. Overall, these longitude-pressure plots reveal a structure consistent with that of theoretically-derived equatorially-trapped Kelvin waves (Holton 1979; Wallace and Kousky 1968; Roundy 2008).

The temperature and wind anomalies indicated in panel A of Figure 8.1 and the large-scale ascent demonstrated by the TTL cirrus correlations in panel A of Figure 8.2 are consistent with the convectively-induced equatorial planetary wave signature that has been predicted by various modeling studies (e.g., Gill 1980; Highwood and Hoskins 1998). These similarities are

more evident in some of the individual correlation plots in Figures 3.5 and 5.1 and in composites which only include reference boxes from the Maritime Continent and western Pacific (not shown).

In Section 6, we investigated the connection between TTL cirrus and the Madden-Julian Oscillation. As the MJO progresses from an initial enhancement of the convection over the Indian Ocean through a disappearance of this positive anomaly after it enters the Pacific Ocean, the TTL cirrus field exhibits a weak feature that develops into a strong, large-scale maximum over the warm pool region (see Figures 6.2 and 6.3). The cirrus signature associated with the MJO also resembles the planetary wave pattern of Gill (1980) and tilts eastward with height. Thus, planetary-scale variations in tropical convection, specifically those associated with the MJO, can be said to modulate TTL cirrus formation. The TTL cirrus feature over the Pacific disappears as the convective signature dissipates, but the perturbation within the TTL continues to propagate eastward, as evidenced by positive cirrus maxima over equatorial South America and Africa during Phases 6 through 8. The role, if any, of this perturbation in the initiation of the subsequent MJO cycle remains an open question.

The intraseasonal, annual, and interannual variability of TTL cirrus was explored in Sections 6 and 7 and is summarized in Figure 8.5. Panel A plots the cold tongue index (CTI) during the two years of our study. In Panels B and C, tropical mean TTL cirrus (cloud fraction with base above 15 km) and 100 hPa temperature are presented as seven-day running means equatorward of 10° (analogous time series for latitudes equatorward of 20° are largely similar). Tropical mean TTL cirrus fraction and 100 hPa temperature, filtered using the 60-day high-pass Lanczos filter, are plotted in the fourth and fifth panels of Figure 8.5. The time series of Phase 6 of the MJO index is shown in the bottom panel. The cloud fraction and temperature time series share many similarities. When tropical mean 100 hPa temperature is regressed onto

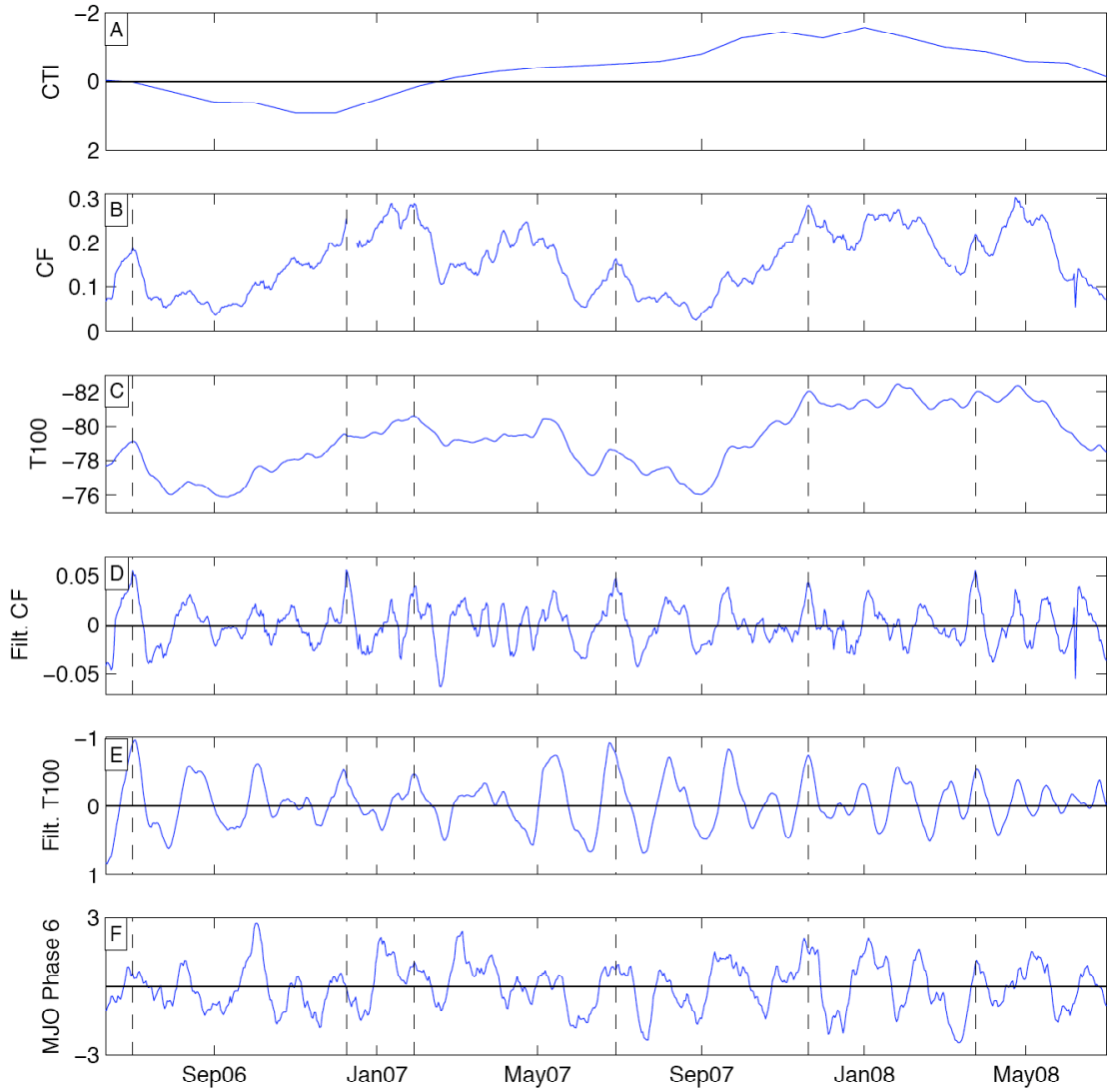

Figure 8.5 Time series of selected variables for June 2006 – June 2008. Panel A: cold tongue index (see Figure 7.3). Panel B: seven-day running mean tropical mean TTL cirrus fraction (cloud fraction with base above 15 km; equatorward of 10°). Panel C: as in panel B, but for GFS 100 hPa temperature. Panel D: as in panel B, but time series filtered using 60-day high-pass Lanczos filter. Panel E: as in panel C, but time series filtered using 60-day high-pass Lanczos filter. Panel F: MJO Phase 6 (see Figure 6.8). Vertical reference lines mark the six highest peaks in filtered cloud fraction.

tropical mean TTL cirrus fraction, the regression coefficient is −22.21°C (−10.94°C using the filtered time series), or temperature drop of 2.22°C for a 10% increase in cloud fraction.

Tropical mean TTL cirrus fraction is modulated by ENSO and the annual cycle, as revealed by our brief examination in Section 7. The boreal winter months are the cloudiest

season in the TTL (see panel B of Figure 8.5), with cirrus maxima in the equatorial belt and southern tropics, while TTL cirrus occurrence during the boreal summer months is dominated by the Indian monsoon. During El Niño, the largest TTL cirrus fractions are observed over the western and central Pacific. The cirrus center intensifies and shifts westward during La Niña, residing above the Maritime Continent and warm pool. By our calculations, the percent increase in tropical mean TTL cirrus fraction equatorward of 10° latitude from JJA to DJF (El Niño to La Niña) during our period of study is 144.4% (15.6%). Lower temperatures within the TTL are evident in Figure 8.5 during the boreal winter and when the CTI is negative (the latter result was also noted in the lower stratosphere by Yulaeva and Wallace 1994). Below the $\sim 15-16$ km level, the annual cycle in cirrus occurrence is highly equatorially asymmetric.

We documented in Section 6 the relationship between tropical mean TTL cirrus fraction and the MJO; this relationship is summarized in the lower three panels of Figure 8.5. Tropicalmean TTL cirrus is at a minimum during the first three phases of the MJO's evolution and is most widespread during Phases 5 through 7, when the convective and cirrus features cross into the Pacific Ocean. The strongest signal in the 100 hPa temperature and TTL cirrus fields is found during Phases 2 and 6. Visual inspection of the time series in the bottom three panels of Figure 8.5 reveals the similarities among these three time series; for reference, the dates corresponding to the six highest peaks in the filtered cloud fraction time series are marked with vertical dashed lines in panels B through F, demonstrating that the MJO signal is discernible even in the unfiltered time series. The correlation coefficient between MJO Phase 6 and the filtered tropical mean TTL cirrus fraction time series is 0.48 (the corresponding value for the filtered 100 hPa temperature time series is -0.40), almost the same magnitude as the strongest correlations observed between MJO phase and local TTL cirrus index time series. The percent increase in tropical mean TTL cirrus fraction from Phase 2 to Phase 6 is 92%.

The use in this study of TTL cirrus data from the CALIPSO satellite has proven both illuminating and challenging. On one hand, this data set provides an unprecedented amount of information regarding the occurrence and characteristics of TTL cirrus, including details about layer reflectivity and optical depth that we have not examined in this study. Its orbital paths ensure a geographic sampling of the tropical belt that is adequate for many purposes. Using the CALIPSO data set has allowed us to identify factors involved in TTL cirrus formation and to analyze the relationship of the TTL cirrus field to planetary wave activity in the TTL and atmospheric variability on a variety of time scales.

The CALIPSO data set is not without its limitations. As of the time this research was begun, only two years of CALIPSO data were available for analysis. The shortness of the data record limited our ability to assess the annual and interannual variability of TTL cirrus and, to a lesser degree, the relationship with the MJO (since only 15–17 realizations of the MJO occurred during our period of study); we have also not considered components of the interannual variability other than ENSO. Despite this limitation, the ENSO, annual cycle, and MJO signals we have noted in the TTL cirrus field are in generally good agreement with similar results based on other atmospheric variables (see discussions in Sections 6 and 7), indicating that the short duration of the CALIPSO data set has not seriously compromised our results. On a positive note, as of the time of this writing, the CALIPSO satellite is still functional and gathering more data. Several additional years of data from this instrument may eventually be available, depending of course upon the satellite's continued health and operational capability.

The greater limitation of the CALIPSO data set has proved to be its irregular spatial and temporal sampling. A given point along one of CALIPSO's orbital paths is sampled once every 16 days; consecutive daytime or nighttime passes cross the equator ~25° longitude apart

with a time difference of ~1.6 hours. As a result, most tropical clouds are sampled only once by the CALIPSO satellite, and a meaningful, representative daily map of TTL cirrus occurrence cannot be obtained from it. These sampling characteristics limit our ability to describe the characteristics of the TTL cirrus field and relate it to other atmospheric variables. The quality of results we have been able to obtain demonstrates that, even with these limitations, the CALIPSO data set is a valuable tool for the study of the tropical atmosphere, including TTL cirrus.

The strongest correlations we have documented between GFS temperatures and TTL cirrus are ~0.7. While such correlations are highly statistically significant, this means that roughly half the variance of the temperature field in a particular location can be explained by the TTL cirrus field (and vice versa); the remaining variance is, then, unexplained. Factored into this issue is the irregular spatial and temporal sampling of the CALIPSO satellite — were the true correlation between 100 hPa temperature and TTL cirrus fraction 1.0, analysis of the two fields as sampled by CALIPSO and the GFS model would likely not capture the full strength of the relationship. A natural question to pursue is to what extent the limited sampling of the CALIPSO satellite contributes to the lower correlations and to what extent TTL cirrus variability simply cannot be explained by the 100 hPa temperature field (and, thus, other factors unexplored in this thesis must be at work).

A means of answering this question is to determine to what extent forcibly limited sampling of the GFS field would lower similar correlations. One-point correlation maps of filtered GFS 100 hPa temperature with itself are shown in Figure 8.6 using the same five reference boxes as before. Figure 8.7 shows similar one-point correlation maps, but for this figure we have artificially limited the GFS data sampling. For each CALIPSO pass, the closest GFS longitudinal data “curtain” (spatially) and run (temporally) is selected, and only

temperatures from the selected GFS data points are used to calculate the time series of 100 hPa temperature within the reference boxes. The limited time series is then filtered and correlated with the full, filtered GFS data set throughout the tropics.

The strongest correlation in each panel of Figures 8.6 and 8.7 is indicated in the lower right corner; for Figure 8.6 this value is, by definition, 1.0. Peak correlations in Figure 8.7 range from 0.84 to 0.92, which demonstrates that our forced limited sampling of the 100 hPa temperature field degrades the correlations, making it appear that the relationship between 100 hPa temperature and itself is weaker than in reality. We can reasonably expect that the limited sampling of TTL cirrus by the CALIPSO satellite would, likewise, underestimate the true correlation between cloud fraction and 100 hPa temperature. Peak correlations in Figure 5.1 are, however, weaker than those in Figure 8.7. From this we conclude that while the relationship between cloud fraction and 100 hPa temperature is likely stronger than indicated by our calculations, there remains a portion of the variance in the TTL cirrus field that cannot be explained by planetary wave activity (as represented by the 100 hPa temperature field).

As mentioned above, past research (e.g., Dima 2005; Fueglistaler et al. 2009, and references therein) has identified a Gill (1980)-like signature in observational data within the TTL. However, one of the surprising results presented in this thesis is the degree of similarity between the TTL cirrus and 100 hPa temperature signatures in Figures 3.5 and 5.1, as well as in the top panels of Figures 8.1 and 8.3. Even with coarser horizontal resolution and sampling, the TTL cirrus field shares many of the characteristics of the temperature field, the Gill (1980)-like feature in particular (this feature above the Maritime Continent also appears in the first EOF of the TTL cirrus field [not shown]). This offers confirmation that this feature in the TTL is not simply a result of the GFS' dynamics. Similar signatures are also found in the TTL cirrus field in association with the MJO (see Section 6).

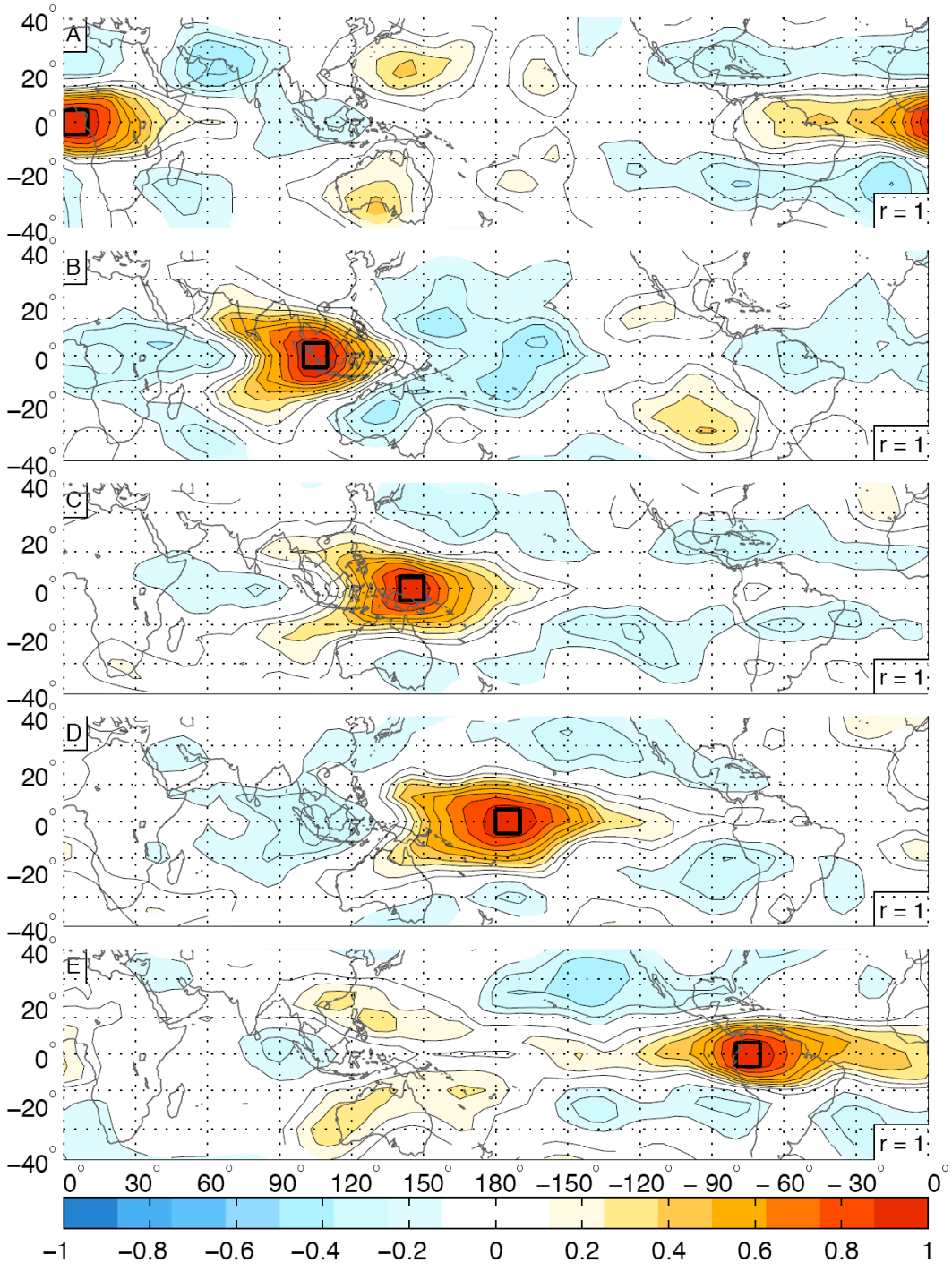

Figure 8.6 Latitude-longitude maps of correlations between GFS 100 hPa temperatures within black reference boxes and GFS 100 hPa temperatures (colors and contours) throughout tropics. Contour interval is 0.1. Both variables have been filtered with 60-day high-pass Lanczos filter. Largest magnitude correlation in lower right.

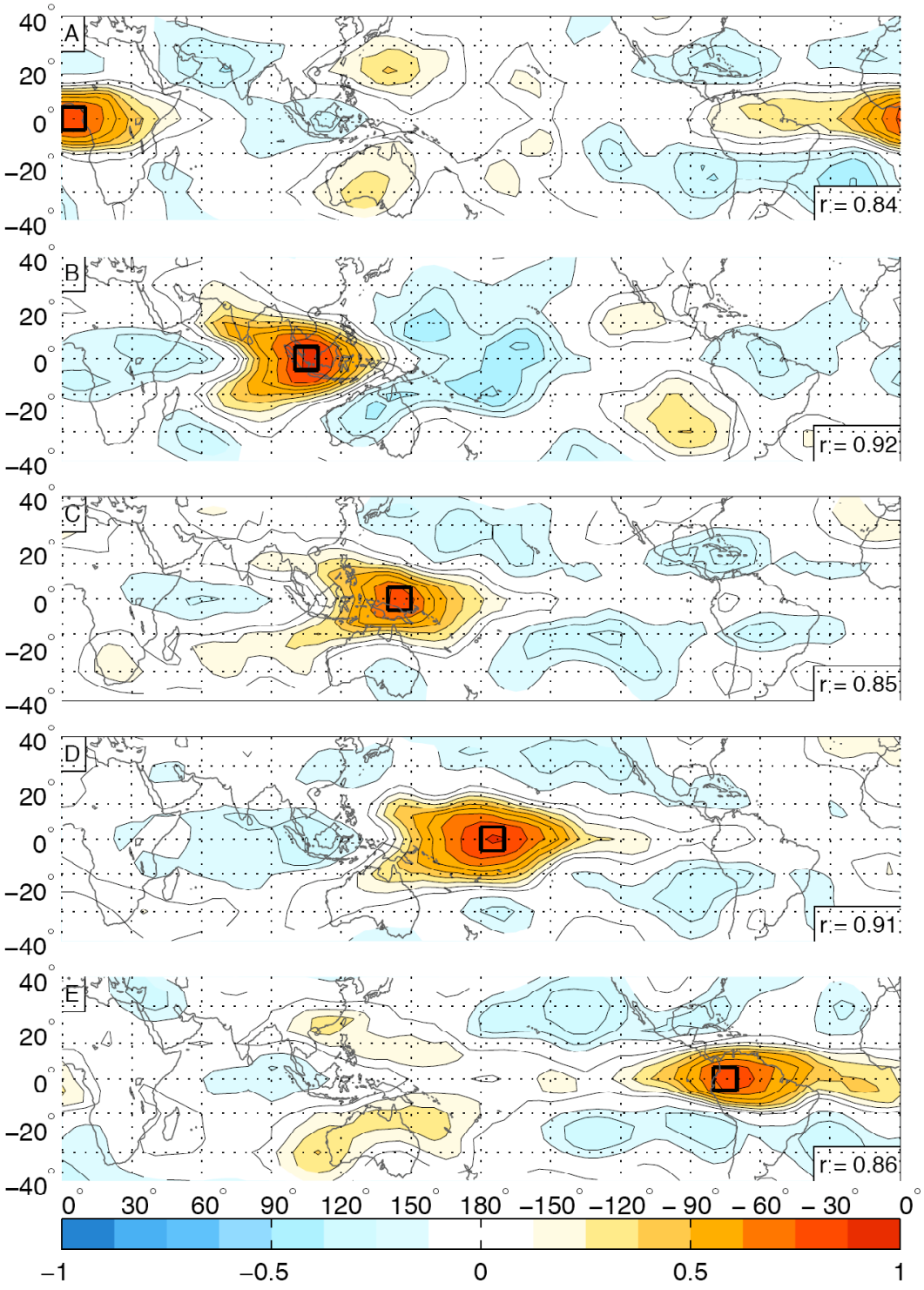

Figure 8.7 As in Figure 8.6, but time series within reference boxes has been artificially limited to match the CALIPSO passes through the region. See text for details.

The Gill (1980)-like signature we have discovered in the TTL cirrus field is a classical result. More peculiar and unexpected is the consistent out-of-phase relationship between the Maritime Continent and both equatorial Africa and South America, visible to some degree in multiple panels of Figures 3.5, 3.11, 5.1, 5.2, and 5.3. To test this observation, we have calculated mean temperature and TTL cirrus indices for Africa (0°–30°E), the Maritime Continent (90°E–120°E), and South America (80°W–50°W). Temperature indices for each region are defined as mean 100 hPa temperature equatorward of 10° latitude; TTL cirrus indices are defined as the fraction of CALIPSO profiles acquired equatorward of 10° latitude which identify a cloud with base above 15 km, similar to our previous cloud index. All indices are calculated using the same consecutive seven-day periods as above and filtered using the 60-day high-pass Lanczos filter. The correlation coefficients between mean temperatures (cloud fractions) over these regions are as follows: Africa and the Maritime Continent –0.25 (–0.48); the Maritime Continent and South America –0.21 (–0.39); and Africa and South America 0.30 (0.44). This confirms our observation that TTL temperatures and cloudiness over the Maritime Continent are out of phase with those over equatorial Africa and South America. Interestingly, TTL cirrus fractions above these regions are more strongly related than 100 hPa temperatures, whose correlations are only marginally statistically significant. This phenomenon is at least partly explained by the active and suppressed phases of the MJO, as demonstrated by the fact that the Maritime Continent and equatorial Africa and South America are out of phase in each of the temperature and TTL cirrus plots in Section 6. Other factors which we have not investigated are likely also involved.

In the course of this study, the variable to which we have most frequently compared TTL cirrus is 100 hPa temperature. The relationship between TTL cirrus and three atmospheric variables is demonstrated in Figure 8.8. For this figure, unfiltered TTL cirrus

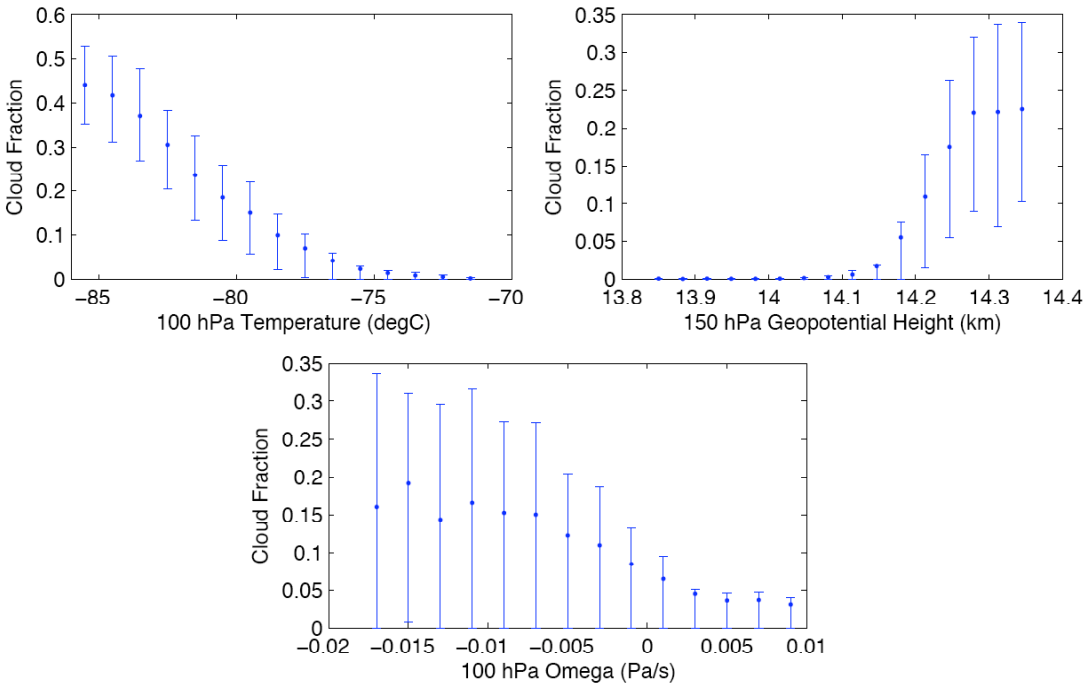

Figure 8.8 Scatter plots of mean TTL cirrus index within regularly spaced bins of GFS 100 hPa temperatures (°C, top left panel), 150 hPa geopotential heights (km, top right panel), and 100 hPa vertical velocities (Pa/s, bottom panel). Error bars indicate 25th and 75th percentiles of cloud fraction for each interval. Cirrus index is calculated as cloud fraction with base above 15 km within 10° latitude × 10° longitude regions over seven-day periods. GFS variables have been averaged to match resolution of cirrus index. All variables are unfiltered.

fractions are paired with collocated 100 hPa temperatures, 150 hPa geopotential heights, and 100 hPa vertical velocities. Mean cloud fractions for regularly spaced temperature, height, and velocity bins are plotted, along with error bars that indicate the 25th and 75th percentiles of cloud fraction for each interval. All data equatorward of 30° latitude are included in these scatter plots.

The tendency for cloudier conditions in the TTL when temperatures are lower, when ascent in the TTL is observed, and above regions of high geopotential height is evident in the scatter plots in Figure 8.8. In this figure, TTL cirrus is most strongly related to 100 hPa temperature, and the lowest ($< -83°$C) temperatures are associated with cloud fractions near or exceeding 0.4. These relationships are not sensitive to the size of the grid box over which cloud occurrence and temperature are averaged or to whether the data are time averaged (not

shown). This result is not in agreement with Clark (2005), who observed decreasing cloud fraction (identified by the Cryogenic Limb Array Etalon Spectrometer [CLAES]) at the 100-hPa level when ambient temperatures decreased beyond 190 K (–83°C). In contrast to the relationship with 100 hPa temperature, the mean cloud fractions associated with the highest 150 hPa geopotential heights and strongest 100 hPa vertical velocities are ~0.23 and ~0.17, respectively. As mentioned above, we speculate that cirrus formation takes place in air that has a history of ascent and that temperature perturbations may be a better indicator of this ascent. The spread in the cloud fractions associated with cold 100 hPa temperatures is also smaller than for the other two variables, another indication that TTL cirrus is most closely related to 100 hPa temperature.

We should also note that, at the ARM sites, seven-day mean cold point temperatures lower than –90°C are observed (see Figure 2.1), demonstrating that the area-averaged temperatures plotted in Figure 8.8 do not capture the more extreme TTL temperatures observed locally. This attests to the coarsening of data which takes place when we calculate averages over areas and seven-day periods, as has been done for almost all data in this study. Such averaging allows us to see more definitely features such as the planetary wave signature and TTL cirrus field associated with the MJO, but an investigation of fine-scale features, such as those documented in Boehm and Verlinde (2000), or cirrus variability at shorter time scales, such as diurnal variations or nighttime sedimentation of tropical cirrus (Fujiwara et al. 2009), would require the analysis of more localized TTL cirrus fields.

BIBLIOGRAPHY

Adler, R. F., G. J. Huffman, A. Chang, R. Ferraro, P.-P. Xie, J. Janowiak, B. Rudolf, U. Schneider, S. Curtis, D. Bolvin, A. Gruber, J. Susskind, and E. Nelkin, 2003: The Version-2 Global Precipitation Climatology Project (GPCP) monthly precipitation analysis (1979–present). *J. Hydromet.*, **4**, 1147–1167.

Alcala, C. M., and A. E. Dessler, 2002: Observations of deep convection in the tropics using the Tropical Rainfall Measuring Mission (TRMM) precipitation radar. *J. Geophys. Res.*, **107** (D24), 4792, doi:10.1029/2002JD002457.

Atmospheric Science Data Center, cited 2009: CALIOP algorithm theoretical basis document: Part 2: Feature detection and layer properties algorithm. [Available online at http://www-CALIPSO.larc.nasa.gov/resources/pdfs/PC-SCI-202_Part2_rev1x01.pdf.]

——, cited 2009: CALIPSO quality statements: Lidar level 2 cloud and aerosol layer products version release: 2.01. [Available online at http://eosweb.larc.nasa.gov/PRODOCS/CALIPSO/Quality_Summaries/CALIOP_L2LayerProducts_2.01.html.]

Bantzer, C. H., and J. M. Wallace, 1996: Intraseasonal variability in tropical mean temperature and precipitation and their relation to the tropical 40–50 day oscillation. *J. Atmos. Sci.*, **53**, 3032–3045.

Birner, T., 2006: Fine-scale structure of the extratropical tropopause region. *J. Geophys. Res.*, **111**, D04104, doi:10.1029/2005JD006301.

Boehm, M. T., and J. Verlinde, 2000: Stratospheric influence on upper tropospheric tropical cirrus. *Geophys. Res. Lett.*, **27**, 3209–3212.

——, and S. Lee, 2003: The implications of tropical Rossby waves for tropical tropopause cirrus formation and for the equatorial upwelling of the Brewer–Dobson circulation. *J. Atmos. Sci.*, **60**, 247–261.

Clark, H. L., 2005: Longitudinal variability of water vapor and cirrus in the tropical tropopause layer. *J. Geophys. Res.*, **110**, D07107, doi:10.1029/2004JD004943.

Comstock, J. M., T. P. Ackerman, and G. G. Mace, 2002: Ground-based lidar and radar remote sensing of tropical cirrus clouds at Nauru Island: cloud statistics and radiative impacts. *J. Geophys. Res.*, **107**, No. D23, 4714, doi:10.1029/2002JD002203.

Corti, T., B. P. Luo, Q. Fu, H. Vömel, and T. Peter, 2006: The impact of cirrus clouds on tropical troposphere-to-stratosphere transport. *Atmos. Chem. Phys.*, **6**, 2539–2547.

Danielsen, E. F., 1993: In situ evidence of rapid, vertical, irreversible transport of lower tropospheric air into the lower tropical stratosphere by convective cloud turrets and by larger-scale upwelling in tropical cyclones. *J. Geophys. Res.*, **98**, 8665–8681.

Deser, C., and J. M. Wallace, 1990: Large-scale atmospheric circulation features of warm and cold episodes in the tropical Pacific. *J. Climate*, **3**, 1254–1281.

Dima, I. M., 2005: An observational study of the tropical tropospheric circulation. Ph.D. dissertation, University of Washington, 110 pp.

——, and J. M. Wallace, 2007: Structure of the annual-mean equatorial planetary waves in the ERA-40 Reanalyses. *J. Atmos. Sci.*, **64**, 2862–2880.

Duchon, C. E., 1979: Lanczos filtering in one and two dimensions. *J. Appl. Met.*, **18**, 1016–1022.

Durran, D. R., T. Dinh, M. Ammerman, and T. Ackerman, 2009: The mesoscale dynamics of thin tropical tropopause cirrus. *J. Atmos. Sci.*, **66**, 2859–2873.

Eguchi, N., and M. Shiotani, 2004: Intraseasonal variations of water vapor and cirrus clouds in the tropical upper troposphere *J. Geophys. Res.*, **109**, D12106, doi:10.1029/2003JD004314.

Fu, Q., Y. Hu, and Q. Yang, 2007: Identifying the top of the tropical tropopause layer from vertical mass flux analysis and CALIPSO lidar cloud observations. *Geophys. Res. Lett.*, **34**, L14813, doi:10.1029/2007GL030099.

Fueglistaler, S., H. Wernli, and T. Peter, 2004: Tropical troposphere-to-stratosphere transport inferred from trajectory calculations. *J. Geophys. Res.*, **109**, D03108, doi:10.1029/2003JD004069.

——, A. E. Dessler, T. J. Dunkerton, I. Folkins, Q. Fu, and P. W. Mote, 2009: Tropical tropopause layer. *Rev. Geophys.*, **47**, RG1004, doi:10.1029/2008RG000267.

Fujiwara, M., S. Iwasaki, A. Shimizu, Y. Inai, M. Shiotani, F. Hasebe, I. Matsui, N. Sugimoto, H. Okamoto, N. Nishi, A. Hamada, T. Sakazaki, and K. Yoneyama, 2009: Cirrus observations in the tropical tropopause layer over the western Pacific. *J. Geophys. Res.*, **114**, D09304, doi:10.1029/2008JD011040.

Gettelman, A., W. J. Randel, S. Massie, F. Wu, W. G. Read, and J. M. Russell III, 2001: El Niño as a natural experiment for studying the tropical tropopause region. *J. Climate*, **14**, 3375–3392.

Gill, A. E., 1980: Some simple solutions for heat-induced tropical circulation. *Quart. J. R. Met. Soc.*, **106**, 447–462.

Hartmann, D. L., 1994: *Global Physical Climatology*. Academic Press, 411 pp.

Hendon, H. H., and Salby, M. L., 1994: The life cycle of the Madden–Julian Oscillation. *J. Atmos. Sci.*, **51**, 2225–2237.

——, 1995: Length of day changes associated with the Madden–Julian Oscillation. *J. Atmos. Sci.*, **52**, 2373–2383.

Highwood, E. J., and B. J. Hoskins, 1998: The tropical tropopause. *Quart. J. R. Met. Soc.*, **124**, 1579–1604.

Holton, J. R., 1979: *An Introduction to Dynamic Meteorology.* Academic Press, 391 pp.

——, P. H. Haynes, M. E. McIntyre, A. R. Douglass, R. B. Rood, and L. Pfister, 1995: Stratosphere-troposphere exchange. *Rev. Geophys*., **33**, p. 403–439.

Horel, J. D., and J. M. Wallace, 1981: Planetary-scale atmospheric phenomena associated with the Southern Oscillation. *Mon. Wea. Rev.*, **109**, 813–829.

Hsu, H.-H, and M.-Y. Lee, 2005: Topographic effects on the eastward propagation and initiation of the Madden-Julian Oscillation. *J. Climate*, **18**, 795–809.

Immler, F., K. Krüger, M. Fujiwara, G. Verver, M. Rex, and O. Schrems, 2008: Correlation between equatorial Kelvin waves and the occurrence of extremely thin ice clouds at the tropical tropopause. *Atmos. Chem. Phys.*, **8**, 4019–4026.

Jakob, C., G. Tselioudis, and T. Hume, 2005: The radiative, cloud, and thermodynamic properties of the major tropical western Pacific cloud regimes. *J. Climate*, **18**, 1203–1215.

Jensen, E. J., O. B. Toon, H. B. Selkirk, J. D. Spinhirne, and M. R. Schoeberl, 1996: On the formation and persistence of subvisible cirrus clouds near the tropical tropopause. *J. Geophys. Res.*, **101**, 21361-21375.

——, and L. Pfister, 2004: Transport and freeze-drying in the tropical tropopause layer. *J. Geophys. Res.*, **109**, D02207, doi:10.1029/2003JD004022.

Knutson, T. R., and K. M. Weickmann, 1987: 30–60 day atmospheric oscillations: composite life cycles of convection and circulation anomalies. *Mon. Wea. Rev.*, **115**, 1407–1436.

Leith, C. E., 1973: The standard error of time–averaged estimates of climatic means. *J. Appl. Met.*, **12**, 1066–1069.

Madden, R. A., and P. R. Julian, 1971: Detection of a 40–50 Day oscillation in the zonal wind in the tropical Pacific. *J. Atmos. Sci.*, **28**, 702–708.

—— and ——, 1972: Description of global–scale circulation cells in the tropics with a 40–50 day period. *J. Atmos. Sci.*, **29**, 1109–1123.

—— and ——, 1994: Observations of the 40–50-Day tropical oscillation — A review. *Mon. Wea. Rev.*, **122**, 814–837.

Massie, S., A. Gettelman, W. Randel, and D. Baumgardner, 2002: Distribution of tropical cirrus in relation to convection. *J. Geophys. Res.*, **107**, doi:10.1029/2001JD001293.

Mather, J. H., T. P. Ackerman, W. E. Clements, F. J. Barnes, M. D. Ivey, L. D. Hatfield, and R. M. Reynolds, 1998: An atmospheric radiation and cloud station in the tropical western Pacific. *Bull. Amer. Met. Soc.*, **79**, 627–642.

——, 2005: Seasonal variability in clouds and radiation at the Manus ARM site. *J. Climate*, **18**, 2417–2428.

Matsuno, T., 1966: Quasi-geostrophic motions in the equatorial area. *J. Met. Soc. Japan*, **44**, 25–42.

McFarquhar, G. M., A. J. Heymsfield, J. Spinhirne, and B. Hart, 2000: Thin and subvisual tropopause tropical cirrus: Observations and radiative impacts. *J. Atmos. Sci.*, **57**, 1841–1853.

Reed, R. J., and C. L. Vlcek, 1969: The annual temperature variation in the lower tropical stratosphere. *J. Atmos. Sci.*, **26**, 163–167.

Robinson, G. D., 1980: The transport of minor atmospheric constituents between troposphere and stratosphere. *Quart. J. R. Met. Soc.*, **106**, 227–253.

Ropelewski, C. F., and M. S. Halpert, 1987: Global and regional scale precipitation patterns associated with the El Niño/Southern Oscillation. *Mon. Wea. Rev.*, **115**, 1606–1626.

Roundy, P. E., 2008: Analysis of convectively coupled Kelvin waves in the Indian Ocean MJO. *J. Atmos. Sci.*, **65**, 1342–1359.

Schwartz, M. J., D. E. Waliser, B. Tian, D. L. Wu, J. H. Jiang, and W. G. Read, 2008: Characterization of MJO-related upper tropospheric hydrological processes using MLS. *Geophys. Res. Lett.*, **35**, L08812, doi:10.1029/2008GL033675.

Seo, K. –H., J. –K. E. Schemm, C. Jones, and S. Moorthi, 2005: Forecast skill of the tropical intraseasonal oscillation in the NCEP GFS dynamical extended range forecasts. *Clim. Dyn.*, **25**, 265–284.

Tian, B., D. E. Waliser, E. J. Fetzer, B. H. Lambrigtsen, Y. L. Yung, and B. Wang, 2006: Vertical moist thermodynamic structure and spatial-temporal evolution of the MJO in AIRS observations. *J. Atmos. Sci.*, **63**, 2462–2485.

——, Y. L. Yung, D. E. Waliser, T. Tyranowski, L. Kuai, E. J. Fetzer, and F. W. Irion, 2007: Intraseasonal variations of the tropical total ozone and their connection to the Madden-Julian Oscillation. *Geophys. Res. Lett.*, **34**, L08704, doi:10.1029/2007GL029451.

——, D. E. Waliser, R. A. Kahn, Q. Li, Y. L. Yung, T. Tyranowski, I. V. Geogdzhayev, M. I. Mishchenko, O. Torres, and A. Smirnov, 2008: Does the Madden-Julian Oscillation influence aerosol variablity? *J. Geophys. Res.*, **113**, D12215,

doi:10.1029/2007JD009372.

Van Tuyl, A. H., 1986: Advective influences on forced tropical motions. *J. Atmos. Sci.*, **43**, 141–161.

Wallace, J. M., and V. E. Kousky, 1968: Observational evidence of Kelvin waves in the tropical stratosphere. *J. Atmos. Sci.*, **25**, 900–907.

Wang, P.-H., P. Minnis, M. P. McCormick, G. S. Kent, and K. M. Skeens, 1996: A 6-year climatology of cloud occurrence frequency from Stratospheric Aerosol and Gas Experiment II observations (1985–1990). *J. Geophys. Res.*, **101**, 29407–29430.

Webster, P. J., 1972: Response of the tropical atmosphere to local, steady forcing. *Mon. Wea. Rev.*, **100**, 518–541.

Wheeler, M., G. N. Kiladis, and P. J. Webster, 2000: Large-scale dynamical fields associated with convectively coupled equatorial waves. *J. Atmos. Sci.*, **57**, 613–640.

——, and H. H. Hendon, 2004: An all-season real-time multivariate MJO index: Development of an index for monitoring and prediction. *Mon. Wea. Rev.*, **132**, 1917–1932.

Winker, D. M., and C. R. Trepte, 1998: Laminar cirrus observed near the tropical tropopause by LITE. *Geophys. Res. Lett.*, **25**, 3351–3354.

——, W. H. Hunt, and M. J. McGill, 2007: Initial performance assessment of CALIOP. *Geophys. Res. Lett.*, **34**, L19803, doi:10.1029/2007GL030135.

Yin, X., A. Gruber, and P. Arkin, 2004: Comparison of the GPCP and CMAP merged gauge–satellite monthly precipitation products for the period 1979–2001. *J. Hydromet.*, **5**, 1207–1222.

Yulaeva, E., and J. M. Wallace, 1994: The signature of ENSO in global temperature and precipitation fields derived from the Microwave Sounding Unit. *J. Climate*, **7**, 1719–1735.

Zhang, C., 1993: On the annual cycle in highest, coldest clouds in the tropics. *J. Climate*, **6**, 1987–1990.

——, 2005: Madden–Julian Oscillation. *Rev. Geophys.*, **43**, RG2003, doi:10.1029/2004RG000158.